Quantitative kinematic and thermal full fields measurement

Chao Zhang

N°d'ordre NNT : 2019LYSEI013

THÈSE de DOCTORAT DE L'UNIVERSITÉ DE LYON
opérée au sein de
I'Institut National des Sciences Appliquées de Lyon

Ecole Doctorale 162
Mécanique, Energétique, Génie civil, Acoustique

Spécialité/ discipline de doctorat
MÉCANIQUE - GÉNIE MÉCANIQUE - GÉNIE CIVIL

Soutenue publiquement le 05/03/2019, par:

Chao ZHANG

Quantitative Kinematic and Thermal Full Fields Measurement

Devant le jury composé de :

WATTRISSE, Bertrand	Professeur (Université Montpellier)	Rapporteur
AMIOT, Fabien	Chargé de Recherche HDR (FEMTO-ST)	Rapporteur
CHARKALUK, Eric	Directeur de Recherche (Ecole Polytechnique)	Examinateur
MAYNADIER, Anne	Maître de Conférences (UFC)	Examinatrice
BAIETTO, Marie-Christine	Directrice de Recherche (INSA Lyon)	Directrice de thèse
RÉTHORÉ, Julien	Directeur de Recherche (EC Nantes)	Co-directeur de thèse

Département FEDORA – INSA Lyon - Ecoles Doctorales – Quinquennal 2016-2020

SIGLE	ECOLE DOCTORALE	NOM ET COORDONNEES DU RESPONSABLE
CHIMIE	CHIMIE DE LYON http://www.edchimie-lyon.fr Sec. : Renée EL MELHEM Bât. Blaise PASCAL, 3e étage secretariat@edchimie-lyon.fr INSA : R. GOURDON	M. Stéphane DANIELE Institut de recherches sur la catalyse et l'environnement de Lyon IRCELYON-UMR 5256 Équipe CDFA 2 Avenue Albert EINSTEIN 69 626 Villeurbanne CEDEX directeur@edchimie-lyon.fr
E.E.A.	ÉLECTRONIQUE, ÉLECTROTECHNIQUE, AUTOMATIQUE http://edeea.ec-lyon.fr Sec. : M.C. HAVGOUDOUKIAN ecole-doctorale.eea@ec-lyon.fr	M. Gérard SCORLETTI École Centrale de Lyon 36 Avenue Guy DE COLLONGUE 69 134 Écully Tél : 04.72.18.60.97 Fax 04.78.43.37.17 gerard.scorletti@ec-lyon.fr
E2M2	ÉVOLUTION, ÉCOSYSTÈME, MICROBIOLOGIE, MODELISATION http://e2m2.universite-lyon.fr Sec. : Sylvie ROBERJOT Bât. Atrium, UCB Lyon 1 Tél : 04.72.44.83.62 INSA : H. CHARLES secretariat.e2m2@univ-lyon1.fr	M. Philippe NORMAND UMR 5557 Lab. d'Ecologie Microbienne Université Claude Bernard Lyon 1 Bâtiment Mendel 43, boulevard du 11 Novembre 1918 69 622 Villeurbanne CEDEX philippe.normand@univ-lyon1.fr
EDISS	INTERDISCIPLINAIRE SCIENCES-SANTE http://www.ediss-lyon.fr Sec. : Sylvie ROBERJOT Bât. Atrium, UCB Lyon 1 Tél : 04.72.44.83.62 INSA : M. LAGARDE secretariat.ediss@univ-lyon1.fr	Mme Emmanuelle CANET-SOULAS INSERM U1060, CarMeN lab, Univ. Lyon 1 Bâtiment IMBL 11 Avenue Jean CAPELLE INSA de Lyon 69 621 Villeurbanne Tél : 04.72.68.49.09 Fax : 04.72.68.49.16 emmanuelle.canet@univ-lyon1.fr
INFOMATHS	INFORMATIQUE ET MATHEMATIQUES http://edinfomaths.universite-lyon.fr Sec. : Renée EL MELHEM Bât. Blaise PASCAL, 3e étage Tél : 04.72.43.80.46 Fax : 04.72.43.16.87 infomaths@univ-lyon1.fr	M. Luca ZAMBONI Bât. Braconnier 43 Boulevard du 11 novembre 1918 69 622 Villeurbanne CEDEX Tél : 04.26.23.45.52 zamboni@maths.univ-lyon1.fr
Matériaux	MATÉRIAUX DE LYON http://ed34.universite-lyon.fr Sec. : Marion COMBE Tél : 04.72.43.71.70 Fax : 04.72.43.87.12 Bât. Direction ed.materiaux@insa-lyon.fr	M. Jean-Yves BUFFIÈRE INSA de Lyon MATEIS - Bât. Saint-Exupéry 7 Avenue Jean CAPELLE 69 621 Villeurbanne CEDEX Tél : 04.72.43.71.70 Fax : 04.72.43.85.28 jean-yves.buffiere@insa-lyon.fr
MEGA	MÉCANIQUE, ÉNERGÉTIQUE, GENIE CIVIL, ACOUSTIQUE http://edmega.universite-lyon.fr Sec. : Marion COMBE Tél : 04.72.43.71.70 Fax : 04.72.43.87.12 Bât. Direction mega@insa-lyon.fr	M. Jocelyn BONJOUR INSA de Lyon Laboratoire CETHIL Bâtiment Sadi-Carnot 9, rue de la Physique 69 621 Villeurbanne CEDEX jocelyn.bonjour@insa-lyon.fr
ScSo	ScSo* http://ed483.univ-lyon2.fr Sec. : Viviane POLSINELLI Brigitte DUBOIS INSA : J.Y. TOUSSAINT Tél : 04.78.69.72.76 viviane.polsinelli@univ-lyon2.fr	M. Christian MONTES Université Lyon 2 86 Rue Pasteur 69 365 Lyon CEDEX 07 christian.montes@univ-lyon2.fr

*ScSo : Histoire, Géographie, Aménagement, Urbanisme, Archéologie, Science politique, Sociologie, Anthropologie

Acknowledges

This thesis of the research work I have carried out between 2015 and 2019 at the Laboratory of Contact and Structural Mechanics (LaMCoS). I would like to express my gratitude to all those whole helped me during the completion of the thesis. Without their support and encouragement, this thesis could not be finished.

First and foremost, I want to extend my heartfelt gratitude to my supervisor, Marie-Christine BAIETTO (Directrice de Recherche - CNRS) for having offered me the opportunity to do something on this interesting topic. During these years, her patient guidance, valuable suggestion and constant encouragement make me successfully complete this thesis. Thank you very much to my co-supervisors, Julien RÉTHORÉ (Directeur de Recherche - CNRS), Anne MAYNADIER (Maître de conférences) and Jeremy MARTY (Maître de conférences), for their supervision during these years. I appreciate the help and advices they gave me. Their enthusiasm and rigor on the research work taught me the necessary characters to carry out a scientific work. We also exchanged many interesting ideas with each other.

Second, I would like to express my sincere gratitude to Philippe CHAUDET and Thomas JAILIN who provided me with technical supports in the experimental part. Their availability and expertise allowed me to realize the experimental studies in the desired direction.

Special thanks for my colleagues of the laboratory with whom I lived in a friendly environment: Tardif NICOLAS, Sonde Abayomi EMMANUEL, Alexis BONETTO, Zikang LOW, Lv ZHAO. Wenjun GAO, Ye LU, Shuai CHEN, Deqi LIU, Meng WANG, Tristan MAQUART, Liangxiao BU.

I would like to thank my country and China Scholarship Council for supporting my research and life in France.

Last but not least, I want to express my thanks to my family. First of all, thanks to my wife Pei's constant and inexhaustible support during these years, then my parents' support and encouragement. Finally, I would like to express my thanks for the coming of my daughter Mujin.

Abstract

Simultaneous measurement of kinematic and thermal full fields are very important for thermomechanical procedures. Silicon-based cameras are widely used to perform real-time observation of the kinematic fields, mainly thanks to digital image correlation. Moreover, they are known to be as well sensitive in the near-infrared spectral range, thus the acquirement of thermal fields using silicon-based cameras is possible. However, there are two main problems for the silicon-based camera to obtain simultaneously kinematic and thermal fields. One is that in the near-infrared spectral range, a small temperature variation will lead to a large modification in the image gray level, which easily leads to poor quality images. Another is that digital image correlation needs a heterogeneous and contrasting surface, while the near-infrared thermography needs a homogeneous and constant surface.

In this thesis, an innovative technique was proposed to automatically adjust the exposure time of the camera to obtain kinematically and thermally exploitable images whatever the temperature evolution occurs on the surface of the observed object. This technique was validated by different experiments, including blackbody heating experiments and realistic specimen heating experiments. Radiometric models of blackbody and specimen surfaces ware calibrated respectively. Based on the radiometric models, thermal fields have been reconstructed on the kinematically and thermally exploitable images.

High temperature tube ballooning experiment is conducted to perform both kinematic and thermal fields. Global digital image correlation was performed to obtain kinematic fields. To perform near-infrared thermography on the specimen surface, radiometric model is calibrated based on portions of the brightest pixels. In this case 20% of the brightest pixels are used to perform radiometric model calibration. Based on the radiometric model using 20% of the brightest pixels, the thermal fields are reconstructed. Combined with the known coordinates of kinematic fields by digital image correlation, the thermal fields at the same coordinates as kinematic fields can be obtained.

KEYWORDS: Silicon-based camera, Kinematic field, Thermal field, Radiometric model, Exposure time adjustment, Thermomechanical

Résumé

La mesure simultanée des champs cinématiques et thermiques est très importante pour les procédures thermomécaniques. Les caméras à base de silicium sont largement utilisées pour l'observation en temps réel des champs cinématiques, principalement grâce à la corrélation d'images numériques. De plus, ils sont aussi connus pour sa sensibilité dans le spectre du proche infrarouge, ce qui permet d'acquérir des champs thermiques à l'aide d'une caméra à base de silicium. Cependant, pour la caméra à base de silicium, il y a deux problèmes principaux d'obtenir simultanément des champs cinématiques et thermiques. D'abord, dans le spectre du proche infrarouge, une petite variation de température entraînera une modification importante du niveau de gris de l'image, ce qui entraînera facilement une mauvaise qualité des images. Deuxième, la corrélation d'images numériques nécessite une surface hétérogène et contrastée, tandis que la thermographie dans le proche infrarouge nécessite une surface homogène et constante.

Dans cette thèse, une technique innovante a été proposée pour ajuster automatiquement le temps d'exposition de la caméra afin d'obtenir des images exploitables pour l'analyse cinématique et thermique, quel que soit l'évolution de température à la surface de l'objet observé. Cette technique a été validée par expériences différentes, notamment des expériences de chauffage d'un corps noir et des expériences de chauffage d'un échantillon réel. Les modèles radiométriques du corps noir et de la surface des échantillons calibrent respectivement. Basé sur les modèles radiométriques, des champs thermiques ont été reconstruits sur les images exploitables pour l'analyse cinématique et thermique.

L'expérience à haute température est réalisée pour le ballonnement des tubes où les champs cinématiques et thermiques sont observés. La corrélation d'images numériques a été effectuée globalement afin d'obtenir des champs cinématiques. Pour effectuer la thermographie du proche infrarouge sur la surface de l'échantillon, le modèle radiométrique est étalonné selon une partie des pixels les plus brillants. Dans ce cas, 20% des pixels les plus brillants sont utilisés pour effectuer l'étalonnage des modèles radiométriques. Basée sur le modèle en utilisant 20% des pixels plus brillants, les champs thermiques sont reconstruits. Combiné avec les coordonnées connues du champ cinématique par corrélation d'images numériques, le champ thermique et le champ cinématique dans les mêmes coordonnées peut être obtenu.

MOTS CLÉS: Caméra à base de silicium, Champ cinématique, Champ thermique, Modèle radiométrique, Réglage du temps d'exposition, Thermomécanique

Contents

List of Figures

List of Tables

General introduction

Nowadays, experimental science is faced with major multi-physical challenges (particularly thermo-mechanical procedure) requiring the development of advanced test benches, multiplying the use of in-situ measurement techniques. Measurement of deformation and temperature is very important for thermo-mechanical procedures, such as mechanical tests at high temperature (fatigue, fracture, impact, et al.) and materials processing at high temperature (welding, forming, heating treatment, et al.). To measure deformation, many methods have been developed, e.g., classical strain gages, grid method, speckle interferometry, digital image correlation, etc. Digital image correlation appeared in the early 1980s has a major impact in the non-contact full field kinematic measurement of mechanics of materials and structures, which is still undergoing very spectacular developments. Common silicon-based cameras are used to perform digital image correlation. With the rapid development of cameras technology and personal computers' computational abilities, this technique will become more widely used in various fields. To know the temperature, many techniques are also available, e.g., thermocouple, thermistor, resistance temperature detector, and infrared thermography, etc. Among these methods, infrared thermography is an advanced real-time non-contact, high-speed response and full field measurement technique. Generally, infrared thermography is performed using infrared cameras. If both kinematic and thermal fields can be simultaneously obtained by digital image correlation and infrared thermography, which can provide rich and relevant information on the thermo-mechanical procedures.

To simultaneously obtain kinematic and thermal fields, many researchers have made efforts on this topic. Many different methods are proposed to simultaneously obtain two fields. The commonly used method is to use two different imaging systems. The kinematic field is obtained by digital image correlation using the silicon-based camera, and the thermal field is obtained by infrared thermography using the infrared camera. Then a *posteriori* data processing is conducted to integrate the space and time associations of these two fields. Some researchers used silicon-based camera and infrared camera to observe two different surfaces of the specimen, respectively. Srinivasan et al. [SRI 12] studied the Lüders deformation in the welded mild steel during uniaxial tensile testing. In their experiment, one surface of the specimen with black coating is used to perform infrared thermography using infrared camera so as to obtain the thermal fields, and the other surface of the specimen sprayed with speckle is used to perform digital image correlation so as to obtain the kinematic fields. Some other researchers

tried to use two imaging systems to observe the kinematic and thermal fields on the same specimen surface. Bodelot et al. [BOD 09] used a "filter-mirror" (dichroic mirror) to separate the infrared radiation and visible radiation, and a silicon-based camera is used to detect the visible radiation while an infrared camera is used to detect the infrared radiation. Simultaneous observation of kinematic and thermal fields in the same zone at the microstructure scale of an AISI 346L austenitic stainless steel specimen during tensile test was performed. However, these methods have some problems which are difficult to be simultaneously addressed: (1) Two different imaging devices have different spatial resolution and acquisition rates. The exact same spatial and temporal coordinates of kinematic and thermal fields cannot be achieved no matter how well the *posteriori* data processing is done; (2) The digital image correlation and infrared thermography have conflicting requirements for the specimen surface. DIC needs a heterogeneous and contrasting texture on the specimen surface, which is tracked to perform the kinematic fields. But the IRT needs a homogeneous and constant emissivity on the surface, of which the temperature can be measured with little influence of emissivity variation; (3) the combination of these two imaging systems is expensive and uneasy. Complicated experimental set-up should be conducted to combine these two imaging systems by special expensive filters and other installations due to the different spectral ranges acquired by these two systems. Too much extra devices are not easy to be installed around the specimens in the tests, especially if the specimen has a complex motion trajectory.

Taking into account the above disadvantages, a few researchers tried to obtain simultaneously kinematic and thermal fields using a single type of camera. Maynadier et al. [MAY 12] used a single infrared camera to obtain kinematic and thermal fields in order to capture localized transformation bands of shape memory alloy under tension. Using a sole set of infrared camera, both two fields decomposed over the same time and space discretization can be obtained. However, the infrared camera delivered rather poor fields due to its low resolution. Moreover, the infrared cameras are expensive and difficult to be used, which are mostly used in the laboratory research. Compared with infrared camera, silicon-based camera is cheaper, presents lower noise, possesses longer durability and has major advantage to deliver a far higher resolution, and it can be widely used for industrial applications. Orteu et al. [ORT 08] tried to use a single type of silicon-based camera (CCD camera) to measure both displacement and temperature fields. However, the preliminary exploration has been done. Some problems have not been solved. The problem that the digital image correlation and infrared thermography have conflicting requirements for the specimen surface has not been addressed. The temperature they obtained is just the apparent temperature (i.e., radiation intensity) and the true temperature fields cannot be obtained. In addition, there is another problem for silicon-based camera to be used for temperature measurement. In the near-infrared spectral range, a small temperature variation will lead to a large modification in the image gray level, which easily leads to poor quality images due to oversaturation and/or poor dynamic range of gray levels. The stable image gray level is the basis for both digital image correlation technique and near-infrared thermography technique. Especially for the digital image correlation, the image

correlation is based on the gray level conservation between reference image and deformed images. The variation of image gray level will introduce large errors.

The objective of this thesis is to measure simultaneously kinematic and thermal full fields using a single silicon-based camera. The problems mentioned above are intended to be addressed when a silicon-based camera is used.

In Chapter 2, an innovative technique is proposed to automatically adjust the exposure time of the camera to obtain kinematically and thermally exploitable images whatever the temperature evolution occurs on the surface of the observed object. Then, the accuracy and reliability of this technique are validated by blackbody heating experiment.

In Chapter 3, the technique proposed in chapter 2 is used in the realistic applications, and the reliability and accuracy of this technique are further validated. Two specimen heating experiments are conducted. The radiometric models of specimen surfaces are calibrated. Then, thermal fields on specimen surfaces are reconstructed based on radiometric models.

In Chapter 4, tube ballooning experiment is conducted, and both kinematic and thermal fields on the tube surface are intended to be obtained. Global digital image correlation is performed to obtain continuous kinematic field. An innovative method is proposed to calibrate an accurate radiometric model for heterogeneous specimen surface with different emissivity paints. This study offers a low-cost simplified technique for obtaining simultaneously kinematic and thermal fields.

General conclusions and perspectives of this work are given at the end of this thesis.

Chapter 1
State of the art

This chapter contains three parts; it presents the kinematic field measurements by digital image correlation, the thermal field measurements by infrared thermography, and the current situations of coupling the kinematic and thermal fields.

Contents

Nowadays, many topics of mechanical science involve thermomechanical coupled phenomena: (1) Determination of complex constitutive model (shear bands, phase transformation, and so on); (2) Description and modeling of rupture (cracking, self-heating in fatigue, and so on); (3) Study of the manufacturing processes (modeling/development of the welding/forging, study of the cutting during milling, and so on). The analysis of these phenomena assumes the consideration of some kinematic and thermal quantities that the experimenter can attain in the form of displacements and temperatures. This raises a series of questions concerning the reliability of the measurements, the dimensions of the regions of interest and the non-disturbance of the phenomenon by the measurement itself.

The joint exploitation of these two quantities of interest allows better understanding, modeling and identifying the coupled phenomena. It is therefore necessary that the two quantities (thermal and kinematic) are measured on the same surface or the same regions of interest and at the same time.

The first part of this chapter presents the kinematics field measurement. First a short general point of view is given prior to focus on the full field measurement by image correlation: the imaging set-up that it generally requires and the basic principles of how it works.

The second part of this chapter presents the thermal field measurement, and especially the most common technique for thermo-mechanical application: the middle-wave infrared thermography.

The last part deals with the current status of coupling the two measurement methods and presents some recent works where the combination of both measuring techniques are used.

1.1 Measurement of kinematic fields

Measuring kinematic field consists in evaluating displacement or deformation on the surface of materials or structures subjected to various loading, across a large area of interest, but often with local resolution. Kinematic fields are commonly obtained using non-contact optical methods. By this way, the measurement of kinematic fields circumvents many issues:

(1) How to avoid the disturbance of the observed phenomena?

(2) How to obtain global information about the displacement of the observed surface?

(3) How to detect local events (cracking, shear or strain localization, and so on)?

There are very important issues, which have been paid special attention in experimental mechanics and materials science. Indeed, some of the commonly used technologies for the displacement or deformation measurement are: (1) the finite difference of the rigid body displacement at the edge of the observed structure; (2) the use of glued strain gages.

In the first case, the experimenter uses the displacement measured by the testing machine itself or the relative displacements of two arms of an extensometer glued or clamped on particular points of the surface. Beyond the practical implementation problems that this entails, the information obtained is then averaged between the points whose movements are known. A local phenomenon can be totally ignored, and if it is detected, we will not be able to know its position and magnitude. In the second case, strain

gauge is a contact measurement method. However, it has some disadvantages. The gauge should be glued to the specimen surface. If a small specimen or soft material are considered, the additional stiffness and weight of the strain gauge will affect seriously the measurement results. Moreover, strain gauge measurement is a point measurement method, and the full field cannot be obtained. It is difficult to use this method for studying non-uniform deformation behaviors. Lastly, strain gauge has a limited measurement range. The large deformation will break the strain gauge resistance wire, so the measurement data cannot be obtained.

The optical measurement methods are non-contact full-field measurement methods, which can deal with the aforementioned issues. There are many kinds of optical measurement methods that permit to quantify displacements: (1) interferometry technique, such as holography interferometry, speckle interferometry, moire interferometry; (2) non-interferometric techniques, such as digital image correlation (DIC), particle image velocimetry (PIV).

Interferometric optical measurement methods measure the deformation by interpreting interferences. In the case of moire or speckle interferometry, the interferences are obtained by projecting a particular pattern (grid, line, or speckle) on the exact same pattern coating the imaged object. The superposition discrepancy reveals local displacements and creates figures that can be interpreted to quantify the displacements. The laser interferometry proceeds by recording the phase difference of the scattered light wave from the test object surface before and after deformation. It could be used to obtain spot measurements or field measurements thanks to a high-speed scanning. This technique usually needs a coherent light source, normally the laser. However, the interferometry measurements have high requirements for the external environment, which should be conducted in a vibration-isolated optical platform. Thus, these techniques are normally used in the laboratory, and are difficult to be used in industrial applications due to the complex environment.

Non-interferometric optical measurement methods measure the deformation of the object surface by comparing the gray intensity changes before and after deformation. Non-interferometric optical measurement methods only need a non-coherent light source, thus they are easier to be used than the interferometric optical measurement methods. DIC is a representative non-interferometric metrology, which has been widely used for the deformation measurement of solid materials [MCC 10][HIL 06].

1.1.1 Introduction of digital image correlation

The emergence and development of DIC is contributed by the rapid development of cameras technology and personal computers' computational abilities.

Compared with the interferometric techniques, DIC presents some attractive advantages:

(1) Simple experimental set-up

A single basic camera, such as a charge-coupled device (CCD) or a complementary metal-oxide-semiconductor (CMOS) is needed to record images of the object surface during its movement.

(2) Simple specimen preparation

If the specimen surface has a natural texture, which has a random gray intensity distribution, the natural texture can be used as speckles to be easily tracked in DIC. If not, the surface can be prepared simply by spraying black and/or white paints as speckle.

(3) Strong environmental adaptability

The DIC technique does not need a laser source. White light source or natural light is enough for the measurement. Even if it is preferable that the illumination of the imaged scene stays constant all through the recording process, some lighting variation can be tolerated as long as the surface texture remains obvious. However, DIC can be used in complex work conditions, such as high temperature, high pressure, high-speed impact, vibration, et al. Thus it is very suitable for industrial applications.

(4) Wide measurement range

DIC deals with digital images, thus these images can be acquired by various high-resolution digital acquisition devices, such as optical microscopy [SUN 97][PIT 02], laser scanning confocal microscope (LSCM) [BER 06][FRA 07], scanning electron microscopy (SEM) [KAN 05][WAN 06], transmission electron microscopy (TEM) [CAL 14], atomic force microscopy (AFM) [CHA 05][SUN 06], scanning tunneling microscope (STM), [VEN 98a][VEN 98b][VEN 98c], and satellites [SCA 62][LEP 07]. All these kinds of images can be analyzed by DIC to make microscale to macroscale displacement measurement.

The idea of DIC technique was first proposed in the early 1980s by Japanese I. Yamaguchi [YAM 81][YAM 81] and W.J. Peters and W.F. Ranson [PET 82] of the University of South Carolina in the United States. I. Yamaguchi investigated the behavior of the small object deformation by calculating the cross-correlation functions of speckle illumination intensities before and after the deformation. Peters and Ranson performed the iterative operations on the digital images of the object acquired before and after deformation. They calculated the correlation coefficient with the change of displacement and its derivative to find the extreme value of the correlation coefficient, thereby obtaining the corresponding displacement.

Many researchers did a lot of work on how to speed up the calculation and improve the calculation accuracy. Peters [PET 83] firstly applied DIC technique to measure the displacement of the rigid body. In the same year, Sutton et al. [SUT 83] improved the correlation search method, and used the combination of coarse correlation and fine correlation to improve the calculation speed. HE et al. [HE 84] studied the accuracy of the DIC technique and improved the theory of this measurement method. Sutton et al. [SUT 86][SUT 88] analyzed the measurement error caused by the subpixel recovery process, and proposed reasonable methods to deal with subpixel recovery. Bruck et al. [BRU 89] used the Newton-Raphson iterative algorithm based on binary cubic spline interpolation sub-pixel reconstruction to solve the DIC problem, which greatly improved the DIC method. Vendroux and Knauss [VEN 98] used a first-order derivative approximation to process the Hessian matrix, *i.e.* that the New-Raphson algorithm was replaced by Gauss-Newton algorithm, which improved the computational efficiency by removing the process of calculating the second-order gray level gradient while ensuring the calculation

accuracy. Borgefors et al. [BOR 01] proposed the hierarchical search method, which decomposed two images to be matched into a series of images whose size gradually decreases and the resolution gradually decreased. The matching of images was from the lowest resolution level, and then gradually backtrack the results, thereby increasing the calculation speed and usability of the method. Yoneyama and Morimoto [YON 03] replaced the gray speckle pattern in the DIC technique by color speckle pattern, which improved the accuracy of displacement and strain. Réthoré et al. [RET 07a][RET08] applied the extended finite element to DIC, thereby greatly improving calculation accuracy of the discontinuous behaviors, such as cracking. Since the emergence of DIC technique, there are still many outstanding scholars who contributed to this term. Thus, the DIC technique is still undergoing very spectacular developments.

In addition to improving calculation speed and accuracy, the practical applications of DIC technique is another important topic. Its applications mainly focus on the following three aspects.

(1) Measuring the deformation properties and mechanical properties of various materials (such as metal, composite, polymer, wood, et al.) under mechanical loading and thermal loading. Zikn et al. [ZIK 95] firstly used DIC technique to investigate the mechanical properties of wood. Choi et al. [CHO 97] applied DIC technique to measure the deformation of concrete under compressive loading, and obtained the failure performance of concrete. Bastawros et al. [BAS 00] used DIC technique to obtain three stages deformation process of the aluminum alloy foam under compressive loading. Chevalier et al. [CHE 01] investigated the axial tensile tests of a kind of polymer by DIC.

(2) Based on the information of displacement and strain obtained by DIC technique, the various materials' parameters can be calculated, such as elastic modulus, Poisson's ratio, thermal expansion coefficient, stress intensity factor, fracture toughness, et al. Zhang et al. [ZHA 02] studied the variation of Poisson's ratio of the arterial vessels with axial strain by DIC. Yoneyama [YON 06] and Réthoré [RET 05] used DIC technique to measure the stress intensity factor at the crack tip. Pan et al. [PAN 07] obtained the deformation information of film, so the thermal expansion coefficient of the film can be calculated.

(3) The full field deformation data of the object surface by DIC technique is used to perform theoretical analysis and numerical simulation [SAB 06][KNA 03][CHO 05]. Thus, the theory, simulation and experiments can be linked.

After years of development, DIC technique has expanded from the initial displacement analysis in metal testing to many other fields, such as biomedicine, civil engineering, aerospace, electronics, and so on. Meanwhile, with the appearance of the atomic force microscopy, transmission electron microscopy and scanning tunneling microscope, the DIC is widely used in microscopic observations. In the past few decades, DIC has shown its great potentiality. From the perspective of further development, DIC technique will inevitably be applied to a wider range of fields with the rapid development of computers and imaging devices.

1.1.2 Measurement set-up for digital image correlation measurement

Specimen preparation

The surface of the measured object must have a random gray intensity distribution. Generally, the random speckle pattern is used as a carrier of displacement information. Some examples of speckles are schematically shown in Fig. 1.1. An isotropic pattern guarantees that the displacement could be identified in every direction of the plane. High-contrast speckle patterns ensure that the gradient will be maximum. An example of the best pattern is shown in Fig. 1.1(d). Other three patterns are not good patterns to perform DIC. Some natural texture of the specimen surface, such as the grains on the metal surface or milling streaks, can be aleatory enough to be tracked by DIC. However, in most cases, artificial speckles are made by spraying black and/or white paints.

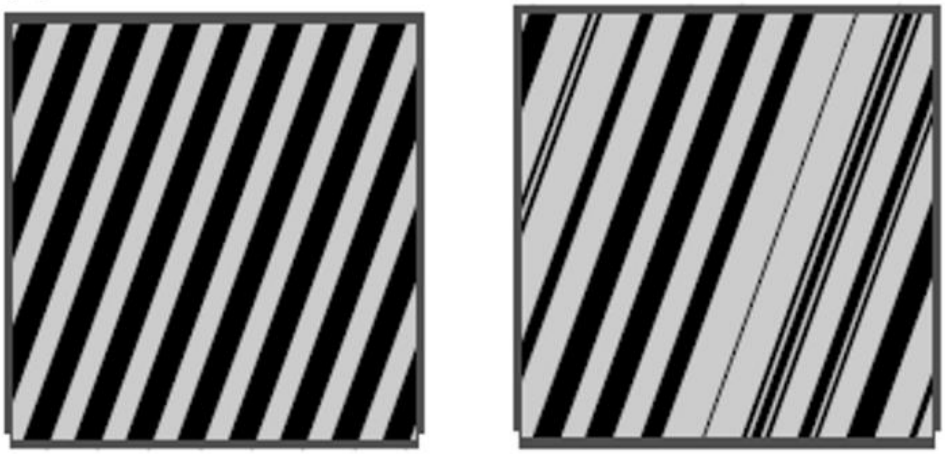

(a) Repetitive, anisotropic, high-contrast. (b) Non-repetitive, anisotropic, high-contrast.

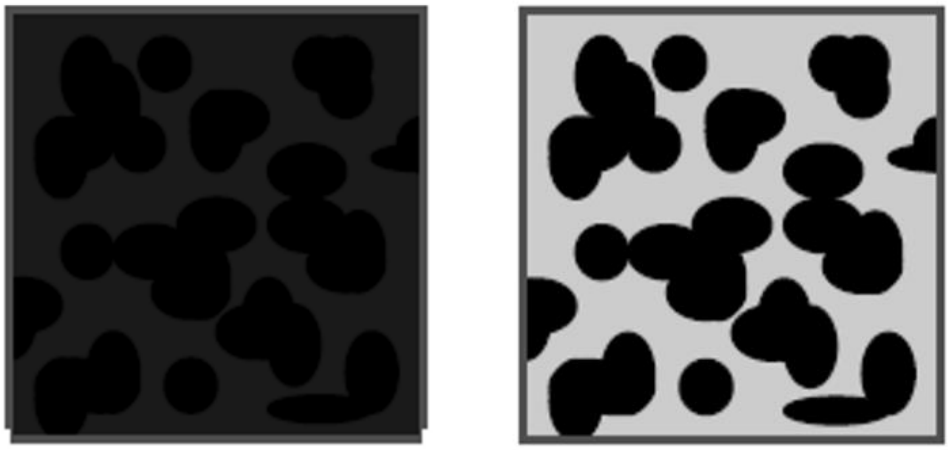

(c) Non-repetitive, isotropic, low-contrast. (d) Non-repetitive, isotropic, high-contrast.

Fig. 1.1: Example of surface pattern for DIC measurements.

Image acquisition system

The general image acquisition system for performing DIC is schematically shown in Fig. 1.2. There are four main elements: (1) specimen with surface speckle; (2) silicon-based camera (CCD or CMOS); (3) computer for data acquisition; (4) white light source. The camera is placed with its optical axis normal to the specimen surface. The white light source is used to provide a good view of the specimen surface with high-contrast gray level intensity distribution. When the specimen is under loading, the camera simultaneously records the images. Then, a *posteriori* processing of the acquired images is performed to obtain the displacement fields by the computer. The strain fields can be inferred from the displacement fields.

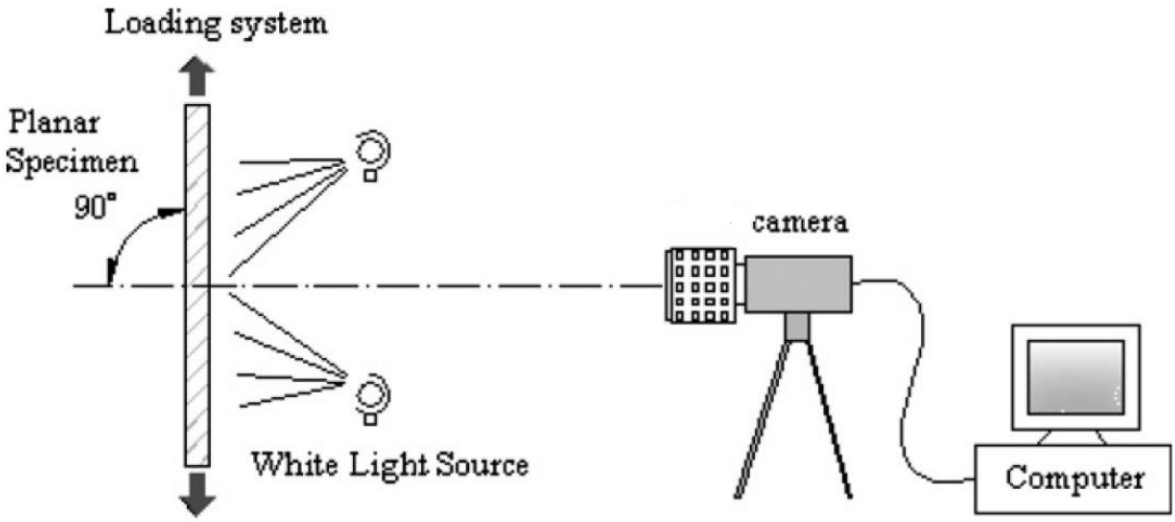

Fig. 1.2: Typical optical image acquisition system [PAN 09].

1.1.3 Basic principles of digital image correlation computation

The basic principle of DIC is to select a reference sub-set with (2*k*+1) × (2*k*+1) pixels (*k* is the number of pixels) in the reference image $f(x, y)$ (*i.e.*, image acquired before deformation), then to determine the corresponding subset location in the deformed image $g(x', y')$ based on the gray level information of the subset. One can notice here that this justify why the surface pattern must not be repetitive, otherwise the determined solution might not be unique. Thus, the displacement and strain can be obtained based on the change of subset location and shape in the two images.

In order to reach this goal, correlation calculations are required. Firstly, a set of suitable variables to represent the displacement and deformation of the subset in the reference image and the deformed image should be found. Secondly, a mathematical criterion should be established to evaluate the correspondence degree of two subsets: one in the reference image, the other one eventually strained and displaced image. Finally, using an efficient search algorithm, the displacement and strain of subset can be obtained by iterative calculation.

Shape functions

As shown in Fig. 1.3, a point $P(x_0, y_0)$ is in the reference image. To compute the displacement of point P, a reference subset centered at point $P(x_0, y_0)$ from the reference image is used to track its corresponding location in the deformed image. The reason why a square subset, rather than an individual pixel, is selected for matching is that the subset comprising a wider variation in gray levels will distinguish itself from other subsets, and can therefore be more uniquely identified in the deformed image.

The subset centered at point $P(x_0, y_0)$ moves to a location near point $P'(x_0', y_0')$. The displacement of point P on the x and y axes is u and v, respectively. Thus,

$$\begin{cases} x_0' = x_0 + u \\ y_0' = y_0 + v \end{cases} \tag{1.1}$$

Meanwhile, point $Q(x_i, y_i)$ represents any point around the point P in the reference subset, positional relationship between point P and point Q is given as follows:

$$\begin{cases} x_i = x_0 + \Delta x \\ y_i = y_0 + \Delta y \end{cases} \tag{1.2}$$

where Δx and Δy is the distance between point P and point Q on the x and y axes, respectively. If the point Q in the reference subset moves to point $Q'(x_i', y_i')$, thus an equation can be given as follows:

$$\begin{cases} x_i' = x_i + u_Q \\ y_i' = y_i + v_Q \end{cases} \tag{1.3}$$

Generally, the material imaged in the reference subset allows translation, rotation and shear. Thus, the displacement of point Q on the x and y axes (u_Q and v_Q) can be given by the first-order displacement gradient of point P:

$$\begin{cases} u_Q = u + \dfrac{\partial u}{\partial x}\Delta x + \dfrac{\partial u}{\partial y}\Delta y \\ v_Q = v + \dfrac{\partial v}{\partial x}\Delta x + \dfrac{\partial v}{\partial y}\Delta y \end{cases} \tag{1.4}$$

Substituting Eq. (1.4) into Eq. (1.3) yield

$$\begin{cases} x_i' = x_i + u + \dfrac{\partial u}{\partial x}\Delta x + \dfrac{\partial u}{\partial y}\Delta y \\ y_i' = y_i + v + \dfrac{\partial v}{\partial x}\Delta x + \dfrac{\partial v}{\partial y}\Delta y \end{cases} \tag{1.5}$$

Since point Q is any point in the subset, it is found from Eq. (1.5) that displacement of subset can be expressed by the displacement of the center point in the subset and its four derivatives ($u, v, \frac{\partial u}{\partial x}, \frac{\partial u}{\partial y}, \frac{\partial v}{\partial x}, \frac{\partial v}{\partial y}$).

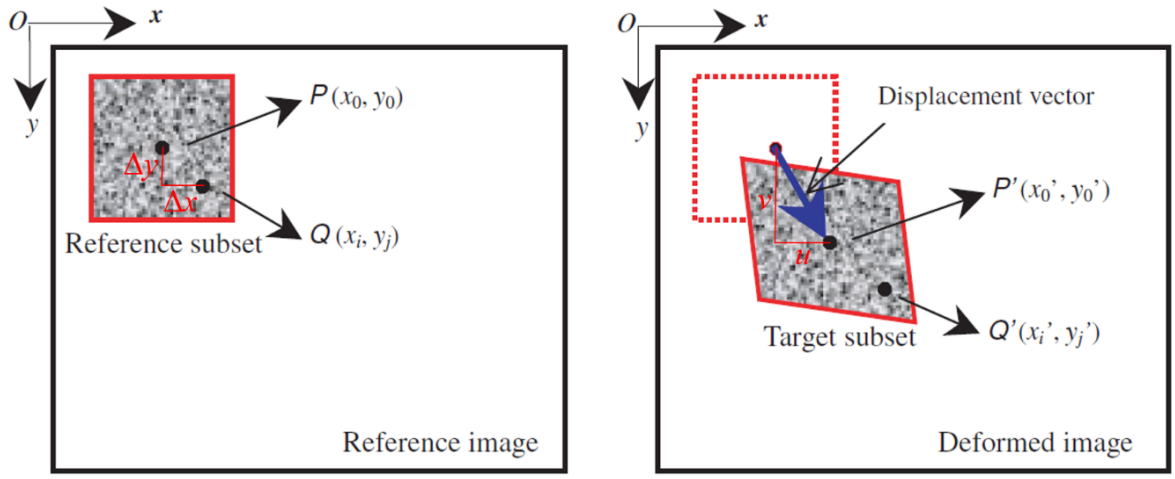

Fig. 1.3: Schematically illustration of a reference square subset before deformation and a target subset after deformation [PAN 10].

Correlation criterion

In order to evaluate the similarity degree between reference subset and deformed subsets, a correlation criterion should be given. To date, different correlation criteria are proposed. Generally, the correlation criteria involve two groups: Cross-correlation (CC) criteria and sum of squared differences (SSD) criteria. Three commonly used CC criteria are given as follows:

(1) Cross-correction (CC):

$$C_{CC} = \sum_{-k}^{k}\sum_{-k}^{k}\left[f(x,y)\cdot g(x',y')\right] \tag{1.6}$$

(2) Normalized cross-correction (NCC):

$$C_{NCC} = \frac{\sum_{-k}^{k}\sum_{-k}^{k}\left[f(x,y)\cdot g(x',y')\right]}{\left[\sum_{-k}^{k}\sum_{-k}^{k} f^2(x,y)\right]^{1/2}\cdot\left[\sum_{-k}^{k}\sum_{-k}^{k} g^2(x',y')\right]^{1/2}} \tag{1.7}$$

(3) Zero-normalized cross-correction (NCC):

$$C_{ZNCC}=\sum_{-k}^{k}\sum_{-k}^{k}\left\{\frac{\left[f(x,y)-f_m\right]\cdot\left[\mathrm{g}(x',y')-g_m\right]}{\left\{\sum_{-k}^{k}\sum_{-k}^{k}\left[f(x,y)-f_m\right]^2\right\}^{1/2}\cdot\left\{\sum_{-k}^{k}\sum_{-k}^{k}\left[\mathrm{g}(x',y')-g_m\right]^2\right\}^{1/2}}\right\} \tag{1.8}$$

where $fm=\frac{1}{(2k+1)^2}\sum_{-k}^{k}\sum_{-k}^{k}f(x,y)$ and $g_m=\frac{1}{(2k+1)^2}\sum_{-k}^{k}\sum_{-k}^{k}\mathrm{g}(x',y')$.

Three commonly used SSD criteria are given as follows:

(1) Sum of squared differences (SSD):

$$C_{SSD}=\sum_{-k}^{k}\sum_{-k}^{k}\left[f(x,y)-\mathrm{g}(x',y')\right]^2 \tag{1.9}$$

(2) Normalized sum of squared differences (NSSD):

$$C_{NSSD}=\sum_{-k}^{k}\sum_{-k}^{k}\left[\frac{f(x,y)}{\left\{\sum_{-k}^{k}\sum_{-k}^{k}\left[f(x,y)\right]^2\right\}^{1/2}}-\frac{\mathrm{g}(x',y')}{\left\{\sum_{-k}^{k}\sum_{-k}^{k}\left[\mathrm{g}(x',y')\right]^2\right\}^{1/2}}\right]^2 \tag{1.10}$$

(3) Zero-normalized sum of squared differences (ZNSSD):

$$C_{ZNSSD}=\sum_{-k}^{k}\sum_{-k}^{k}\left\{\frac{f(x,y)-f_m}{\left\{\sum_{-k}^{k}\sum_{-k}^{k}\left[f(x,y)-f_m\right]^2\right\}^{1/2}}-\frac{\mathrm{g}(x',y')-g_m}{\left\{\sum_{-k}^{k}\sum_{-k}^{k}\left[\mathrm{g}(x',y')-g_m\right]^2\right\}^{1/2}}\right\} \tag{1.11}$$

The basic principles of these correlation criteria are the same. Here, the normalized cross-correlation (NCC) is used to be analyzed as an example. The definition of NCC is given as follows:

$$C(x,y,u,v,\frac{\partial u}{\partial x},\frac{\partial u}{\partial y},\frac{\partial v}{\partial x},\frac{\partial v}{\partial y})=\frac{\sum_{-k}^{k}\sum_{-k}^{k}\left[f(x,y)\cdot\mathrm{g}(x',y')\right]}{\left[\sum_{-k}^{k}\sum_{-k}^{k}f^2(x,y)\right]^{1/2}\cdot\left[\sum_{-k}^{k}\sum_{-k}^{k}g^2(x',y')\right]^{1/2}} \tag{1.12}$$

where x, y are the coordinates of the center point in the subset; x', y' are the coordinates of any point in the subset and can be obtained by Eq. (1.5). When maximum value is achieved (*i.e.*, C=1), the subset in the deformed image are correlated with the reference subset in the reference image.

In correlation calculation, an optimization algorithm is normally adopted to find the minimum value. Thus, a correlation factor S is introduced:

$$S = 1 - C = 1 - \frac{\sum_{-k}^{k}\sum_{-k}^{k}[f(x,y)\cdot g(x',y')]}{\left[\sum_{-k}^{k}\sum_{-k}^{k} f^2(x,y)\right]^{1/2}\cdot\left[\sum_{-k}^{k}\sum_{-k}^{k} g^2(x',y')\right]^{1/2}} \tag{1.13}$$

It is clear from Eq. (1.13) that the smaller the S value, the greater the correlation between the two subset.

Search algorithm

A vector *J* is introduced to represent the displacement of subset, which is given as follows:

$$J = \left\{x, y, u, v, \frac{\partial u}{\partial x}, \frac{\partial u}{\partial y}, \frac{\partial v}{\partial x}, \frac{\partial v}{\partial y}\right\} \tag{1.14}$$

J_i (i = 1, 2, 3, 4, 5, 6) is used to represent the u, v, $\frac{\partial u}{\partial x}$, $\frac{\partial u}{\partial y}$, $\frac{\partial v}{\partial x}$, $\frac{\partial v}{\partial y}$. Thus, the correlation calculation is to find the minimum of objective function $S(J_1, J_2, J_3, J_4, J_5, J_6)$. It is obvious that the necessary condition for *S* to achieve the minimum value is that its first-order derivative is equal to zero.

$$\frac{\partial S}{\partial J_i} = 0 \tag{1.15}$$

For this optimization problem, there are many numerical methods, such as Newton-Raphson, etc. When the *S* achieves the minimum value, we can obtain the displacement and deformation of the subset from the J_i values.

The aforementioned processes are the basic principles of local image correlation method, in which a small region of interest (i.e., the aforementioned reference sub-set) is chosen to be treated, as shown in Fig. 1.3. The main limitation of the local method is that the process can induce large fluctuations from one image to the other (from speckle and the variation of lighting).

The global image correlation method is better than the local method to avoid the limitations of the local method mentioned above [HIL 12]. The global method relies on the entire image to determine the displacement field based on a mesh and shape functions [BES 06]. The basic principles of global method will be described in Chapter 4, in which the global image correlation method will be performed by Finite element in our study.

1.2 Measurement of thermal fields

Temperature measurement is an important topic in many fields, especially high temperature measurement in aerospace, materials, energy, metallurgy and other high-tech fields. To measure the temperature, many techniques are available, which can be classified into two categories: (1) contact measurement techniques, the sensor is sealed on the surface or embedded into the material like thermocouples [GEN 09][BLO 80], thermistors[KIM 11], resistance temperature detectors [BLA 15],

etc. These sensors are well known, cheap and robust, but they provide a point information. Moreover, they fatally cause a disturbance in the observed phenomenon; (2) contactless measurement methods, the sensor exploits the change in radiation from the surface due to thermal change of the observed object. It can be a single point measurement like for infrared pyrometers or multisite sensors like becoming real cameras (infrared thermography) [PER 17][WAN 11][AST 06], etc.

The following subsections focus on the infrared thermography as a method of full thermal field measurement. Firstly, a general introduction of the infrared thermography is given. Then a brief introduction of the notion of thermometry, and particularly to the infrared thermometry, is proposed.

1.2.1 Introduction of infrared thermography

Infrared thermography (IRT) is an advanced real-time, non-contact, high speed response and full field measurement technique, which transforms the thermal radiation, emitted by objects in the infrared wavelength of the electromagnetic spectrum, into an electronic video signal with a resolution depending on the physical size of each pixel and of the whole sensor. IRT has some advantages:

(1) Non-contact measurement

Due to the infrared radiation of object surface being measured, it is unnecessary to touch the objects and it will not interfere with the thermal balance of the object. Therefore, this technique is very suitable for measuring moving or dangerous objects.

(2) Full field measurement

IRT outputs the full field temperature distribution of object surface, which not only provides complete information, but also is visually intuitive. In the mechanics of materials, it is particularly relevant for the observation of localized phenomena like localized phase transformation, cracking or damaging.

(3) High-speed response

The response time of conventional temperature measurement techniques (such as thermocouple) is in seconds, while the response time of IRT is in milliseconds or even microseconds. Thus, IRT is relevant for the observation of transient phenomena.

Development of the use of infrared thermography

The IRT was firstly used in the military. In World War II, Germans used infrared imaging tubes as photoelectric conversion devices to develop night vision devices and infrared communication devices [LIS 11]. After World War II, many countries have conducted extensive researches on the use of IRT in the military field. In late 1950s Texas instruments and the US Military developed the first single element detectors, which allowed the scanning of scenes and produced line images. In the late 1960s infrared camera was commercialized and thermal imaging became accessible to a wider audience, and not only to the military [BAR 12]. As the technology advances and matures, the application of IRT has been expanded to other fields.

In the medical field, measuring the temperature of the human body can contribute to both disease diagnosis and treatment planning. For example, IRT can be used for the diagnosis of superficial human body tumors such as malignant melanoma [DI 2003]. IRT can provide real-time information for the surgeon to assist him in decision making in the heart surgery [Ruddok 2003]. IRT is used in many other medical applications, such as the diagnosing of diabetic neuropathy or vascular disorders [RIN 10], fever screening [NGU 10], dentistry and dermatology [HAN 04], et al.

In the industrial field, IRT is an effective predictive maintenance tool. For example, IRT can be used to detect abnormal temperature patterns, thereby indicating faulty connections [CHO 09]. IRT can also be used in other areas of the maintenance and process monitoring field, such as monitoring of deformation [BAD 11], fatigue damage [LUO 98][PAS 08][WAN 00], welding [MEO 04][KAF 11][LAH 11], nuclear product monitoring [BLA 89][ITA 04], aerospace maintenance [FAV 95][MEN 06], et al.

For civil engineering applications, the temperature measurement of the facade of buildings can provide important information to discover many hidden conditions. For example, IRT is used to detect where and how energy is leaking from a building envelope. Besides the detection of heat loss, it can also be used to discover other anomalies, such as water infiltration and moisture [BOM 78][LJU 94] . A wet mass in a wall with the differentiated thermal inertia can be discovered by IRT. IRT is used for sub-surface moisture detection in masonry structures [MAI 09] and for moisture mapping in ancient buildings [GRI 02].

The applications of IRT are not limited to medicine, maintenance and buildings. Nowadays, this technique has been applied to various fields.

1.2.2 Fundamentals of infrared thermography

Random movements of molecules and atoms exist in any object above absolute zero, which emits thermal radiation. The more intense the movement of molecules and atoms is, the greater the energy is. The infrared wavelength range is approximately 0.76-1000 μm, which is between visible light and microwaves in the electromagnetic spectrum, as shown in Fig. 1.4. Much of infrared range of the electromagnetic spectrum is difficult to be used in IRT due to the lack of permittivity of the atmosphere and optical set-up concerning these typical wavelengths. Fig. 1.5 shows the atmospheric transmittance for different wavelengths. It is clear that the usable parts of the infrared for IRT involves: (1) Near-infrared (NIR) from 0.76 μm to 1.7 μm; (2) Short-wavelength infrared (SWIR) from 1.7 μm to 2.5 μm; (3) Mid-wavelength infrared (MWIR) from 3 μm to 5 μm; (4) Long-wavelength infrared (LWIR) from 8 μm to 14 μm. Infrared radiation has a strong temperature effect. The higher the temperature of the object is, the stronger the infrared radiation energy is. Therefore, the temperature of the object surface can be obtained by measuring the infrared radiation energy. This is the theoretical basis for IRT.

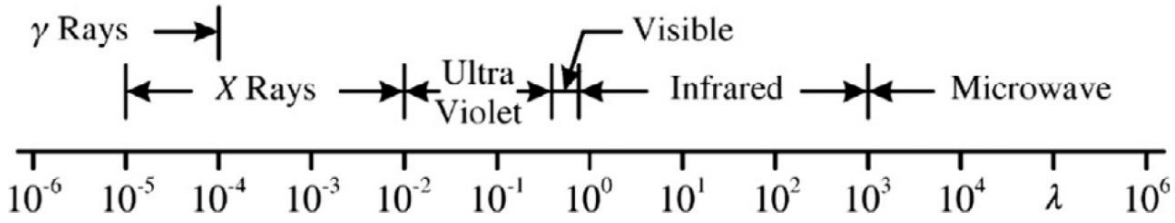

Fig. 1.4: Electromagnetic spectrum (wavelength λ in micrometers) [CEN 97].

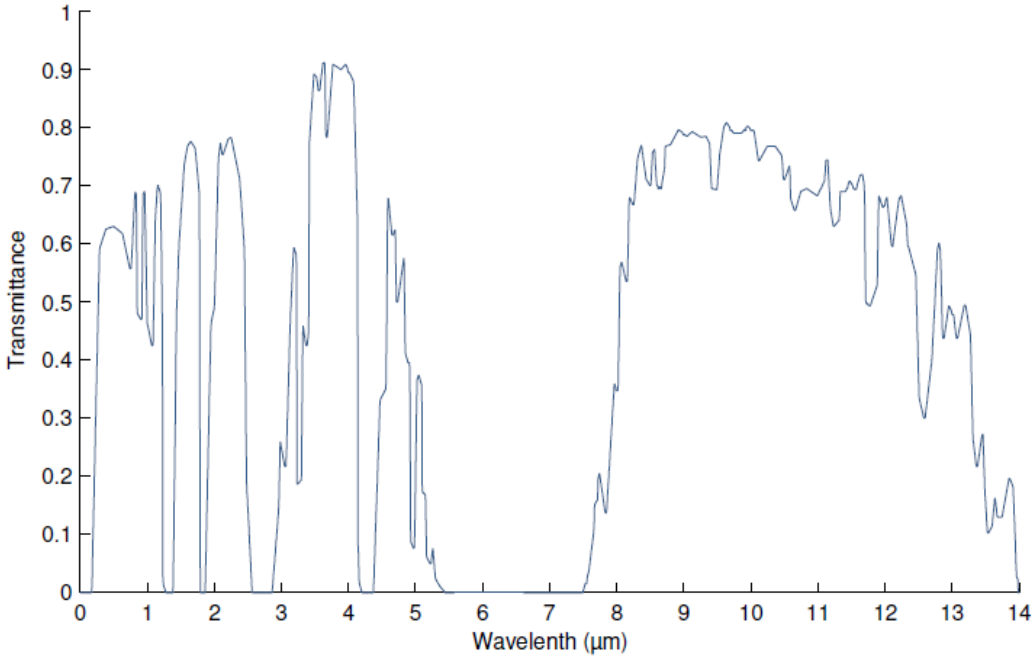

Fig. 1.5: Atmospheric transmittance at one nautical mile, 15.5℃, 70% relative humidity and at sea level [USA 14].

In the early 1800s, the English physicist William Herschel discovered thermal radiation outside the deep red in the visible spectral ranges, and this invisible light called infrared. After the observation of the infrared, many great scientists, such as Max Planck, Ludwig Boltzmann, Gustav Kirchhoff, James Clerk Maxwell, Joseph Stefan, Macedonio Melloni, et al., have made great contributions to IRT. Nowadays, IRT has become a useful technique to obtain the full field temperature distribution on the object surface.

The blackbody is an idealized physical body that absorbs all incident electromagnetic radiation, regardless of frequency or angle of incidence. Thus, blackbody can be used as a standard for radiation energy and is widely used for the calibration of infrared devices. In reality, the absolute blackbody does not exist. In 1860, Kirchhoff opened a small hole in an isothermally closed cavity. When the light entered the cavity through the small hole, it was reflected multiple times in the cavity, and was quickly absorbed

and attenuated. Finally, only a very small proportion of the radiation could emit from the small hole, as schematically shown in Fig. 1.6. This is the artificial blackbody.

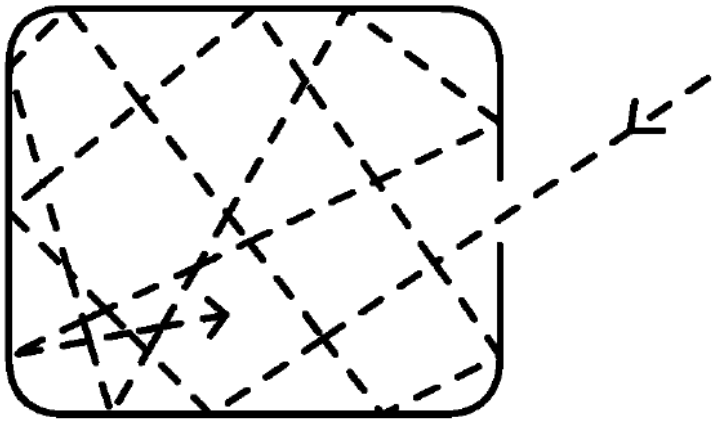

Fig. 1.6: Blackbody model [ROB 09].

The spectral characteristics of the blackbody are measured, and the curve of the spectral radiation emission as a function of wavelength is shown in Fig. 1.7. It can be seen from the figure that there is a maximum value corresponding to each temperature, and the blackbody radiation increases rapidly with the increase of temperature. The maximum value of the curve is also gradually moved to the short wave side with the increase of temperature.

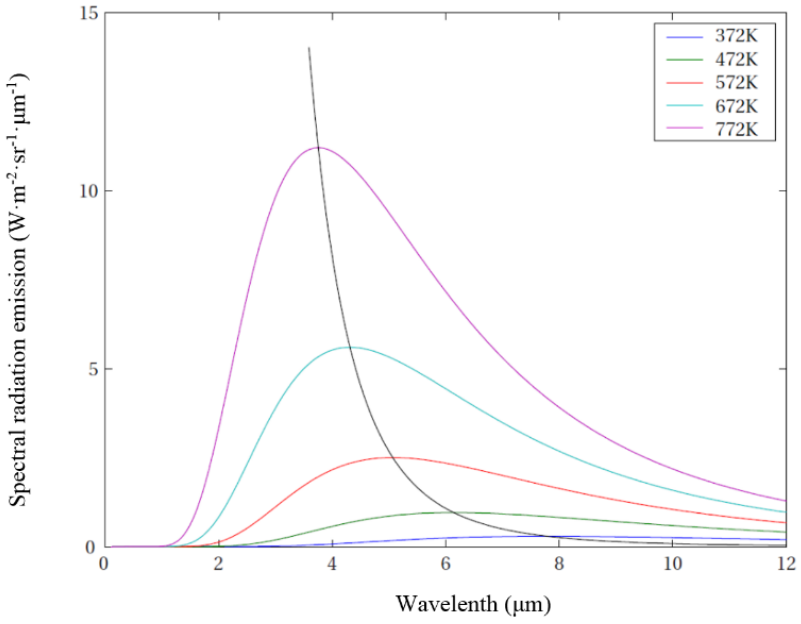

Fig. 1.7: Special radiation versus wavelength [ROT 06a].

(1) Planck's law

In 1990, Planck proposed the energy quantization hypothesis to theoretically explain the blackbody radiation curve in Fig. 1.7. Planck thought that the radiation can be perceived as a collection of discrete particles termed 'photons' or 'quanta', where each photon has energy e (J) [MAH 05][CEN 97]:

$$e = h\nu = h\frac{c}{\lambda} \tag{1.16}$$

where h is Planck's constant (h = 6.6262×10^{-34} J·s); ν is the frequency of wave (s^{-1}), c is the light speed (c = 2.9979×10^{8} m·s^{-1}), and λ is wavelength (m). It is apparent that while both c and λ depend on the medium through which the wave travels, ν is constant because the energy of the photon must be conserved. The Planck's radiation law can be given as follows [MAH 05][CEN 97]:

$$M(\lambda,T) = \frac{c_1}{\lambda^5}\left(e^{\frac{c_2}{\lambda T}} - 1\right)^{-1} \tag{1.17}$$

where $M(\lambda,T)$ is the spectral radiance of blackbody (W·cm^{-2}·μm^{-1}); c_1 is the first radiation constant ($c_1 = 2\pi hc^2$ = 3.7415×10^{-16} W·m^2); c_2 is the second radiation constant ($c_2 = \frac{hc}{k}$ = 1.44×10^{-2} m·K), k is the Boltzmann's constant (k = 1.38054×10^{-23} W·s·K^{-1}).

For any temperature, a radiation curve can be plotted using Planck's law. It is clear from any Planck curve that the spectral radiance is equal to zero when the wavelength is zero, the maximum value of spectral radiance can be obtained at the peak wavelength, and the spectral radiance approaches zero as the wavelength is extremely large. Planck's law is the basis for all quantitative calculation of infrared radiation.

(2) Wien's displacement law

From the radiation curve of blackbody shown in Fig. 1.7, it is apparent that the maximum value of spectral radiance is obtained at the peak wavelength (λ_m), and this peak wavelength moves to lower wavelength with the increase of temperature (as indicated by black curve in Fig. 1.7). The higher the temperature is, the shorter the peak wavelength is. For example, during the heating process of metal, at the beginning the long wavelength of infrared cannot be seen by human eye. As the temperature increases, the radiation wavelength becomes shorter, so that the human eye can see it. By differentiating Planck's law with respect to λ to find the peak wavelength, the Wien's displacement law can be given as follows:

$$\lambda_m = \frac{2898\mu \cdot K}{T} \tag{1.18}$$

As seen from the Eq. (1.18), in room temperature (300 K), peak wavelength falls in the infrared spectral range. Only when the temperature is higher than 3864 K, the peak wavelength is approximately equal to 0.75 μm, which moves to the visible light.

(3) Stefan-Boltzmann's law

By integrating Planck's law over the entire spectrum ($\lambda = 0 \sim \infty$), the total hemispherical radiation intensity of blackbody M_B can be given as follows:

$$M_B = \int_0^\infty M(\lambda,T)d\lambda = \int_0^\infty \frac{c_1}{\lambda^5}\left(e^{\frac{c_2}{\lambda T}}-1\right)^{-1} d\lambda = \sigma T^4 \tag{1.19}$$

where σ is the Stefan-Boltzmann's constant ($\sigma =$ 5.670 $\times$ 10^{-8} W·m^{-2}·K^{-4}). This is the Stefan-Boltzmann's law. This law indicated that the total hemispherical radiation intensity of blackbody per unit surface area in a unit time is proportional to the fourth power of the absolute temperature.

The blackbody is an ideal radiator, but in reality the ideal blackbody does not exist. The real objects only emit part of the radiation that a blackbody emits at the same temperature and same wavelength. Here, the emissivity, which is defined as radiation of real objects $M_R(\lambda,T)$ normalized by radiation of the blackbody $M_B(\lambda,T)$ at the same temperature and same wavelength, is introduced:

$$\varepsilon_{\lambda,T} = \frac{M_R(\lambda,T)}{M_B(\lambda,T)} \tag{1.20}$$

The emissivity of the object depends on the materials and the surface state of the object. The emissivity of the blackbody is equal to 1, while the emissivity of real objects is always between 0 and 1. If the emissivity of an object at a certain temperature is known, the radiation of this real object at this temperature can be expressed by the Planck's law and the emissivity:

$$M_R(\lambda,T) = \varepsilon \cdot \frac{c_1}{\lambda^5}\left(e^{\frac{c_2}{\lambda T}}-1\right)^{-1} \tag{1.21}$$

Based on the Stefan-Boltzmann's law, the radiation of this real object can also be given as follows:

$$M_R(\lambda,T) = \varepsilon \cdot \sigma T^4 \tag{1.22}$$

This Eq. (1.22) is the theoretical basis of IRT.

1.2.3 Infrared thermometry

As mentioned above, any real object has surface emissivity. Thus, the problem of surface emissivity cannot be ignored in the infrared thermometry. In reality, several common methods of infrared thermometry are proposed to deal with this problem. The common methods involve total radiation thermometry, radiance thermometry and dual wavelength thermometry.

(1) Total radiation thermometry

The basic principle of total radiation thermometry is that the total spectral radiance of the object within the entire spectral ranges ($0<\lambda<\infty$) is firstly measured, then the temperature of the object is calibrated by the same spectral radiance of the blackbody. That is, when the object to be measured with

a temperature T and the blackbody with a temperature T_b have the same total spectral radiance in the entire spectral ranges, the blackbody temperature T_b is defined as the radiant temperature of the object.

Based on the Stefan-Boltzmann's law, the total spectral radiance of blackbody with the temperature T_b can be given as follow:

$$M_b = \sigma T_b^4 \tag{1.23}$$

Also the total spectral radiance of the object with the temperature T can be given as follow:

$$M = \varepsilon \cdot \sigma T^4 \tag{1.24}$$

Based on the assumption of total radiation thermometry, an equation can be given as follow:

$$M_b = M \tag{1.25}$$

Substituting Eqs. (1.23) and (1.24) into Eq. (1.25), the temperature of the object is

$$T = \frac{T_b}{\sqrt[4]{\varepsilon(T)}} \tag{1.26}$$

The real temperature of object T is in fact higher than its radiant temperature T_b because the emissivity of the object is less than 1.

In reality, the detectors cannot acquire the entire spectral ranges. Thus, only a reduced part of spectral range is measured in practical applications of total radiation thermometry. That is, the spectral radiance of the object within a certain spectral range ($\lambda_1<\lambda<\lambda_2$) can be expressed by:

$$M = \int_{\lambda_1}^{\lambda_2} M(\lambda, T) d\lambda \tag{1.27}$$

Meanwhile, the spectral radiance of the blackbody within the same spectral ranges ($\lambda_1<\lambda<\lambda_2$) can be also calculated, and the temperature of the blackbody is defined as the radiant temperature of the object. Thus, the temperature of the blackbody can be given as follows:

$$T_b = \sqrt[4]{\frac{\int_{\lambda_1}^{\lambda_2} M(\lambda, T) d\lambda}{\sigma}} \tag{1.28}$$

Based on the Eq. (1.26), the temperature of the object surface can also be obtained as follows:

$$T = \sqrt[4]{\frac{\int_{\lambda_1}^{\lambda_2} M(\lambda, T) d\lambda}{\sigma\varepsilon(T)}} \tag{1.29}$$

It should be noticed, reading the Eq. (1.29), that emissivity in the measured spectral range should be known to obtain the true temperature of the object surface. The measurement error is mainly related to the estimation error of the emissivity. The smaller the surface emissivity is, the larger the error is.

(2) Radiance thermometry

The basic principle of radiance thermometry is that the infrared devices is used to measure the illumination from the object, then the temperature of the object is calibrated by the same illumination

from a blackbody. Indeed, when the observed object has a temperature *T*, the output illumination of this object *V* can be given based on Wien's approximation:

$$V = K_\lambda \varepsilon(\lambda, T) \lambda^{-5} \cdot e^{-\frac{C_2}{\lambda T}} \tag{1.30}$$

where K_λ is a constant of the device at given wavelength. Meanwhile, the same device is used to obtain the same illumination of a blackbody *V* with a temperature T_b:

$$V = K_\lambda \lambda^{-5} \cdot e^{-\frac{C_2}{\lambda T_b}} \tag{1.31}$$

Combining Eq. (1.30) and Eq. (1.31), the temperature of object can be obtained as follows:

$$\frac{1}{T} = \frac{1}{T_b} + \frac{\lambda}{C_2} \ln \varepsilon \tag{1.32}$$

The above equation is derived from a monochromatic spectrum of wavelength λ. In realistic measurement, it is carried out within a certain narrow spectral range. The emissivity of the object near the spectral ranges should be known to get the true temperature of object surface. If the emissivity is unknown, the temperature T_b is considered to be the true temperature but an error will be introduced. Nonetheless, this error is smaller than that of total radiation thermometry.

(3) Dual wavelength thermometry

The aforementioned two thermometries are affected significantly by the emissivity of the object surface. In order to reduce the influence of the lack of knowledge on the emissivity of the object surface, the dual wavelength thermometry is proposed. The basic principle of dual wavelength thermometry is that the spectral radiation ratio of the object at two given wavelengths λ_1 and λ_2 is measured. Then the temperature of the object is calibrated by the same spectral radiation ratio of the blackbody. When the observed object has a temperature *T*, two output illuminations of this object V_1 and V_2 can be given for two given wavelengths λ_1 and λ_2:

$$V_1 = K_{\lambda_1} \varepsilon_1 \lambda_1^{-5} \cdot e^{-\frac{C_2}{\lambda_1 T}} \tag{1.33}$$

$$V_2 = K_{\lambda_2} \varepsilon_2 \lambda_2^{-5} \cdot e^{-\frac{C_2}{\lambda_2 T}} \tag{1.34}$$

where $K_{\lambda 1}$ and $K_{\lambda 2}$ are two constants of the device at two given wavelength, respectively. A ratio *R* is introduced as:

$$R = \frac{V_1}{V_2} = \frac{K_{\lambda 1} \varepsilon_1 \lambda_1^{-5} \cdot e^{-\frac{C_2}{\lambda_1 T}}}{K_{\lambda 2} \varepsilon_2 \lambda_2^{-5} \cdot e^{-\frac{C_2}{\lambda_2 T}}} \tag{1.35}$$

It is apparent from Eq. (1.35) that the temperature of object *T* is directly linked to the ratio *R*. If the ratio *R* can be obtained by blackbody calibration, the temperature of the object can also be obtained. This method is also named as two-color thermometry.

When the same device is used to measure the temperature of blackbody T_b, the ratio *R* is:

$$R = \frac{V_1'}{V_2'} = \frac{K_{\lambda 1}\lambda_1^{-5} \cdot e^{-\frac{C_2}{\lambda_1 T_b}}}{K_{\lambda 2}\lambda_2^{-5} \cdot e^{-\frac{C_2}{\lambda_2 T_b}}} \tag{1.36}$$

Combining Eq. (1.35) and Eq. (1.36), the temperature of the object can be obtained as follows:

$$\frac{1}{T} = \frac{1}{T_b} + \frac{\ln \varepsilon_2 - \ln \varepsilon_1}{C_2\left(\lambda_2 - \lambda_1\right)}\lambda_1\lambda_2 \tag{1.37}$$

It can be found from Eq. (1.37) that the temperature T_b is equal to the true temperature T when the object is a gray body (the emissivity of gray body does not change with the variation of wavelength. Thus, measurement accuracy can be very high when dual wavelength thermometry is used to measure the temperature of the gray body. When the dual wavelength thermometry is used to measure the temperature of non-gray body, the larger the distance between λ_1 and λ_2, the larger the error. Two wavelengths with small distance between them are generally chosen in the realistic measurement.

1.2.4 Infrared thermal imaging

The infrared cameras can measure the infrared radiation emitted by an object and convert the energy detected into an image. In practical applications, not all of the radiation received comes from the target object. The radiation may come from other sources, such as surrounding objects, atmosphere, which should be removed in the conversion to temperature. Fig. 1.8 shows a thermographic analysis of the heat transfer processes. The total radiation received by the infrared camera (W_{tot}) comes from three sources: the radiation emitted by target object (W_{obj}), the radiation reflected, emitted by the surrounding objects (W_{refl}) and the radiation absorbed by the atmosphere (W_{atm}). The energy balance can be given as follows:

$$W_{tot} = \varepsilon\tau W_{obj} + \left(1-\varepsilon\right)\tau W_{refl} + \left(1-\tau\right)W_{atm} \tag{1.38}$$

where τ is transmittance of the atmosphere. To obtain the temperature of the object, some information should be known: object emissivity, reflected temperature, atmosphere temperature, the transmittance of the atmosphere.

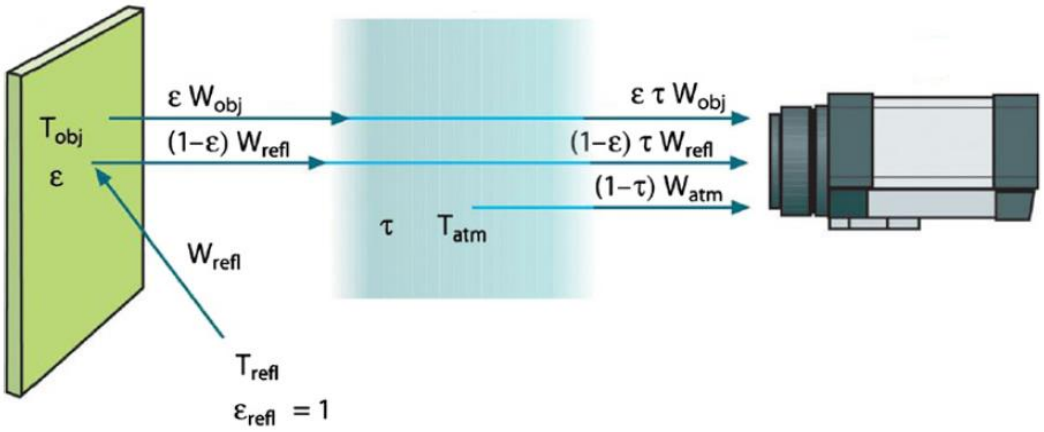

Fig. 1.8: IRT: schematization of the heat transfer processes [ASD 02].

1.3 Current status of coupling kinematic and thermal fields

Many experimental processes require observing both kinematic and thermal information in several points or even on a large area of interest. Especially in experimental mechanics (mechanical tests such as fatigue, fracture, impact, etc.) and materials science (materials characterization, or materials processing such as welding, forming, heat treatment, etc.), the deformation and temperature of the specimens or components are two most important parameters, which are necessary to be known. If both kinematic and thermal full fields can be obtained at the same spatial and temporal coordinates, it can offer invaluable experimental data for these thermo-mechanical procedures. DIC and IRT are two good candidates for obtaining both kinematic and thermal full fields. Many researchers have contributed to integrating both kinematic and thermal fields. The following subsections will present the common methods that have been proposed to simultaneously measure these two fields.

1.3.1 Combination of two imaging systems

The more commonly used method to obtain simultaneously the kinematic and thermal fields is to use two different imaging systems: kinematic fields acquired by silicon-based camera and thermal fields acquired by infrared camera. Then, a *posteriori* data processing is conducted to integrate the space and time associations of these two fields. Some scholars used silicon-based camera and infrared camera to observe two different surfaces of the specimen. Srinivasan et al. [SRI 12] studied the Lüders deformation in the welded mild steel during uniaxial tensile testing, as schematically shown in Fig 1.9. In their experiment, an infrared camera was used to observe the thermal fields of one surface with black coating, and a silicon-based camera was used to observe the kinematic fields of another surface with speckle

pattern. The same method was used by Wang et al. [WAN 17] to observe the kinematic and thermal characteristics of Lüders and Protevin-Le Châtelier bands in a medium Mn transformation-induced plasticity steel. Chrysochoos et al. [CHR 10] investigated the mechanical energy and heat sources involved locally during a heterogeneous thermal tensile tests of materials using data supplied by DIC and IRT. These two techniques are performed on different surfaces of the specimen by a CCD camera and an infrared camera. As shown in Fig. 1.10, Wang et al. [WAN 16] also used this two-face measurement configuration to investigate the plastic deformation of a pure aluminum oligocrystal sheet in a tensile test by measuring the kinematic and thermal fields on the two different surfaces of the sheet. Favier et al. [FAV 17] also used two-face measurement configuration to observe the kinematic and thermal fields on the surface of austenitic polycrystalline Ti-50.8 at.% Ni thin tube under tension test. In their tests, the thin geometries of the specimens (such as sheets, plates, or wires) were commonly used to ensure that the temperature and the displacements are constant through the specimen thickness. One surface of the specimen was sprayed by the black-white paints, which could provide a heterogeneous surface with randomly distributed speckle pattern for digital image correlation. Another one was sprayed by single black or white paint, which could provide a homogeneous surface with constant surface emissivity for IRT purpose. Although this two-face measurement experimental set-up solves the problem that DIC and IRT have different requirements for coatings of the surfaces to be observed, the problem of time and space association still remains and this method is only suitable for some thin specimens.

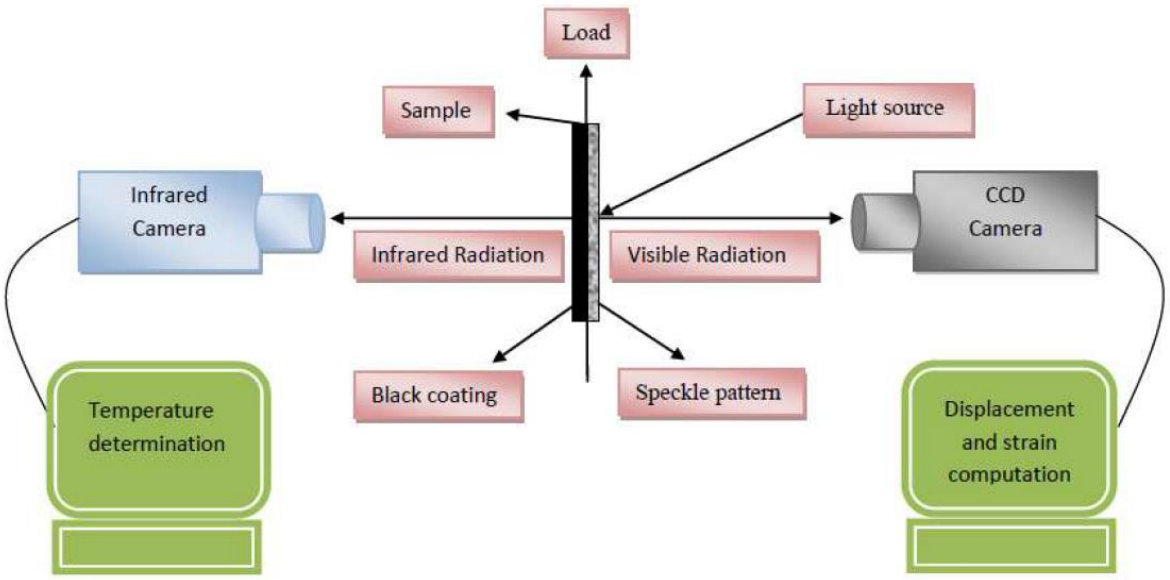

Fig. 1.9: Schematic of Srinivasan's experimental set-up [SRI 12].

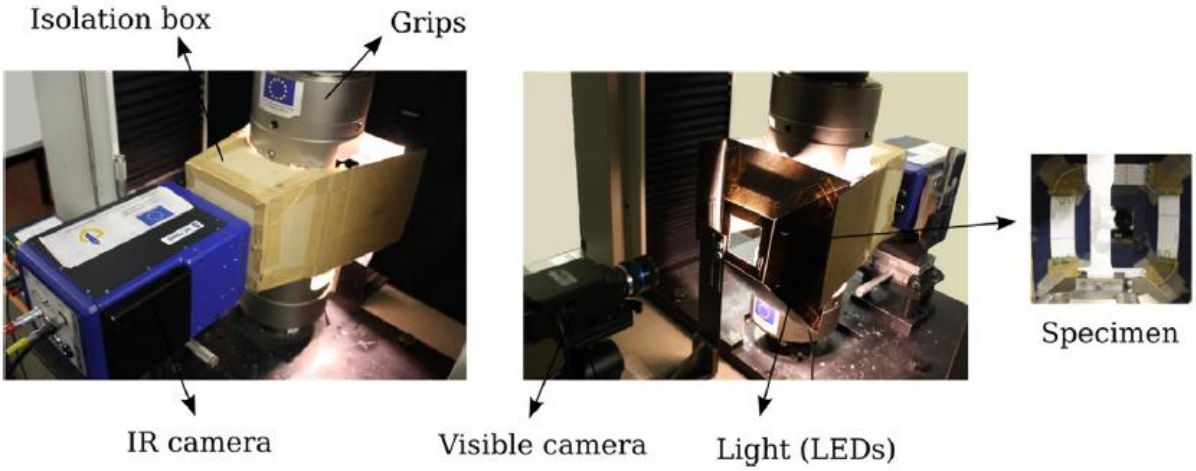

Fig. 1.10: Wang's two-face measurement experimental set-up [WAN 16].

Some other scholars performed both DIC and IRT on the same surface by using two imaging devices. Harzallah et al. [HAR 18] proposed a bi-spectral imaging apparatus with a cold mirror (as shown in Fig. 1.11), which enabled imaging at two different wavelengths: one dedicated to visible images for DIC purpose and the other to infrared images for IRT purpose. Using this apparatus, the kinematic and thermal fields on the same surface with speckle pattern in orthogonal cutting experiment can be simultaneously measured. Similarly, a "filter-mirror" (dichroic mirror) was used by Bodelot et al. [BOD 09] to separate the infrared radiation and visible radiation for simultaneous observation of kinematic and thermal fields in the same zone at the microstructure scale of an AISI 346L austenitic stainless steel specimen during tensile test, as shown in Fig. 1.12. Louche et al. [LOU 12] directly used a visible camera and an infrared camera to observe kinematic and thermal fields on the same NiTi alloy specimen surface with speckle during tensile test, as shown in Fig. 1.13. The similar methods have also used by other scholars [GOI 13][DAT 13][KRS 15]. In their tests, the temporal synchronization and spatial synchronization of these two fields were performed. Nowak and Maj [NOW 18] provided a detailed description of the numerical procedures for determining coupled thermomechanical fields based on the experimental data obtained from two cameras (silicon-based camera and infrared camera).

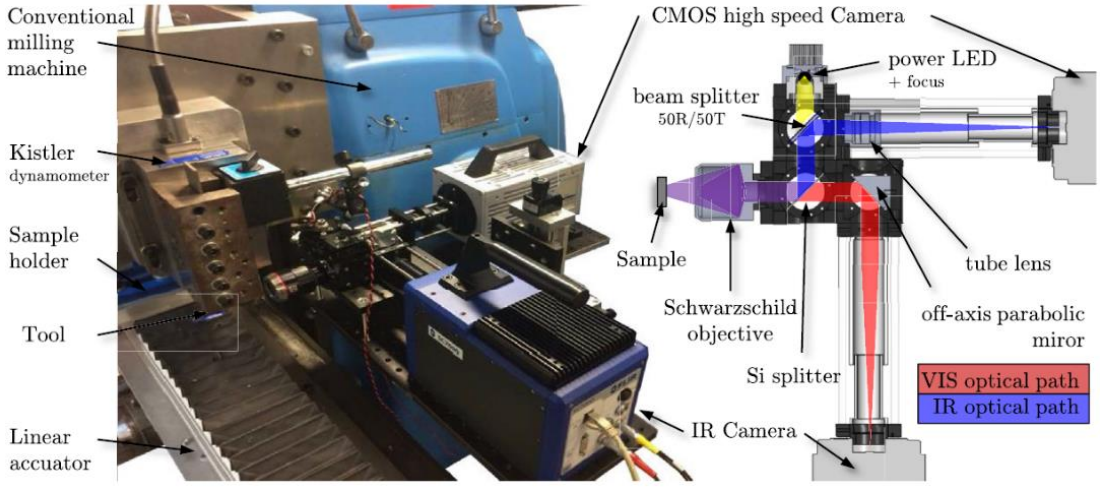

Fig. 1.11: Orthogonal cutting device and imaging apparatus (left) and schematic of the visible-infrared imaging apparatus (right) [HAR 18].

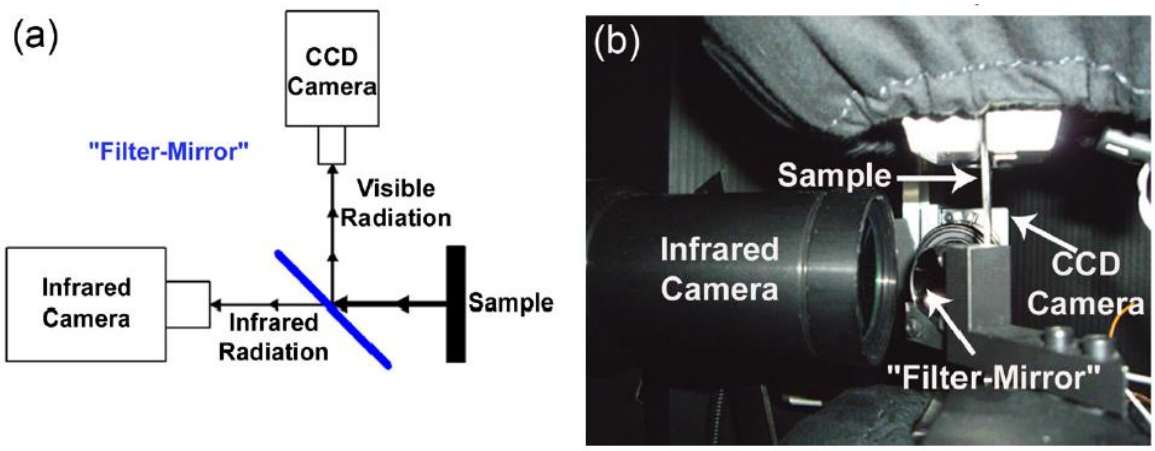

(a) Schematic of the imaging apparatus. (b) Experimental set-up

Fig. 1.12: Schematic of the imaging apparatus and experimental set-up [BOD 09].

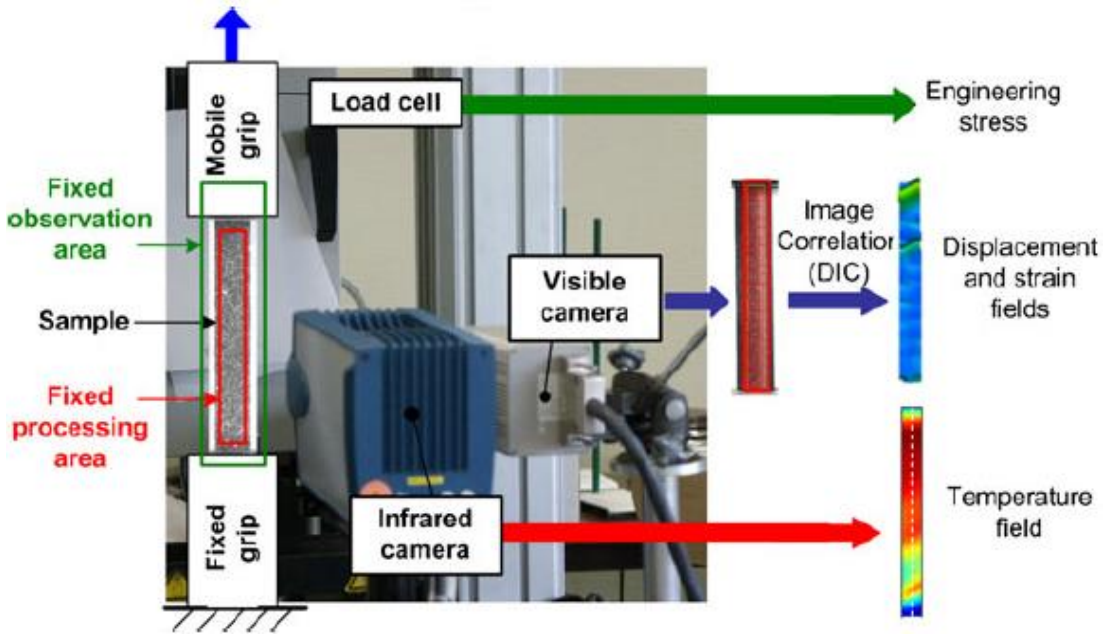

Fig. 1.13: Experimental set-up of tensile tests of superelastic NiTi shape memory alloys [LOU 12].

However, from the experimental point of view, this method has several essential problems which are difficult to be solved:

(1) The two different imaging devices (silicon-based camera and infrared camera) have different spatial resolution and acquisition rates. The exact same spatial and temporal coordinates of kinematic and thermal fields cannot be perfectly achieved no matter how well *posteriori* data processing is done.

(2) The two techniques (DIC and IRT) have conflicting requirements for the specimen surface. DIC needs a heterogeneous and contrasting texture on the specimen surface, which is easily tracked to perform the kinematic fields. But the IRT needs a homogeneous and constant emissivity on the surface, of which the temperature can be accurately measured with little influence of emissivity variation.

(3) The combination of these two imaging systems is expensive and uneasy. Complicated experimental set-up should be conducted to combine these two imaging systems by special expensive filters and other installations due to the different spectral ranges acquired by these two systems. The too much extra devices are not easy to be installed around the specimens in the tests, especially if the specimen has complex motion trajectory.

1.3.2 Single imaging device for both fields measurement

To avoid the aforementioned problems induced by two imaging systems, a few researchers tried to obtain both kinematic and thermal fields using a single camera. Maynadier et al. [MAY 12] proposed the infrared image correlation (IRIC) technique to access to both kinematic and thermal fields decomposed over the same time and space discretization using single apparatus: an infrared camera (shown in Fig. 1.14). It was applied to capture localized transformation bands of shape memory alloy

under tension. Nevertheless, this technique, based on the infrared camera (usually operating in the middle wave infrared spectral range of 3-5 μm or 8-12 μm), delivered rather poor resolution fields (only 320×240 pixels to be exploited) and the temperature explored is limited to [20; 60]℃ in this publication. In addition, the infrared cameras are expensive and difficult to be used. Thus they are mostly confined to the laboratory research. Compared with infrared cameras, silicon-based cameras are cheaper, present lower noise, possess a longer durability and have major advantage to deliver a far higher resolution (about 4800×3600 pixels), so they are widely used for industrial applications. The most important point is that the cameras equipped with silicon detectors (CCD or CMOS), which are widely used to perform real-time observation of the kinematic fields thanks to digital image correlation, are not only operating in the visible spectrum (0.4-0.75 μm), but are also sensible in near-infrared spectral range (0.75-1.1 μm). This indicates that silicon-based camera can also be used to measure the temperatures higher than about 573 K. Thus, they are good candidates to measure both kinematical and thermal fields if the sensors are properly calibrated.

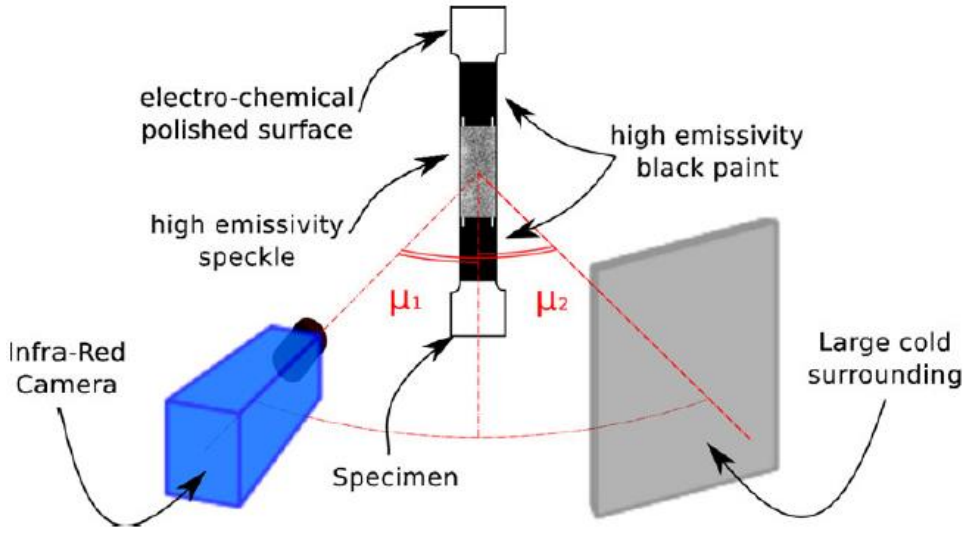

Fig. 1.14: Kinematic and thermal fields measurement experimental set-up using a single infrared camera [MAY 12].

Moreover, the silicon-based cameras have some special advantages over infrared cameras when the thermography is conducted. Firstly, the disturbance from the surrounding radiation to the measurement of thermal fields by silicon-based cameras in the near-infrared spectral ranges is much less than that by infrared camera in the middle infrared spectral ranges. The disturbance radiation from the surrounding objects is an important issue in infrared thermography and the correction process is very difficult. This problem will be amplified when the observed surface has low emissivity due to the high reflectivity. Teyssieux et al. [TEY 07] [TEY 08] compared the influence of different wavelength on the disturbance radiation from surrounding objects by introducing the normalized ratio

($NR = {R_O - R_a}/{R_O}$), where R_O is the radiation of the object to be observed, R_a is the surrounding radiation reflected by other objects. Fig. 1.15 shows the relationship among wavelength, temperature and normalized ratio at a given emissivity of 0.25. It indicates that the disturbance radiation from surrounding objects is slight and can be negligible when the wavelength is less than 2 μm, while the disturbance radiation from surrounding objects is obvious when the wavelength is greater than 2 μm.

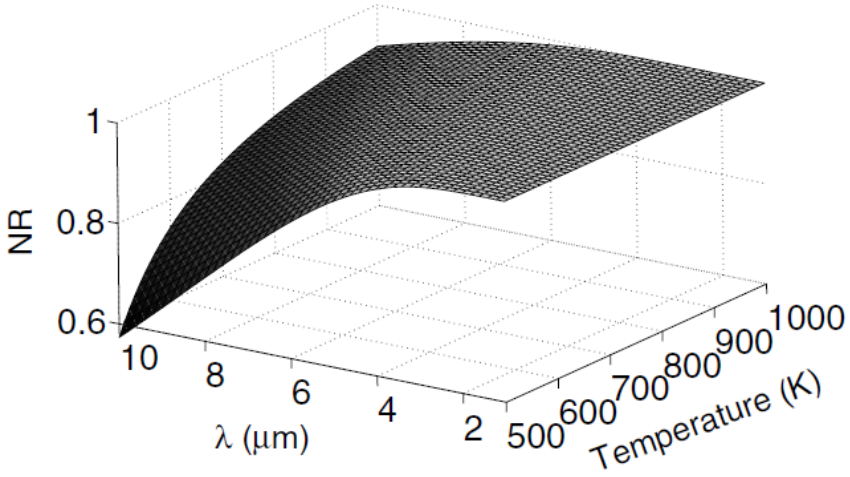

Fig. 1.15: Relationship among normalized ratio NR, temperature and wavelength at a given emissivity of 0.25. [TEY 08].

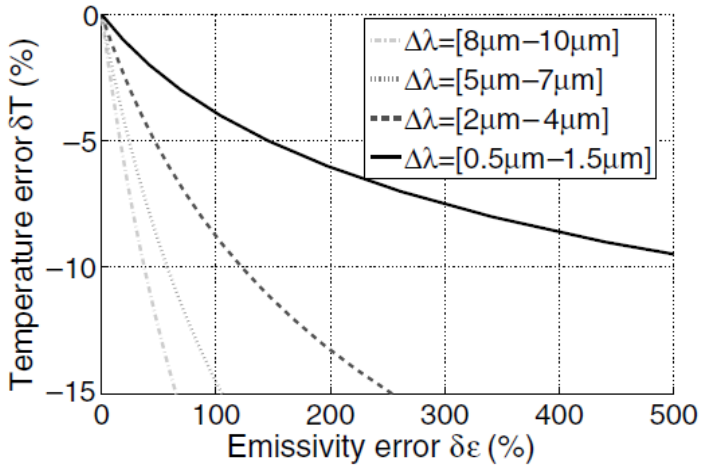

Fig. 1.16: Relative temperature error versus relative error on the emissivity at a given temperature of 550 K. [TEY 07]

Secondly, a smaller temperature assessment error can be achieved in the near-infrared spectral range rather than in the middle wave infrared spectral range even when the surface emissivity varies with the temperature. The evolution of the temperature error versus emissivity error for different spectral

ranges was shown in Fig. 1.16 when the temperature is fixed at 550 K [TEY 09]. It indicates that a better accuracy of temperature measurement could be achieved in the lower spectral range when the emissivity is varying. Rotrou et al. [ROT 06b] also studied the measurement of thermal fields of an object surface with gradient emissivity by both infrared camera operating in the spectral ranges of 8-12 μm and a silicon-based camera operating in the spectral ranges of 0.75-1.1 μm. The results showed that more accurate thermal fields can be obtained by using silicon-based cameras, while large temperature errors higher than 100 K appear by using infrared cameras due to the emissivity gradient, as shown in Fig. 1.17.

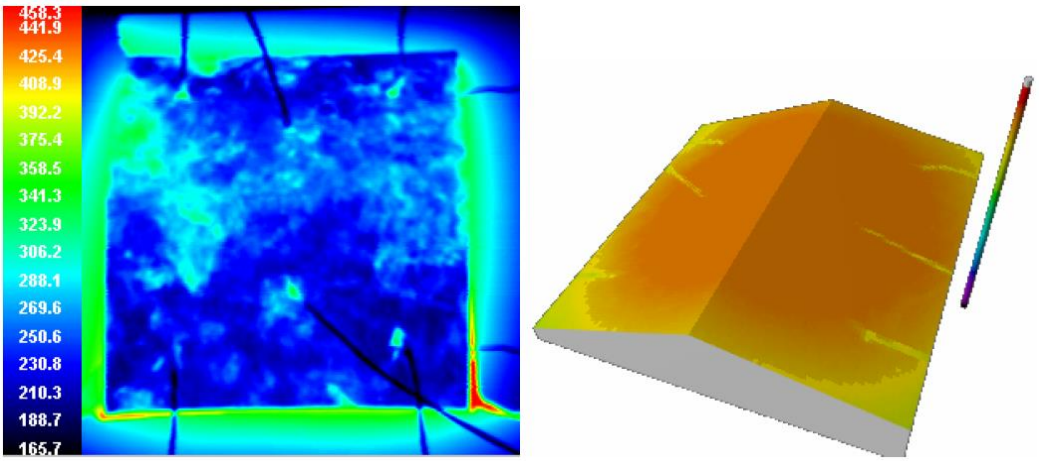

Fig. 1.17: Temperature measurement on a surface with gradients of emissivity, the infrared image on the left, the near-infrared image on the right. [ROT 06b].

Orteu et al. [ORT 08] intended to use two CCD cameras to measure the shape, strain and temperature full-fields, in which a single camera can obtain simultaneous kinematic and thermal fields. Moreover, the two cameras are used to obtain the three-dimensional shape of the object. However, the problem that the heterogeneous specimen surface coating possesses different emissivity cannot be addressed, thus the temperature they obtained is just the apparent temperature (i.e., radiation intensity) and the ture temperature field cannot be obtained directly.

Furthermore, one big practical issue for silicon-based camera operating in the near-infrared spectral range is that a small temperature variation leads to a large modification in the image gray level. At the high temperature, the temperature fluctuation easily occurs, which significantly affects the image gray level. This high sensitivity to temperature variation leads to poor quality images due to oversaturation and/or poor dynamic range of gray levels. This phenomenon will lead to unreadable images, and any useful information cannot be obtained. Moreover, in this study the kinematic field obtained by digital image correlation is based on the stable gray level images. Thus, there is here a conflict between the thermal field computation that requires to record the radiation change due to temperature, and the DIC

computation that relies on the luminance conservation, assuming only displacement and deformation of an unchanged texture.

1.4 Motivation and originality of this work

The work that is presented in this thesis aims to propose an experimental technique in order to obtain both kinematic and thermal fields at the same spatial and temporal coordinates using a single common visible camera. Three main points are addressed in this thesis:

1. How to maintain the image gray level stable when the temperature changes? This point will be addressed in Chapter 2, in which an approach to maintain the image gray level stable is proposed whatever the temperature changes.

2. In realistic applications, the thermal field should be reconstructed on the realistic specimen surface, which has its own emissivity. How to practically use a common visible camera to reconstruct thermal field on this surface without measurement of surface emissivity? This point will be addressed in Chapter 3, in which some realistic experiments are conducted and the thermal field on the specimen surface is reconstructed.

3. When both kinematic and thermal fields at the same spatial and temporal coordinates are obtained. To perform digital image correlation, a non-repetitive, contrasting texture is required on the specimen surface. Generally, the speckle is sprayed on the specimen surface. However, the speckled specimen surface will then present a non-uniform emissivity that will interfere with the thermal field computation by near-infrared thermography. How to perform the near-infrared thermography on this contrasted surface simultaneously to DIC measurement? This point will be addressed in Chapter 4, in which a method is proposed to perform near-infrared thermography on the heterogeneous surface with speckle, thereby obtaining thermal fields.

Chapter 2
Control of image gray level with temperature evolution

In this chapter, the principle of the radiometric model is introduced. Blackbody experiments are conducted to calibrate the radiometric model of the blackbody. Based on the radiometric model, an approach to automatically adjust the exposure time is proposed to obtain stable gray level images whatever temperature evolution is.

Contents

2.1 Introduction

Silicon-based sensor cameras are widely used to perform real-time observation of the kinematic fields in visible spectral range (0.4-0.75 μm). Those cameras are known to be as well sensitive in the near-infrared spectral range (0.75-1.1 μm). Thus the acquirement of thermal field using a silicon-based camera is possible and suitable for application at high temperature. Nevertheless, in the near-infrared spectral range, a small temperature variation leads to a large modification in the sensor illumination and thus of the image gray level. Orteu et al [ORT 08] gave an example: when the camera operates in the near-infrared spectral range (close to 1 μm), the ratio of the measured luminance between 573K and 1273K is about one million (times), whereas when the camera operates in the long-wave infrared spectral range (close to 10 μm) the ratio is only five (times). This high sensitivity to temperature evolution at high temperature leads to poor quality recorded images due to oversaturation and/or poor dynamic range of gray level. These undesired phenomena will lead to inexploitable images, *i.e.* that any useful information cannot be obtained. Thus, simultaneous measurement of accurate thermal and kinematic fields is quite impossible when these inexploitable images are used. In order to address this problem, this Chapter proposes an innovative method to precisely and automatically adjust the exposure time, all through the recording process, to obtain kinematically and thermally exploitable images whatever the temperature evolution on the surface of the observed object is. Indeed, a series of images with stable gray level is the basic requirement for digital image correlation whereas the recording of the sensor illumination evolution is needed for infrared thermography so as to obtain good kinematic and thermal fields at the same time.

This chapter is structured as follows. First part introduces the radiometric model, which describes the relationship between gray level, exposure time and temperature. Then, experiments are conducted by imaging a blackbody in order to calibrate the radiometric model of blackbody. In the second part, the basic principle of our approach to maintain the mean gray level of image stable is proposed, and the detailed procedure of this approach is also given. In this approach, the new exposure time should be predicted. Thus, two algorithms, including linear algorithm and Planck's algorithm, are proposed to predict the exposure time so as to obtain the images with stable mean gray level. Based on these two algorithms, a software is made to automatically adjust the exposure time to obtain images when the temperature changes. Finally, a new series of images recorded on a blackbody with varied temperature are recorded to validate and compare the accuracy and reliability of two algorithms when the temperature changes.

2.2 Radiometric model

2.2.1 Principle of radiometric model

The surface of any object has its own emissivity ($0 < \varepsilon < 1$) and own temperature ($T > 0$ K). It emits electromagnetic energy in the form of radiation in a wavelength range [λ_1, λ_2]. As mentioned in Chapter 1, the Planck's law describes the total monochromatic flux (for one particular wavelength) emitted by a blackbody as a function of its temperature and the wavelength of the electromagnetic energy. Based on the Planck's law, the total monochromatic flux emitted by the surface of any object Φ_e with uniform emissivity can be given as follows:

$$\Phi_e(\lambda,T) = \varepsilon(\lambda)\cdot M(\lambda,T) = \varepsilon(\lambda)\cdot\frac{c_1}{\lambda^5}\left(e^{\frac{c_2}{\lambda T}}-1\right)^{-1} \tag{2.1}$$

where $\varepsilon(\lambda)$ is the emissivity of the object surface, for the considered wavelength. In reality, the measurement of a flux emitted by a target surface is difficult to be achieved because the reflection of flux from surrounding objects received by this surface Φ_{ref} is often superimposed on it. The total flux received by a detector Φ_{tot} is therefore given as follow:

$$\Phi_{tot}(\lambda,T) = \Phi_e(\lambda,T) + \Phi_{ref}(\lambda,T) = \varepsilon(\lambda)\cdot M(\lambda,T) + (1-\varepsilon(\lambda))\Phi_{ref}(\lambda,T) \tag{2.2}$$

The quantum sensors of the detectors use the photoelectric effect to create electrons from the received photons if their energy is sufficient (greater than the gap energy of the material constituting the detector). The electron flow is measured during the exposure time for each of the pixels. It is finally converted to the form of digital level *I*. The detectors made by different materials are sensitive to different wavelength ranges. For example, the silicon based detector is particularly sensible in the wavelength range from 0.4 μm to 1.1 μm, while the VisGaAs based detector can detect the wavelength range from 0.4 μm to 1.7 μm. In this thesis, the silicon-based camera is used due to its low cost, lack of cooling, low sensitivity to the emissivity of the material and its spatial resolution.

The description of the whole measurement chain makes it possible to establish the general radiometric equations. Cabannes et al. [CAB 96] indicated that it is generally necessary to simplify these equations to be able to use them. The expression of the digital gray level *I*, representing the illumination, can be reduced to the following two terms:

$$I = \tau\cdot\left(\int\varepsilon(\lambda)\cdot W(\lambda)\cdot M(\lambda,T)\cdot d\lambda + \int(1-\varepsilon(\lambda))\cdot W(\lambda)\cdot\Phi_{ref}(\lambda,T)\cdot d\lambda\right) \tag{2.3}$$

where τ is the exposure time (integration time) of the camera; $W(\lambda)$ is the spectral response of the whole measurement system. Different systems have different components. Generally, the spectral

response of the whole measurement system involves the spectral transmittance of the atmosphere φ_{atm}, the spectral transmittance of the filter φ_{filter} (if there is), the spectral quantum efficiency η_e, and so on. $M(\lambda,T)$ is the spectral radiance of blackbody (as indicated in Chapter 1, Eq. (1.17)).

If the measurement is carried out in a dark room without other energy sources, or if the surface emissivity $\varepsilon(\lambda)$ is sufficiently high, the term containing Φ_{ref} can be neglected. Thus, the Eq. (2.3) can be simplified as follows:

$$I = \tau \cdot \int \varepsilon(\lambda) \cdot W(\lambda) \cdot M(\lambda,T) \cdot d\lambda = \tau \cdot \int \varepsilon(\lambda) \cdot W(\lambda) \cdot \frac{C_1}{\lambda^5} \left(e^{\frac{c_2}{\lambda T}} - 1 \right)^{-1} \cdot d\lambda \qquad (2.4)$$

In this study, a CMOS camera sensitive to wavelength up of 1.1 μm is used. The maximum temperature to be studied is about 1203 K. Wien's approximation indicates that: if $\lambda \cdot T \le 2900 \mu m \cdot K$, it can be simplified as $e^{\frac{c_2}{\lambda T}} - 1 \approx e^{\frac{c_2}{\lambda T}}$. Thus, this study satisfies the condition of Wien's approximation ($1.1 \mu m \times 1203 K \le 2900 \mu m \cdot K$), and the Eq. (2.4) can be simplified as follows:

$$I = \tau \cdot \int \varepsilon(\lambda) \cdot W(\lambda) \cdot \frac{C_1}{\lambda^5} \cdot e^{-\frac{c_2}{\lambda T}} \cdot d\lambda \qquad (2.5)$$

The Eq. (2.5) is an integral form, which wavelength bounds are difficult to use in practical measurement. Rotrou et al. [ROT 06] introduced an effective wavelength λ_e into the radiometric model. Thus, the digital signal *I* can be given as follows:

$$I = \tau \cdot \left(c_1 \cdot K_{\text{int}} \cdot W(\lambda_e) \cdot \varepsilon(\lambda_e) \cdot \lambda_e^{-5} \right) \cdot e^{-\frac{c_2}{\lambda_e T}} \qquad (2.6)$$

where K_{int} is an integration constant. Based on the Saunders's research [SAU 97]. The spectral density of energy in the near-infrared spectral band will move to lower wavelengths when the temperature increases. Thus, the effective wavelength λ_e to be considered, should be chosen as a function of the absolute temperature of the surface. That is why an extended effective wavelength $\lambda_x(T)$ is introduced by Rotrou [ROT 06] into the term $e^{-\frac{c_2}{\lambda_e T}}$. Then, the final equation can be given as follows:

$$I = \tau \cdot k_w \cdot e^{-\frac{c_2}{\lambda_x(T) T}} \qquad (2.7)$$

where k_w, gathering several set-up dependent parameters, is a parameter which could be determined by a radiometric calibration process, *T* is the absolute temperature, c_2 is the second Planck's constant (1.44×10^{-2} m·K), $\lambda_x(T)$ is the extended effective wavelength, which is defined by the following equation [ORT 08]:

$$\frac{1}{\lambda_x(T)} = a_0 + \frac{a_1}{T} + \frac{a_2}{T^2} + \cdots + \frac{a_n}{T^n}, (n = \infty) \qquad (2.8)$$

where a_0, a_1, a_2, a_3, ⋯, a_n are parameters dependent of the whole bench configuration (camera's sensor, lens, surrounding objects, etc.), which should be determined by a *priori* in situ radiometric calibration. Due to the short temperature range (less than 300 K) to be studied in this study, the extended effective wavelength with two parameters a_0 and a_1 is enough for the radiometric model calibration. Thus, the radiometric model equation can be written as follows:

$$I = \tau \cdot k_w \cdot e^{-\frac{c_2 \times a_0}{T} - \frac{c_2 \times a_1}{T^2}} \tag{2.9}$$

To avoid performing too many radiometric model calibrations for each exposure time, the intensity $I_n(T)$ is used to perform the calibration [ROT 06], which is defined as gray level I normalized by exposure time τ. Thus, the radiometric model equation can be written as follows:

$$I_n = \frac{I}{\tau} = k_w \cdot e^{-\frac{c_2 \times a_0}{T} - \frac{c_2 \times a_1}{T^2}} \tag{2.10}$$

The Eq. (2.10) is the radiometric model, which provides the desired relation between the temperature of the studied surface T and the numerical level I. Three unknown parameters of the radiometric model (k_w, a_0 and a_1) should be calibrated in order to calculate the temperature distribution over the object surface.

2.2.2 Blackbody experimental set-up

Blackbody experiments are conducted to calibrate the radiometric model. The schematic diagram of the experimental bench is shown in Fig. 2.1. It is composed of four main elements: (a) a cavity blackbody (temperature reference source up to 1350 K) and its temperature controller (RCN 1200 N1 manufactured by HGH); (b) a CMOS camera (VC-12MC-M65E0-FM) with 4096 × 3072 pixels, mounted with a lens (NIK AF MICRO-NIKKOR 200MM F/4D IF-ED); (c) an auxiliary pyrometer to monitor the effective blackbody internal temperature; (d) a computer which controls the image acquisition and records the experimental data (images, blackbody theoretical temperature prescribed by the controller, blackbody internal temperature controlled by embedded thermocouple and by pyrometer, recording exposure time).

The experiments are performed in a dark room to avoid the interference from other heat sources. The CMOS camera is placed with its optical axis normal to the Ø 50 mm aperture of the cavity blackbody. The distance between the front lens of the camera and the blackbody is approximately 1 meter. The computer records simultaneously: the digital image with gray level encoded between 0 and 255 level, exposure time of the camera. The CMOS camera is controlled by home-made Labview software, which can automatically adjust the exposure time of the camera to control the mean image gray level of a particular region of the image (see ROI in Fig. 2.2) during the heating process of the blackbody.

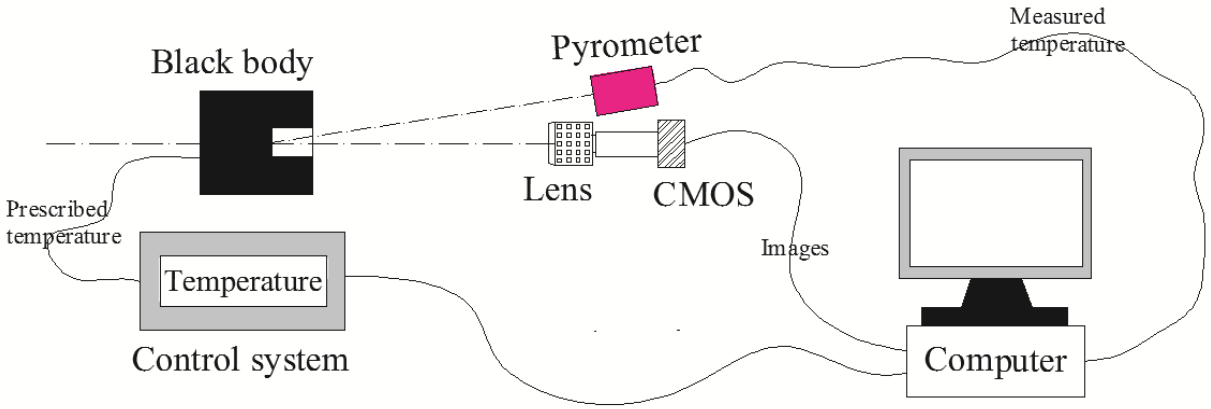

Fig. 2.1: Blackbody experimental set-up.

2.2.3 Calibration of radiometric model

The aforementioned radiometric model describes the relation between gray level, exposure time and temperature. Validating the relation between these three physical quantities is an important issue for better understanding of the radiometric model. Moreover, three parameters (k_w, a_0 and a_1) must be identified.

Fig. 2.2 shows an acquired image of the blackbody. The red region in the image is the region of interest (ROI), which has 1000 × 1000 pixels. A series of images have been recorded with various independently and manually tuned blackbody temperature or and/or exposure time. The exposure time varied between [1; 11ms] for two particular temperatures of 1123K and 1153K and the temperature of the blackbody varied between [1050; 1250K] for two given exposure times of 7 ms and 3 ms. Fig. 2.3 shows the evolution of mean gray level of ROI as a function of exposure time at fixed temperature. It is clear that the gray level increases with the increase of exposure time. We also find that these data follow the linear curves. The evolution of gray level as a function of the temperature for fixed exposure time of 3 ms and 7 ms is shown in Fig. 2.4. The mean gray level also increases with increasing of temperature. But the experimental data roughly follows the exponential curves. These results indicate that the form of the radiometric model in Eq. (2.10) is accurate, in which exposure time and gray level are in linear relation, and the gray level and temperature are in exponential relation.

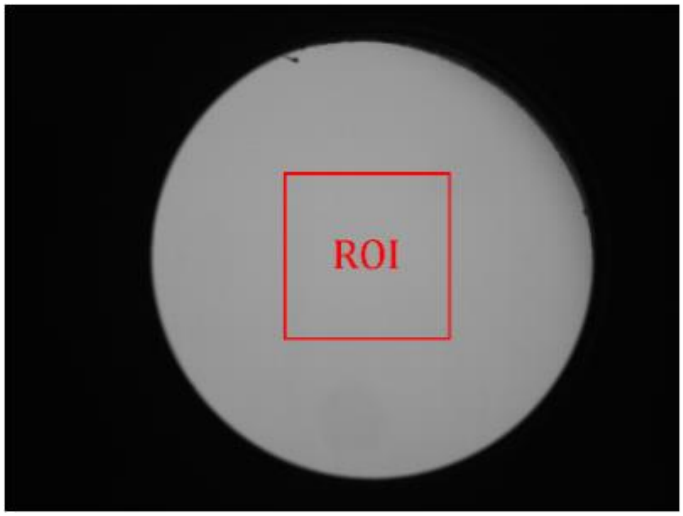

Fig. 2.2: Image acquired and the ROI with 1000 × 1000 pixels.

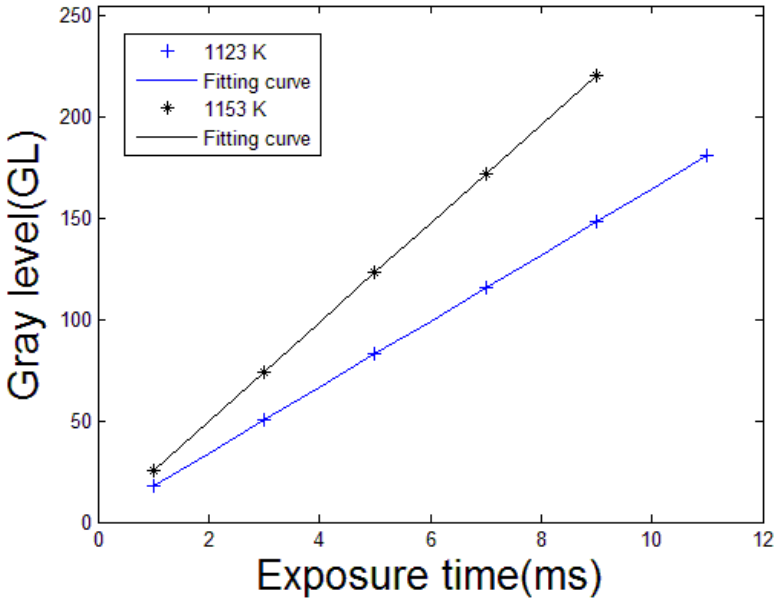

Fig. 2.3: Evolution of mean gray level of ROI as a function of exposure time for the given temperatures of 1223 K and 1253 K.

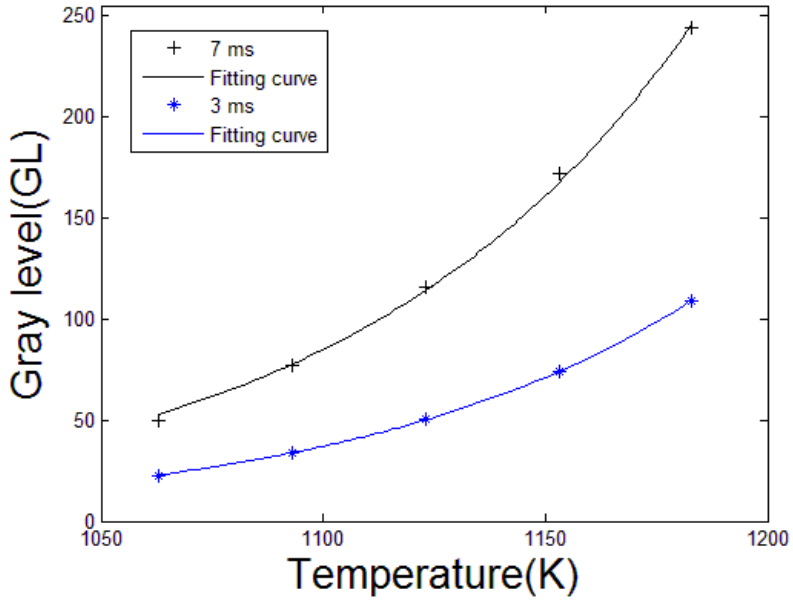

Fig. 2.4: Evolution of mean gray level of ROI as a function of temperature for the given exposures time of 7 ms and 3 ms.

Blackbody experiments (13 images acquired with manual adjustment of blackbody temperature and exposure time) are also conducted to calibrate the radiometric model. In this study, the least square method is used to calibrate the radiometric model. Through the calibration process by Matlab software, the three parameters of the radiometric model (k_w, a_0 and a_1) are identified and indicated in Table 2.1. Thus, for our particular set-up, the radiometric model of blackbody can be given as follows:

$$I_n = \frac{I}{\tau} = 1.358\times10^{11} \times \exp\left(-\frac{1.843\times10^4}{T} + \frac{8.549\times10^5}{T^2}\right) \tag{2.11}$$

The calibrated radiometric model of blackbody is also shown in Fig. 2.5, where experimental data (cross points) follows well the calibrated radiometric model (continuous curve).

Table 2.1: Three parameters of radiometric model of the blackbody.

k_w (GL/s)	a_0 (m^{-1})	a_1 ($K \cdot m^{-1}$)
1.358×10^{11}	1.28×10^6	-5.9368×10^7

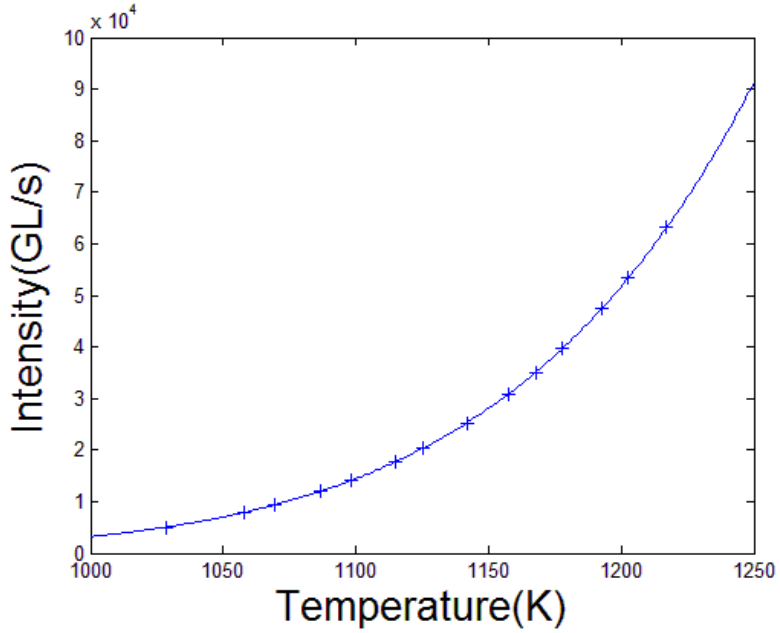

Fig. 2.5: Radiometric calibration function identified on experimental data (cross points).

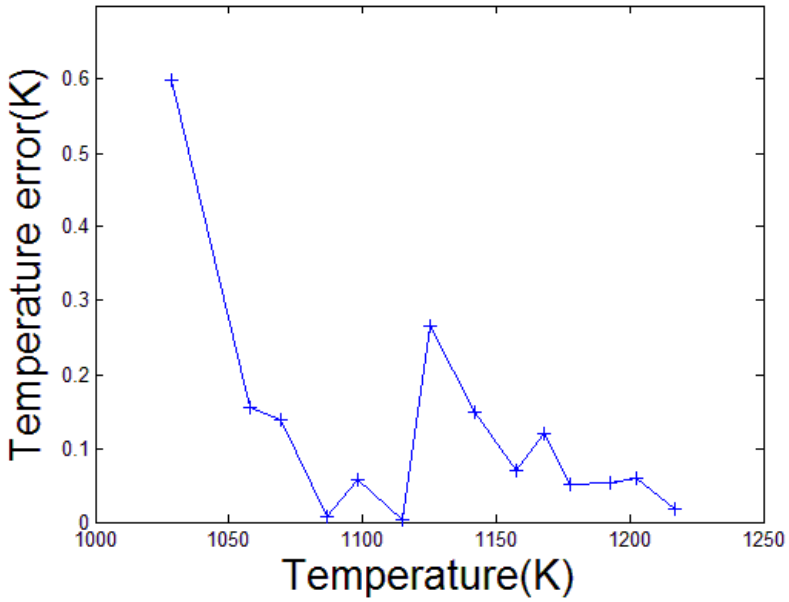

Fig. 2.6: Temperature errors of radiometric model.

In order to validate the identified radiometric model, we propose to evaluate the error between temperature calculated thanks to the radiometric model and the temperature measured by the pyrometer. The temperature errors of the radiometric model ΔT_{radio} is defined by:

$$\Delta T_{radio} = \left| T_{real} - T_{radio} \right| \tag{2.12}$$

where T_{real} is the blackbody temperature measured by the pyrometer; T_{radio} is the calculated temperature by radiometric model. Fig. 2.6 shows the temperature errors of radiometric model. The maximum error is only 0.6 K. Most of errors are less than 0.3 K.

2.3 Approach to control image illumination

2.3.1 Principle of the approach

The camera receives the incident flux coming from the target object which is related to its surface temperature. Each pixel then converts the incident flux into the output signal (gray level value), so the gray level value of the acquired image is directly linked to the temperature of the object surface. Moreover, the exposure time controls the duration of acquisition and thus to the amount of photons collected by the sensor. Thus, the gray level of an image can be modified by adjusting the exposure time of camera. The principle of the proposed approach is to continuously and automatically adjust the exposure time to get a series of images with stable mean gray level of the ROI whatever the temperature evolution is. The schematic diagram of the basic principle is shown in Fig. 2.7. At the beginning, the first two images (as indicated by black points) are acquired with an identical exposure time (i.e., $\tau_1 = \tau_2 = \tau$). If the exposure time is kept unchanged while the temperature increases, the image gray level will increase fast (as indicated by hollow points) and this will easily lead to the saturation of image. Thus, the exposure time should be adjusted (decreased in this case) to maintain mean gray level of ROI equal to that of the first image (as indicated by red points).

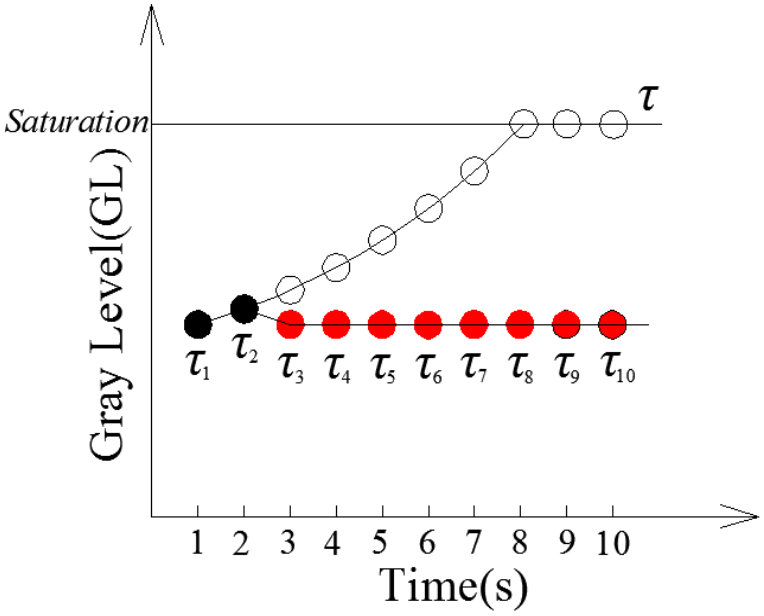

Fig. 2.7: Schematic diagram of the basic principle of the approach.

2.3.2 Detailed procedure of the exposure time adjustment

It is observed from the radiometric model (Eq. 2.10) that the intensity is only related to temperature. If the first two images are known and one gives a prediction of the temperature of the next image, then the intensity of the third one can be predicted. The flow chart for maintaining the mean gray level of ROI is shown in Fig. 2.8. A criterion equation is introduced as follows:

$$\left|\overline{I_n(i-1)} - \overline{I_n(1)}\right| \le C, i \ge 3 \tag{2.13}$$

where $\overline{I_n(i-1)}$ is the mean intensity value of ROI in the No. $i-1$ image, $\overline{I_n(1)}$ is the mean intensity value of ROI in the first image, and C is a critical value chosen by the user. This critical threshold, as low as possible, cannot be exactly zero as it is impossible to acquire two exactly identical images in reality (noise, vibrations, optical disturbance, etc.).

When the discrepancy in mean intensity value between the image $i-1$ and the first one is less than the critical value C, it means that the intensity as well as the temperature is the same between two images. Thus, it is unnecessary to change the exposure time and the next exposure time $\tau(i)$ can be equal to the last one $\tau(i\text{-}1)$. When the discrepancy is greater than the critical value C, it means that the intensity as well as the temperature is different between two images. The exposure time should be adjusted to make the gray level equal to the original one. In this situation, an algorithm to accurately predict the next exposure time should be proposed. This study proposes two kinds of algorithms (Linear algorithm and Planck's algorithm) in the following section 2.3.3 to predict the next exposure time $\tau(i)$.

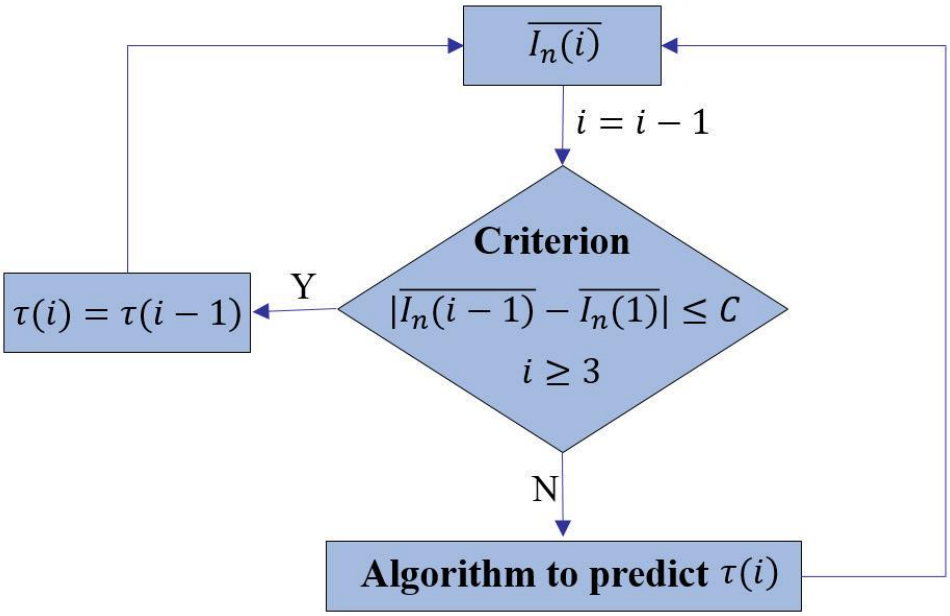

Fig. 2.8: Flow chart of the approach to maintain the image gray level constant.

2.3.3 Two possible algorithms to predict the exposure time

Linear algorithm

A linear algorithm can be used to predict the next exposure time. The principle of the specific law of linear algorithm is shown in Fig. 2.9. Because the frequency of camera is maintained constant during the tests, the time interval between adjacent images is constant. Thus, an equation can be given as follow:

$$t_i - t_{i-1} = t_{i-1} - t_{i-2} \tag{2.14}$$

For a general linear function $\overline{I_n} = a \times t + b$, there are

$$\overline{I_n(i)} = a \times t_i + b \tag{2.15}$$

$$\overline{I_n(i-1)} = a \times t_{i-1} + b \tag{2.16}$$

$$\overline{I_n(i-2)} = a \times t_{i-2} + b \tag{2.17}$$

Combining Eqs. (2.14), (2.15), (2.16) with (2.17), it can obtain:

$$\overline{I_n(i)} - \overline{I_n(i-1)} = a \times (t_i - t_{i-1}) + b = a \times (t_{i-1} - t_{i-2}) + b = \overline{I_n(i-1)} - \overline{I_n(i-2)} \tag{2.18}$$

Thus,

$$\overline{I_n(i)} = 2 \times \overline{I_n(i-1)} - \overline{I_n(i-2)} \tag{2.19}$$

Eq. (2.19) can be expanded:

$$\overline{I_n(i)} = \frac{\overline{I(i)}}{\tau(i)} = 2 \times \frac{\overline{I(i-1)}}{\tau(i-1)} - \frac{\overline{I(i-2)}}{\tau(i-2)} \tag{2.20}$$

In order to make sure that mean gray level value of image number *i* is equal to that of the first image $\overline{I(i)} = \overline{I(1)}$, the next exposure time can be predicted as follows:

$$\tau(i) = \frac{\overline{I(1)}}{2 \times \frac{\overline{I(i-1)}}{\tau(i-1)} - \frac{\overline{I(i-2)}}{\tau(i-2)}} \tag{2.21}$$

Planck's algorithm

The radiometric model is derived from the Planck's law, and its basic equation is an exponential function. Thus, the exponential algorithm based on Planck's law seems relevant to predict the next exposure time. The principle of the specific law of exponential algorithm is shown in Fig. 2.9. Because the frequency of camera is maintained constant during the tests, the time interval between adjacent images is constant (indicated by Eq. (2.14)). For a general exponential function $\overline{I_n} = a \cdot e^{bt}$, there are

$$\overline{I_n(i)} = a \cdot e^{bt_i} \tag{2.22}$$

$$\overline{I_n(i-1)} = a \cdot e^{bt_{i-1}} \tag{2.23}$$

$$\overline{I_n(i-2)} = a \cdot e^{bt_{i-2}} \tag{2.24}$$

Combining Eqs. (2.14), (2.22), (2.23) with (2.24), it can obtain:

$$\overline{I_n(i)} \times \overline{I_n(i-2)} = a \cdot e^{bt_i} \times a \cdot e^{bt_{i-2}} = a^2 \cdot e^{b(t_i + t_{i-2})} = a^2 \cdot e^{2b(t_{i-1})} = \overline{I_n(i-1)}^2 \tag{2.25}$$

Thus,

$$\overline{I_n(i)} = \frac{\overline{I_n(i-1)}^2}{\overline{I_n(i-2)}} \tag{2.26}$$

Eq. (2.26) can be expanded:

$$I_n(i) = \frac{\overline{I(i)}}{\tau(i)} = \left[\frac{\overline{I(i-1)}}{\tau(i-1)}\right]^2 \times \frac{\tau(i-2)}{\overline{I(i-2)}} \tag{2.27}$$

In order to make sure that mean gray level value of image number *i* is equal to that of the first image $\overline{I(i)} = \overline{I(1)}$, the next exposure time can be predicted as follows:

$$\tau(i) = \overline{I(1)} \times \left[\frac{\tau(i-1)}{\overline{I(i-1)}}\right]^2 \times \frac{\overline{I(i-2)}}{\tau(i-2)} \tag{2.28}$$

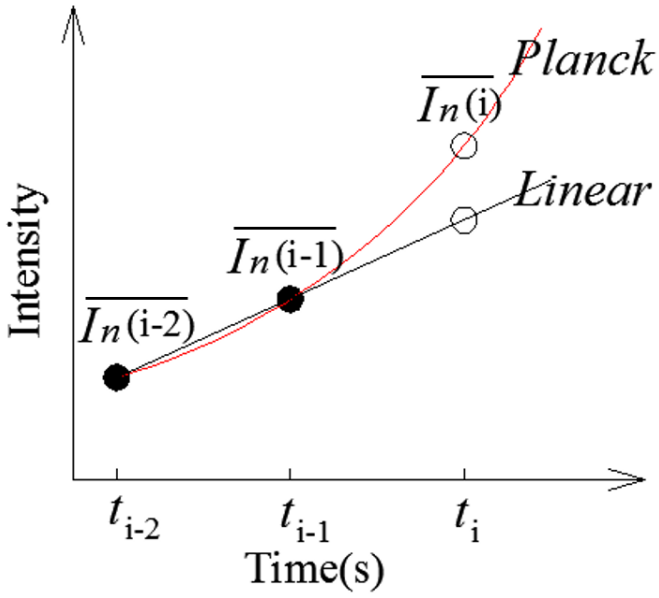

Fig 2.9: Principle of the specific law of exponential function and linear function.

2.3.4 Validation of two algorithms

Blackbody experiments are conducted in the temperature range from 1024K to 1224K. Eighteen images are acquired with automatic adjustment of exposure time by a homemade software based on the aforementioned two algorithms. The parameters of the two cases are shown in Table 2.2. In order to validate and compare two algorithms of exposure time prediction, a set of simulated gray levels, which are inferred from the radiometric model, are firstly analyzed. Then a set of realistic images of the blackbody experiments at different temperatures is also analyzed. We aim at quantify how much both algorithms are able to keep mean gray level stable whatever the temperature changes.

Table 2.2: The parameters of two cases to validate and compare two algorithms.

Case No.	Critical value C (GL/s)	Frequency of camera (Hz)	Algorithm
Case 1 Case 2	0.05	0.05	Linear Planck

Case 1

Based on the radiometric model and the linear algorithm to predict the next exposure time, the simulation process is conducted by Matlab software. Fig. 2.10 shows the simulated results of a case by using linear algorithm and the temperature range is from 1024 K to 1224 K. As mentioned in section 2.3.1, the first two images are taken with a constant exposure time (about 35.1 ms). Thus, Fig. 2.10(b) shows that the

image gray level rapidly increases with the temperature change between the two first images. Then, the linear algorithm operates and automatically adjusts the exposure time of the camera. One can observe that the exposure time decreases when the temperature increases, and the corresponding gray level decreases. It is worth noting that the first exposure time prediction and adjustment is underestimated leading to a mean gray level a little bit higher than expected. Then, the gray level has a decreasing trend.

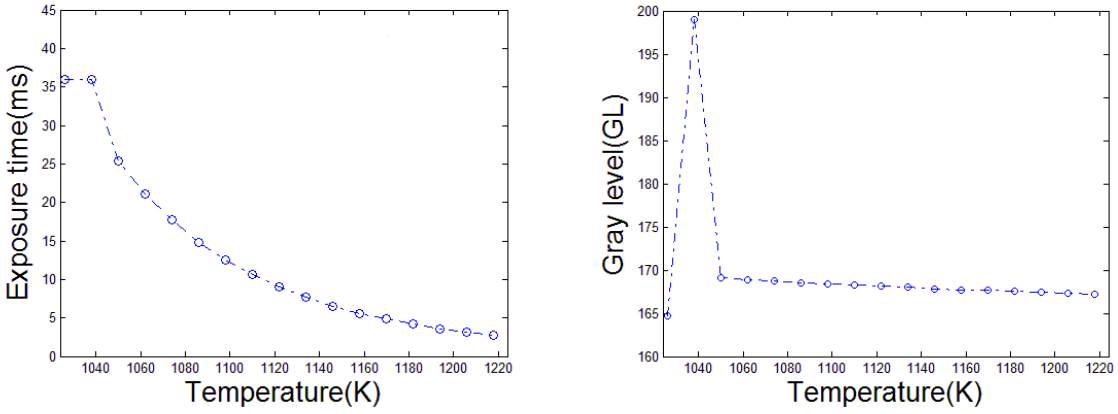

(a) Automatic adjustment of exposure time. (b) Evolution of mean gray level after exposure time adjustment.

Fig. 2.10: Simulated results of linear algorithm.

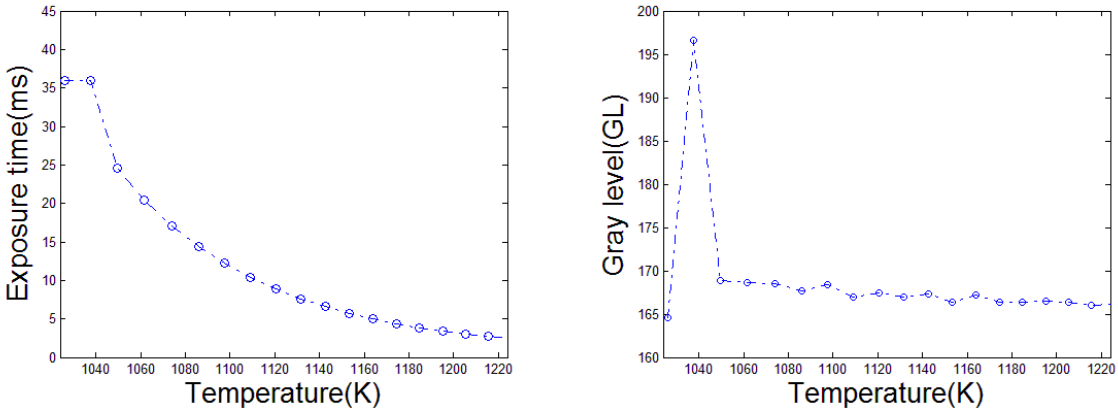

(a) Automatic adjustment of exposure time. (b) Evolution of mean gray level after exposure time adjustment.

Fig. 2.11: Experimental results of linear algorithm.

Blackbody experiments with the same conditions as the simulation process are conducted, and the corresponding results are shown in Fig. 2.11. Comparing the experimental results with the simulated ones, one can observe that the evolution of exposure time and gray level in the experiments is almost the same as that of simulated results, but the difference is that the gray level after adjustment in the

experiments is not a perfectly linear reduction relationship. This phenomenon is normal because the heating rate of blackbody in reality is not an exactly linear and the experiments will be affected by noise, vibrations and optical disturbance, while in the simulation the heating rate follows a perfect linear function.

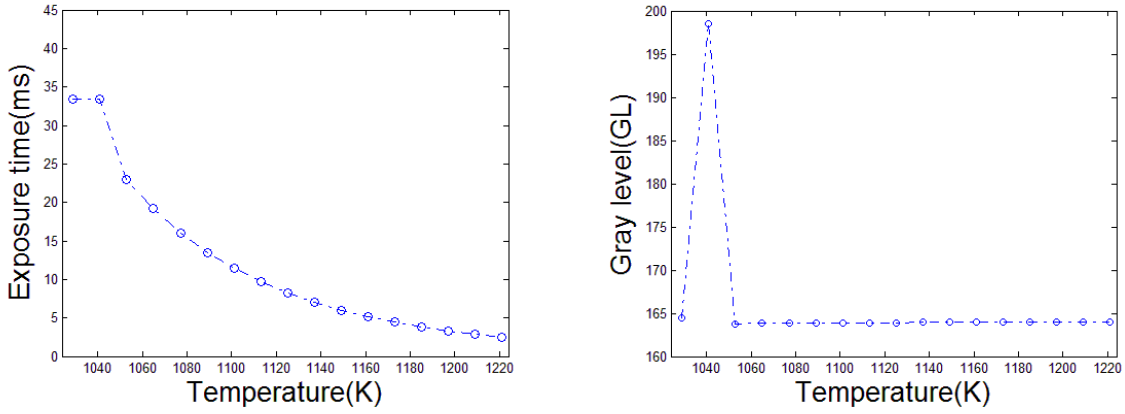

(a) Automatic adjustment of exposure time. (b) Evolution of mean gray level after exposure time adjustment.

Fig. 2.12: Simulated results of Planck's algorithm.

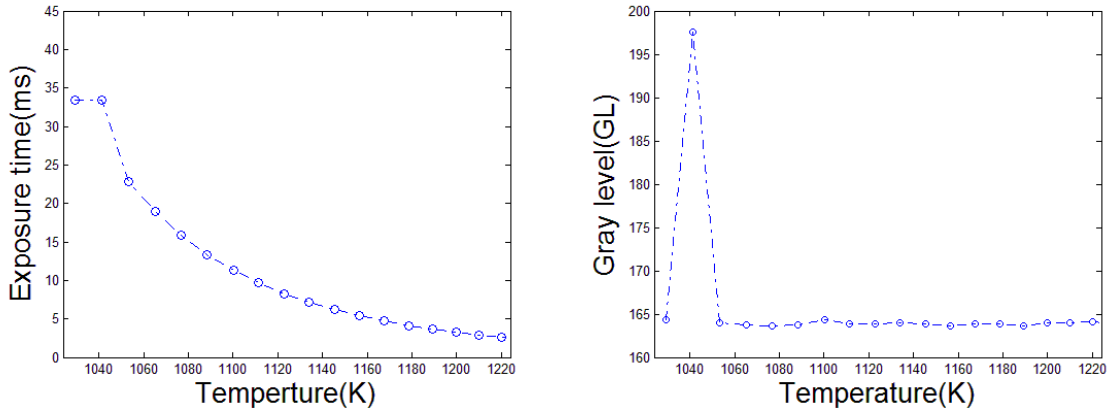

(a) Automatic adjustment of exposure time. (b) Evolution of mean gray level after exposure time adjustment.

Fig. 2.13: Experimental results of Planck's algorithm.

Case 2

The Planck's algorithm is also used to maintain the gray level constant as the temperature increases in the simulation process. Fig. 2.12 shows the results of the use of Planck's algorithm on the set of simulated mean gray levels. As for the linear algorithm, the exposure time is constant for the first two images, giving a 2nd gray level quite different from the expected one. The mean gray level then decreases to be equal to that of the first image due to the rapid decrease of the exposure time. It can be seen that a stable gray level after adjustment is obtained.

Based on the Planck's algorithm, the corresponding experimental results at the same conditions are shown in Fig. 2.13. It is apparent that the experimental results agree well with the simulated one, and the image gray level after adjustment decreases to the original value of the first image.

Comparison between two algorithms

The error, which is defined as the difference between mean gray level of image after the third one $\overline{I(i)}$ and the mean gray level of the first image $\overline{I(1)}$ normalized by the mean gray level of the first image, is introduced as follows:

$$error = \frac{\left|\overline{I(i)} - \overline{I(1)}\right|}{\overline{I(1)}} \times 100\% \tag{2.29}$$

Both experimental errors of linear algorithm and Planck's algorithm are shown in Fig. 2.14. It is apparent that the Planck's algorithm has two advantages: first the error is less than 0.5% which is much smaller than the linear algorithm; then the error is stable. It seems thus that this error is mainly due to experimental artifacts (noise, temperature regulation or non-uniformity). The Planck's algorithm is based on the basic function of the radiometric model, thus it is better for it to predict precisely the next exposure time, thereby resulting in the more accurate image gray level equal to the original value of the first image after adjustment. It is also worth noting that although the software made by Planck's algorithm is derived from the radiometric model, in the practical application of this software it is unnecessary to conduct the calibration experiment and calibrate the radiometric model.

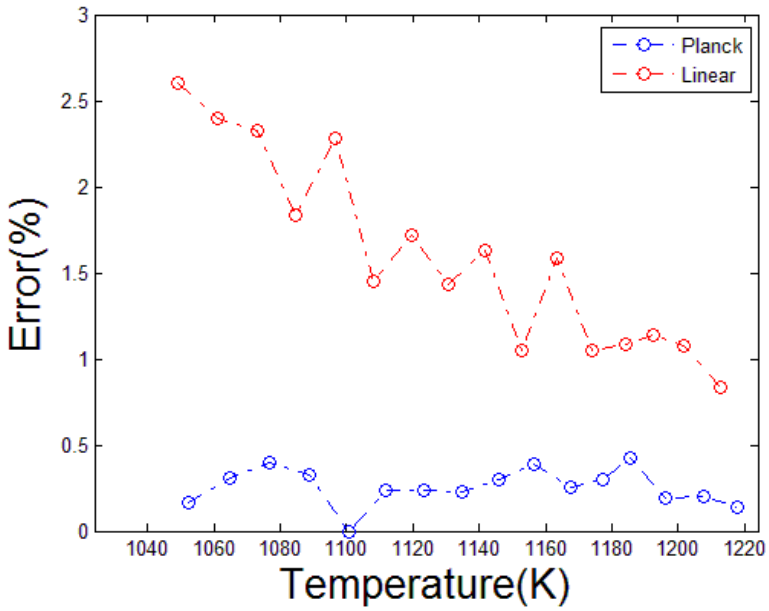

Fig. 2.14: Experimental errors of linear algorithm and Planck's algorithm.

2.4 Conclusions

The radiometric model and an approach to control mean gray level of ROI in the images whatever the temperature evolution are investigated in this chapter. In the first part, the basic principle of radiometric model is introduced, and image recording and analyses of a high temperature blackbody are conducted to calibrate the radiometric model. The least square method is used to identify the three parameters k_w, a_0 and a_1 of radiometric model. Thus, the radiometric model of blackbody with three parameters is obtained as follows:

$$I_n = \frac{I}{\tau} = 1.358 \times 10^{11} \times \exp\left(-\frac{1.843 \times 10^4}{T} + \frac{8.549 \times 10^5}{T^2} \right)$$

Meanwhile, the errors of radiometric model at different temperatures are also calculated, and the maximum error is only 0.6 K.

In the second part of this chapter, an approach to automatically adjust exposure time is proposed to obtain a series of images with stable mean gray level whatever the temperature changes. The basic principle and detailed procedure of this approach is described. Two algorithms, linear algorithm and Planck's algorithm, are proposed to predict the exposure time. Based on two algorithms, a homemade software is made to automatically adjust the exposure time. Then the homemade software is applied to compute the temperature of images recorded during the heating of blackbody from 1024 K to 1224 K. This procedure aims to validate and to compare the accuracy and reliability of two algorithms. The results indicate that a reliable and stable mean image gray level can be obtained by Planck's algorithm, while bigger errors will occur by using the linear algorithm. Thus, the Planck's algorithm is more suitable to obtain images with stable and reliable gray level.

Chapter 3
Thermal field reconstruction in realistic application

This chapter contains two parts. The first part introduces the basic principle of thermal field reconstruction based on radiometric model. The thermal field of blackbody experiment is reconstructed. In the second part, the thermal field of specimen surface in realistic application is reconstructed without surface emissivity measurement.

Contents

3.1 Introduction

As pointed out in Chapter 2, a simple radiometric model can be calibrated over a few images at different temperatures. The demonstration of this identification has been performed on a blackbody cavity. Moreover, a homemade software based on the Planck's algorithm has been proposed in order to acquire images with stable mean gray level by automatically adjusting the exposure time. It has been obtained and validated by recording the heating process of blackbody. In the first part of this chapter, the principle of thermal field reconstruction is proposed, and the thermal fields of blackbody images are reconstructed based on this principle. Then, the temperature errors between temperatures calculated from the thermal fields and temperatures measured by thermocouples are also calculated.

To further validate the accuracy of the software for automatic adjustment of exposure time and the method to reconstruct thermal field, two different realistic applications are conducted in the second part of this chapter. In the first experiments, two heating coils are used for heating a steel specimen. In the second experiments, a heating plate is used for heating a titanium alloy specimen. For both experiments, the evolution of the mean gray level of ROI is investigated to further validate the accuracy and reliability of the software based on the Planck's algorithm for automatic adjustment of exposure time. Thereafter, thermal fields of images acquired in both experiments are reconstructed, and the temperature errors between temperatures calculated from the thermal fields and temperatures measured by classic measurement methods (pyrometer or thermocouples) are also calculated.

3.2 Thermal field reconstruction

3.2.1 Principle of thermal field reconstruction

In this study, the radiometric model, which describes the relationship between gray level, exposure time and temperature (firstly introduced by Eq. (2.10) in Chapter 2) is recalled hereafter:

$$\ln\left(I_n\right) = \ln\left(k_w\right) - \frac{c_2 \times a_0}{T} - \frac{c_2 \times a_1}{T^2} \tag{3.1}$$

Thus,

$$\frac{c_2 \times a_1}{T^2} + \frac{c_2 \times a_0}{T} + \ln\left(I_n\right) - \ln\left(k_w\right) = 0 \tag{3.2}$$

The temperature can finally be expressed by the following equation:

$$T = \frac{1}{-\sqrt{\frac{a_0^{\,2}}{4a_1^{\,2}} - \frac{\ln(I_n) - \ln(k_w)}{c_2 \times a_1}} - \frac{a_0}{2a_1}} \tag{3.3}$$

If the radiometric model is calibrated and all three parameters (k_w, a_0 and a_1) are obtained. The temperature can be computed from the intensity, which is the gray level divided by exposure time.

During the experimental procedure, the images and exposure time of the camera are recorded. Thus, the temperature of each pixel in an image can be calculated from the Eq. (3.3), and the thermal field can also be reconstructed based on the calculated temperatures of all pixels. This is the basic principle of thermal field reconstruction

3.2.2 Thermal fields of blackbody

In Chapter 2, the radiometric model of blackbody has been obtained. Based on the radiometric model of blackbody and recorded images of blackbody, the thermal field can be computed pixelwise, under uniformity assumption that the same global radiometric model can be used for all pixels. Several thermal fields of ROI (as indicated in Fig. 2.2) for various temperatures measured by pyrometer are shown in Fig. 3.1 when using the software Planck's algorithm for automatic adjustment of exposure time. Meanwhile, the temperature error ΔT_{pixel} between each pixel and pyrometer can also be calculated, which is defined as follows:

$$\Delta T_{pixel} = \left| T_{real} - T_{pixel} \right| \tag{3.4}$$

where T_{pixel} is the calculated temperature of each pixel, T_{real} is the temperature measured by the pyrometer. The error field can thus be reconstructed based on the errors of all pixels, as shown in Fig. 3.1. The mean temperature errors and standard deviations (error bars) of all error fields at various temperatures measured by pyrometer are plotted in Fig. 3.2. It is apparent from these two figures that the thermal field and error field are quite uniform. Mean temperature errors of all error fields are about 1 K. It demonstrates that the calculated temperatures are in good agreement with the measured temperatures, and the near-infrared thermography technique used for calculating temperature is accurate and reliable.

Temperature (K)	**Thermal field (K)**	**Error field (K)**
1064.7	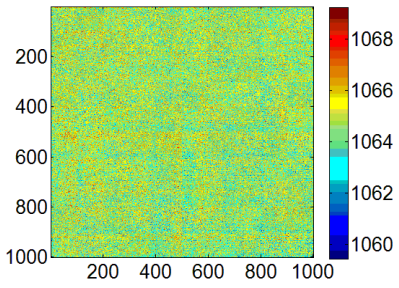	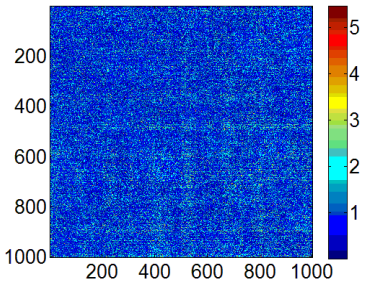

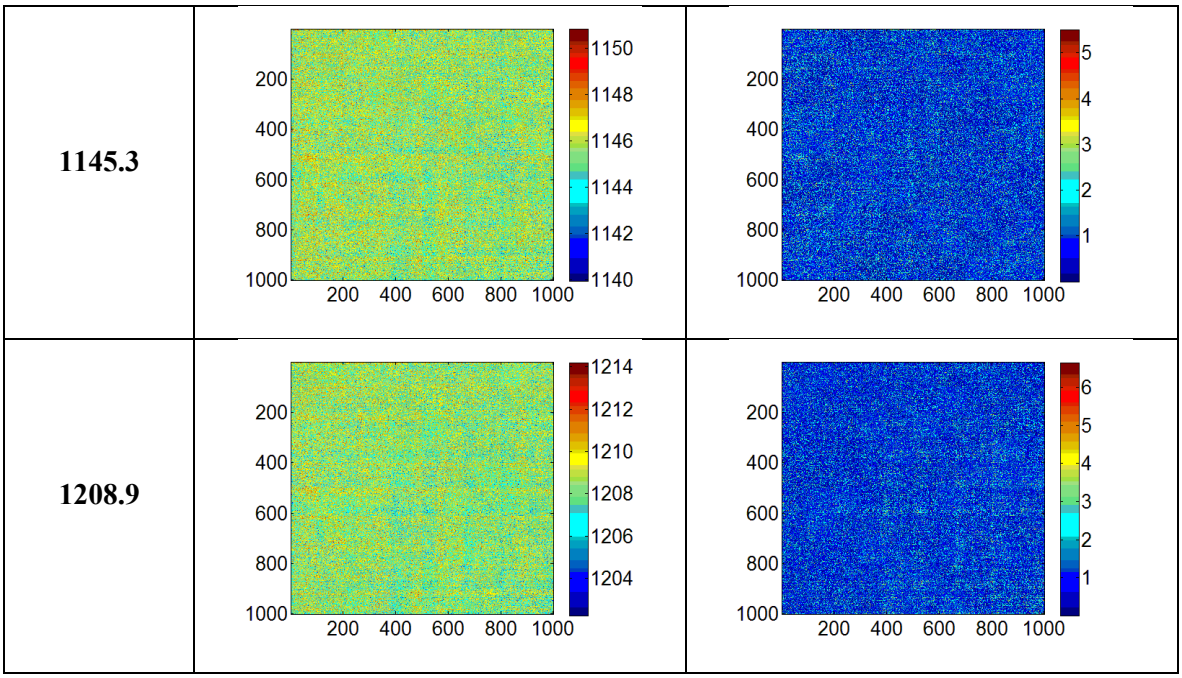

Fig. 3.1 Reconstructed thermals field and error fields from recorded images with mean gray level conservation (Planck's algorithm).

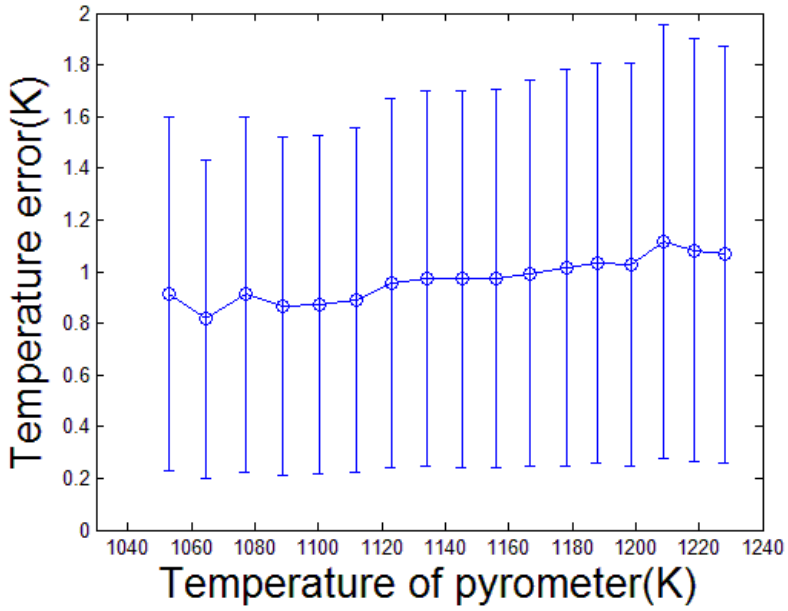

Fig. 3.2: The mean temperature errors and standard deviations (error bars) of error fields at various temperatures of pyrometer

3.3 Thermal field reconstruction in realistic applications

The aforementioned software based on the Planck's algorithm for automatic adjustment of exposure time and the method for reconstructing thermal field has been exploited so far only in blackbody experiments. In this section, the software is used in realistic experiments, and the corresponding thermal field is reconstructed. Two different tests are conducted: first heating process of a steel specimen under heating coils is investigated, then the heating process of a titanium alloy specimen under heating plate is investigated.

3.3.1 Thermal field of specimen surface under heating coils

Experimental Procedure

The material used is AISI 304L steel, which chemical composition (wt.-%) is Fe−0.024C−1.09Mn−18.55Cr−8.00Ni−0.41Si−0.008S−0.023P. A specimen with dimensions of 100 mm (length) × 10 mm (width) × 1 mm (thickness) was cut from the steel sheets. For metal specimen where emissivity is too low or heterogeneous, coating with black paint is required in common infrared thermography in order that the homogeneous and high emissivity surface can be produced. Thus, the specimen surface was sprayed with high temperature black paint.

Fig. 3.3 shows the experimental set-up. This set-up consists of several main elements: (a) AISI 304L steel specimen with black paint coating; (b) an induction heating device; (c) a CMOS camera (VC-12MC-M65E0-FM) with 4096 × 3072 pixels, mounted with a lens (NIK AF MICRO-NIKKOR 200MM F/4D IF-ED); (d) a pyrometer and three thermocouples to provide the classical temperature measurement for comparison; (e) a computer with our software to record the experimental data (images, exposure time and temperature) and automatically adjust the exposure time to control the image gray level.

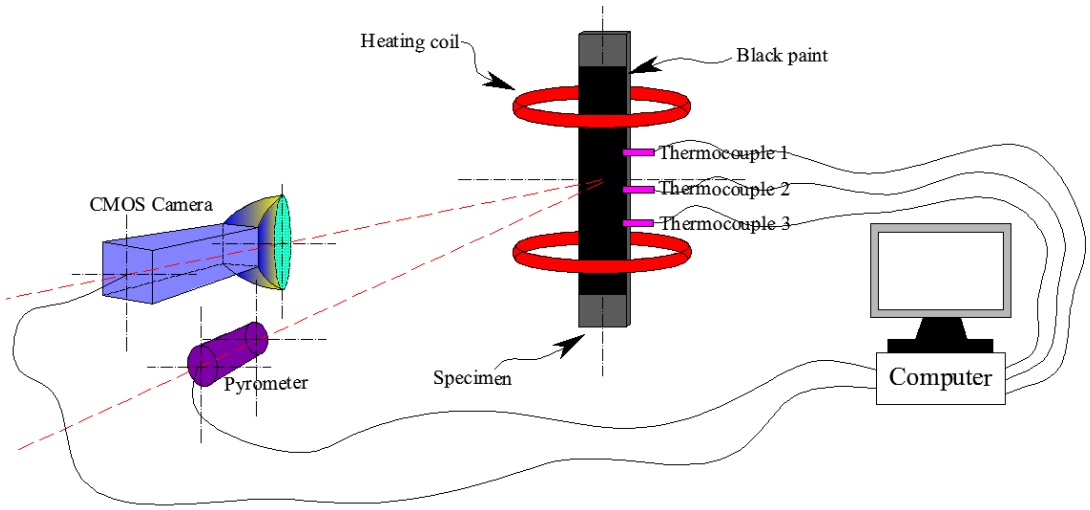

Fig. 3.3 Experimental set-up: the observed surface is located between the two induction heating coils.

The experiment was conducted in a small dark room. The distance between the front lens of the camera and the specimen surface was approximately 1 meter. Three thermocouples were welded at the edge of the specimen surface, and the distance between optical pyrometer and the specimen surface was 1 meter. The specimen was heated by induction with two coils, and its temperature is servo-controlled with respect to the data returned to a control thermocouple. The induced temperature is ordered from 873 K to 973 K and the heating rate is set to 1K/s. The software based on the Planck's algorithm is used for automatic adjustment of exposure time, and images are acquired with acquisition rate of 1 image per second at the same time. Before the test, the pyrometer is calibrated to ensure the control thermocouple and the pyrometer indicate the same value when the same temperature is measured.

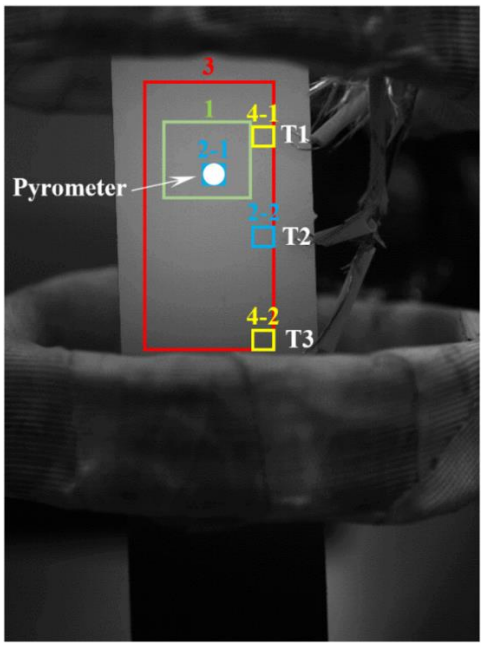

Fig. 3.4: Acquired image of specimen surface under induction heating: Rectangle 1 is the ROI for exposure time adjustment; rectangles 2-1 and 2-2 are considered for the identification of the radiometric model; rectangle 3 is the area of thermal field reconstruction; rectangles 4-1 and 4-2 are considered for the validation of the reconstructed thermal field.

Fig. 3.4 shows an acquired image of the specimen surface. The white dot in the center of the image is the measuring position of pyrometer. T1, T2 and T3 are the three thermocouples. The green rectangle 1 is a chosen ROI with 500 × 400 pixels, analyzed by our homemade software, where the mean gray level is intended to be maintained stable or even constant by automatic adjustment of exposure time. The two blue squares 2-1 and 2-2 are two 100 × 100 pixels areas, chosen to identify the parameters of the radiometric model in this configuration. These two particular areas are chosen because they correspond to the measurement points of the pyrometer and to the location of the thermocouple T2. A justification of the size of the area 2-2 is proposed in Appendix A. The red rectangle 3 with 800 × 1700

pixels is a wide ROI for the thermal field reconstruction. The yellow 100 × 100 pixels squares 4-1 and 4-2 are chosen because they correspond to the temperature measurement areas of thermocouple 1 (T1) and thermocouple 3 (T3). The temperatures of these two yellow squares calculated from thermal fields are respectively compared with the measured temperatures by thermocouples T1 and T3, thereby validating the accuracy of the thermal field.

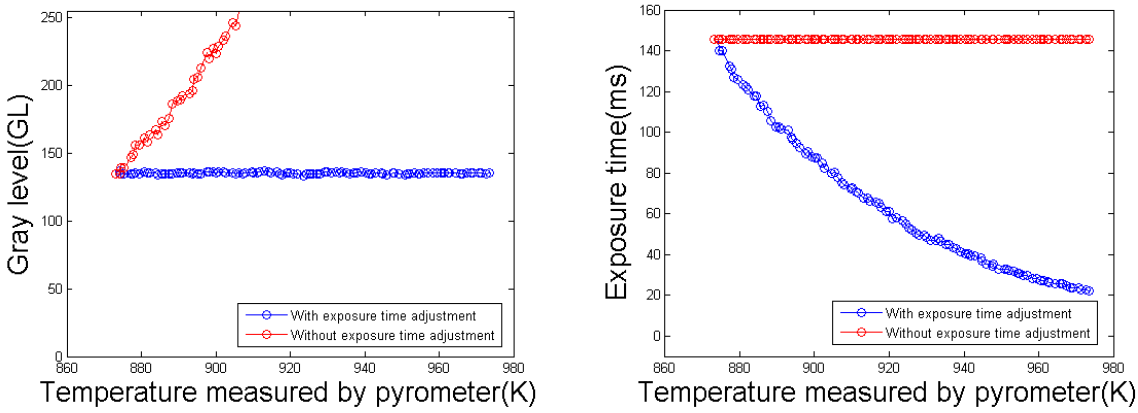

(a) Mean gray level of ROI 1 evolution.

(b) Exposure time evolution after exposure time adjustment.

Fig. 3.5: Mean gray level of ROI 1 and exposure time evolves as the temperature measured by pyrometer increases with/without exposure time adjustment.

Control of the conservation of the image mean gray level

Fig. 3.5 shows the evolution of mean gray level of green ROI 1 (defined in Fig. 3.4) and exposure time with/without exposure time adjustment as the temperature measured by pyrometer increases from 873 K to 973 K. As indicated by red points in Fig. 3.5(a), without the automatic adjustment of exposure time the mean gray level of green ROI 1 increases fast from original gray level 135 GL to the maximum gray level 255 GL as the temperature just increases from 873 K to 906 K. As the temperature further increases from 906 K to 973 K, the acquired images are inexploitable due to the over saturation of images. These saturated images cannot provide any useful information. Some examples of acquired images are shown in Fig. 3.6, in which the gray level of image increases with the increase of temperature at the constant exposure time. When the mean gray level of ROI 1 is chosen to be controlled by the software based on the Planck's algorithm for automatic adjustment of exposure time, the exposure time decreased with the increase of temperature (shown in Fig. 3.5(b)), in which the critical value C is set to 0.05 GL/s and the frequency of camera is set to 1 Hz. It can also be found that with automatic adjustment of exposure time the corresponding mean gray level of ROI 1 (as indicated by blue points in Fig. 3.5(a)) can be maintained stable as the temperature increases from 873 K to 973 K. Some examples of acquired images are also shown in Fig. 3.7, in which the gray level of image is maintained stable with the increase of temperature

when the exposure time is automatically adjusted. This result further indicates that the software based on the Planck's algorithm for automatic adjustment of exposure time is feasible and reliable.

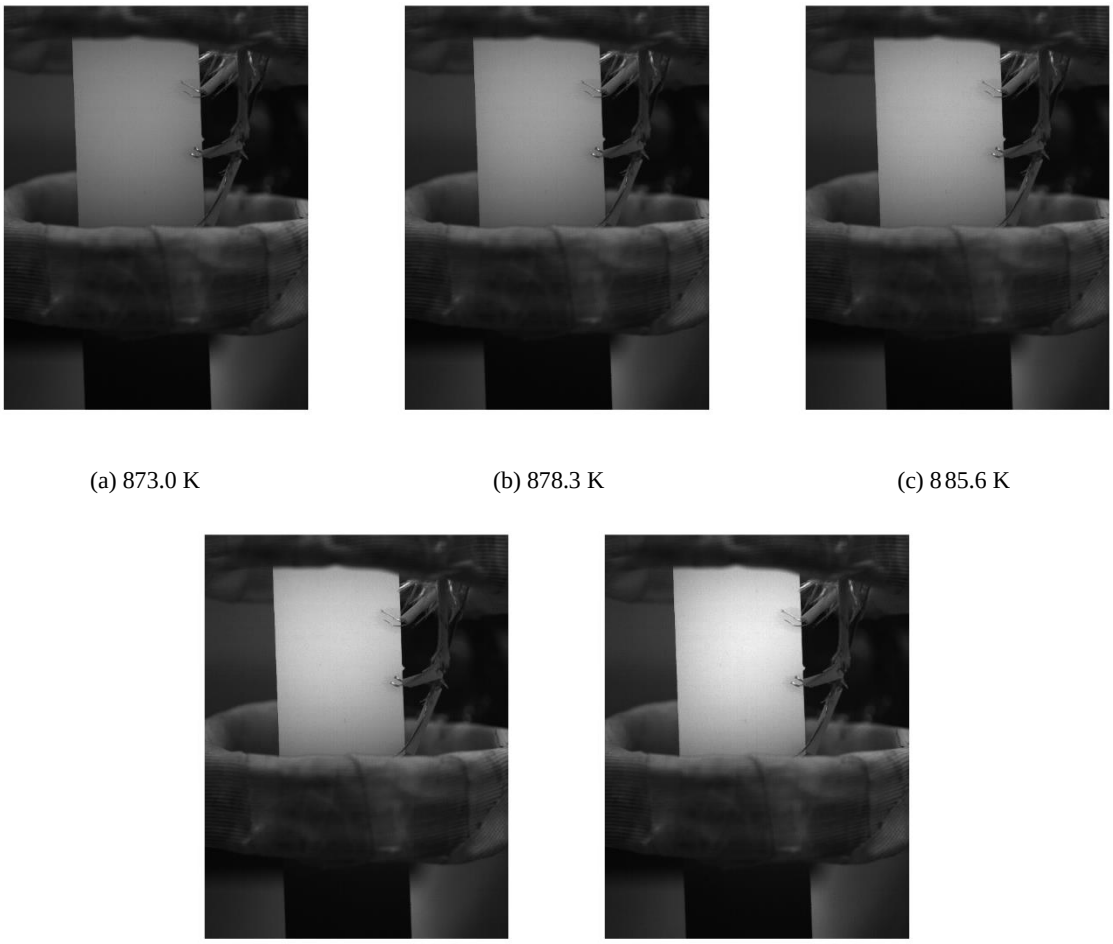

(a) 873.0 K (b) 878.3 K (c) 885.6 K

(d) 894.0 K (e) 900.6 K

Fig. 3.6: Some images acquired at various temperatures using a constant exposure time.

(a) 873.0 K (b) 878.3 K (c) 885.6 K

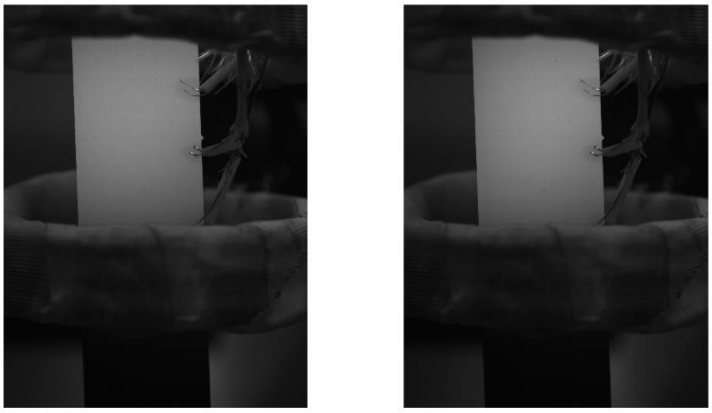

(d) 894.0 K (e) 900.6 K

Fig. 3.7: Some images acquired at various temperatures with exposure time adjustment.

Calibration of radiometric model

Three parameters k_w, a_0 and a_1 of radiometric model should be obtained by calibration of radiometric model. The mean gray level of two blue ROI (Fig. 3.4) and reference temperatures provided by pyrometer and thermocouple T2 are used for the radiometric model calibration. All data of two ROIs are used to calibrate the radiometric model. Experiment data and calibrated radiometric model are shown in Fig. 3.8. It can be seen that two sets of experimental data obtained by pyrometer and T2 are in good agreement. Based on all these experimental data, the radiometric model (red curve) is calibrated using the least square method, and the three parameters of radiometric model are obtained and indicated in Table 3.1. Thus, the radiometric model of steel specimen surface can be given as follows:

$$I_n = \frac{I}{\tau} = 2.12\times10^{11}\times\exp\left(-\frac{1.728\times10^4}{T}+\frac{4.349\times10^5}{T^2}\right) \tag{3.5}$$

A temperature is defined as the difference between the inferred temperature of the surface thanks to the calibrated radiometric model and the specimen temperature measured by the pyrometer and the thermocouple T2. Fig. 3.9 shows the temperature errors as a function of the specimen temperature. The maximum error is about 2.5 K. Most of errors are less than 1.5 K.

Table 3.1: Three parameters of radiometric model of steel specimen surface.

k_w (GL/s)	a_0 (m^{-1})	a_1 ($K\cdot m^{-1}$)
2.12×10^{11}	1.20×10^{6}	-3.02×10^{7}

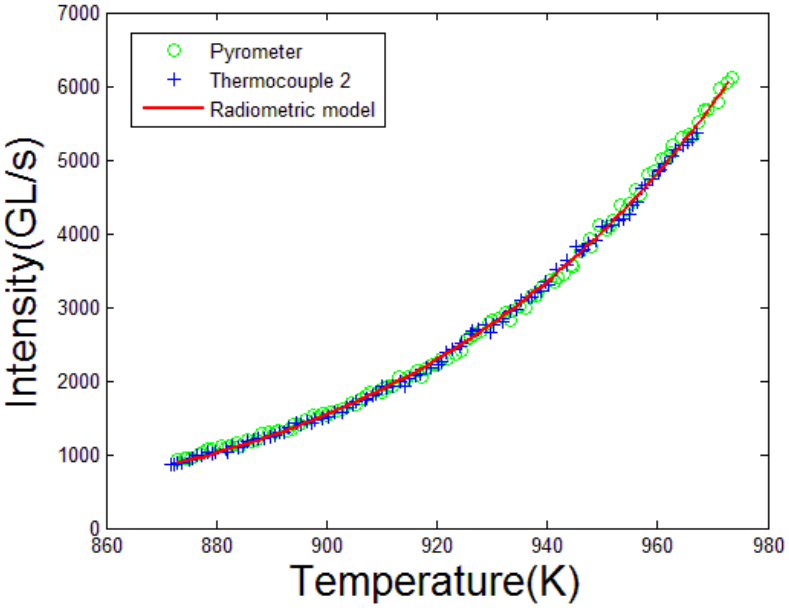

Fig. 3.8: Identification of the radiometric model parameters: rounds and crosses represents the mean gray level of areas 2-1 and 2-2 respectively as a function of the measured temperature by the pyrometer and thermocouple T2 respectively.

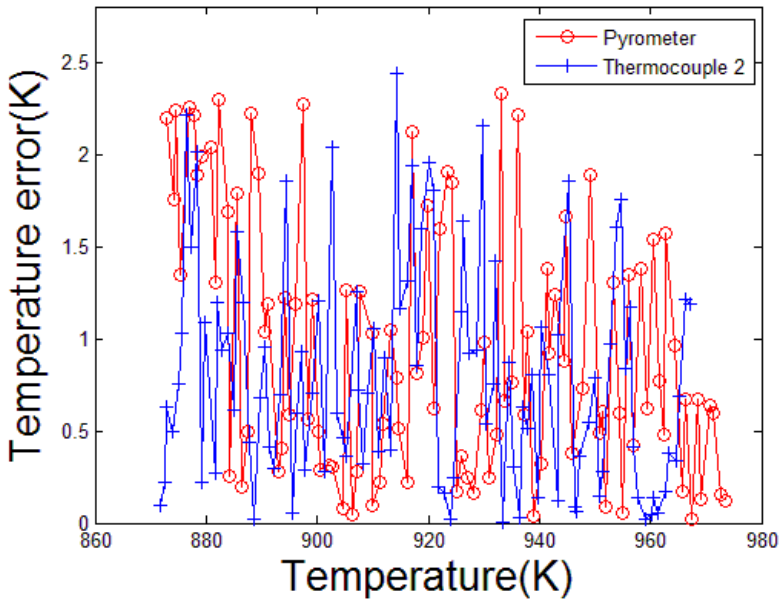

Fig. 3.9: Temperature errors of the radiometric model.

In this realistic test, the homemade software to obtain stable gray level images is validated to be effective and reliable. Using the intensity, the radiometric model on a realistic surface can be calibrated successfully. For the radiometric model calibration, trustable measurement of the real temperature of the specimen surface achieved by pyrometer and thermocouple is required, and the record images acquired all although the heating process of specimen are also required. If these experimental data can be obtained successfully, the temperature fields can be reconstructed over a large area of the observed object.

Thermal field reconstruction

The thermal field can be reconstructed thanks to the aforementioned radiometric model of steel specimen surface. In the following, thermal field of the red ROI 3 (indicated in Fig. 3.4) is intended to be reconstructed. Some examples of reconstructed thermal fields at various temperatures measured by thermocouple T1 are shown in Fig 3.10. As expected, the thermal fields over the specimen surface are non-homogeneous: a gradient of almost 30℃ is visible from edges to the mid-height of the field. This is likely due to the spacing of the coils required to observe the specimen surface, and the induced magnetic field is therefore less homogeneous as well as the temperature induced in the steel specimen. The temperature distribution along the black dotted line (as indicated in Fig. 3.10(a)) is also analyzed: the horizontal ordinate of the line is No. 400 pixel. The temperature distribution, calculated thanks to the radiometric model, along the line at different temperatures of T1 is shown in Fig. 3.11. The graph shows that the temperature gradients on the specimen surface at different temperatures of T1 are almost stable, indicating that the induction heating coils can provide a stable temperature distribution for this steel specimen surface at different temperatures. Moreover, two thermocouples (T1 and T3) are used to validate the accuracy and reliability of thermal fields. The mean temperatures of two yellow rectangles 4-1 and 4-2 (Fig. 3.4) are calculated from the thermal fields to be compared with the temperatures measured by these two thermocouples (T1 and T3). Fig. 3.12 shows the temperature errors between the measured temperatures and calculated temperatures. The result indicates that the calculated temperatures are in good agreement with the measured temperatures. The maximum temperature error is about 2.5 K. Most of the temperature errors between calculated and measured temperatures are less than 1.5 K. This indicates that the reconstructed thermal fields are accurate and reliable.

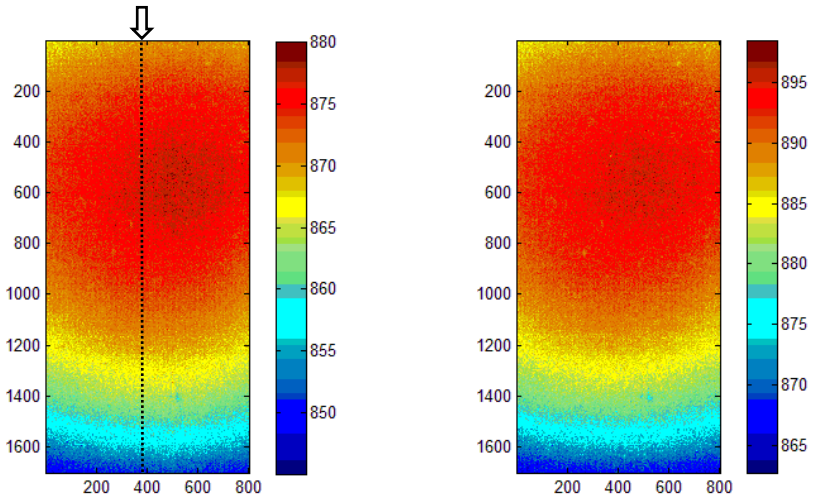

(a) 875.6 K

(b) 893.3 K

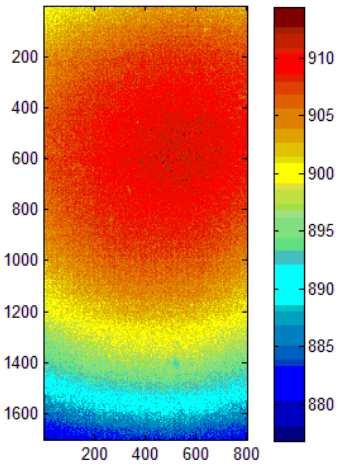

(c) 908.2 K

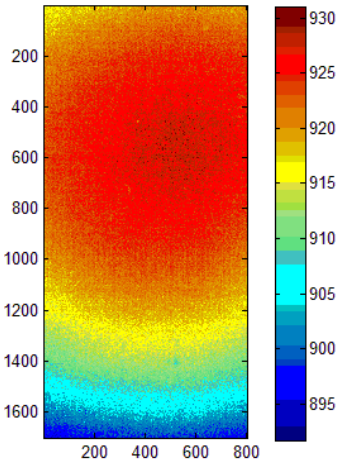

(d) 924.5

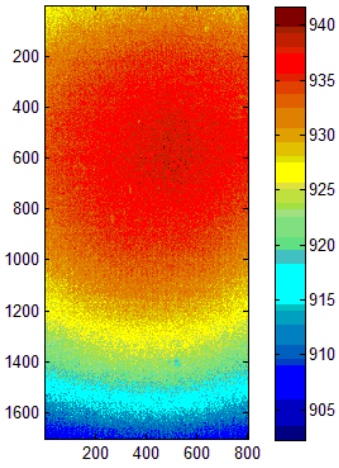

(e) 936.3

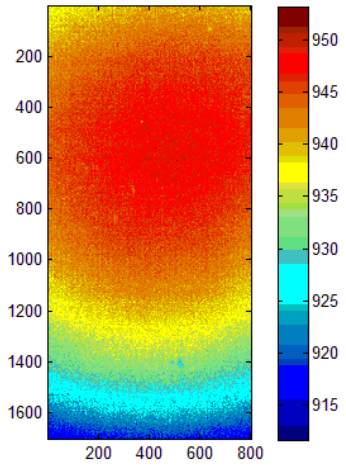

(f) 946.2

Fig. 3.10: Reconstructed thermal fields at different measured temperatures of T1.

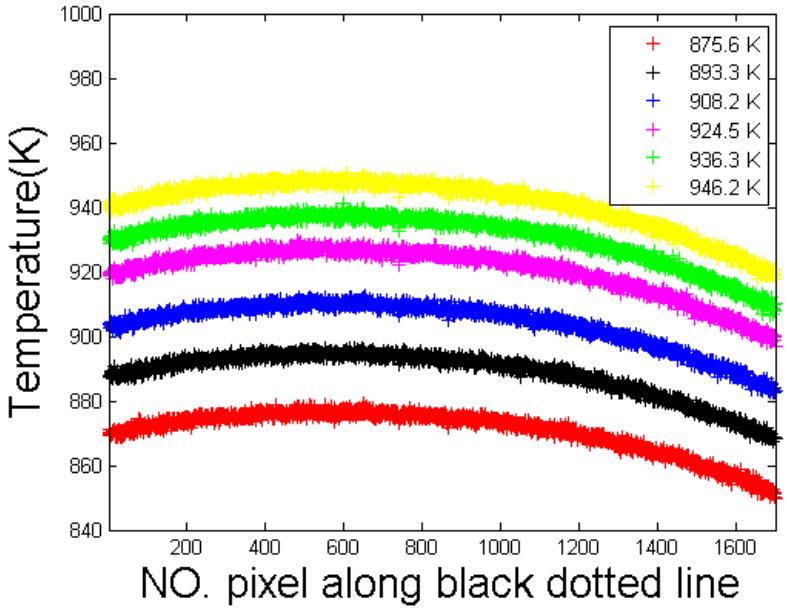

Fig. 3.11: Temperature distribution along the longitudinal direction (see the black dotted line in **Figure 3.10**(a)) for different temperatures commands given to the induction heating device.

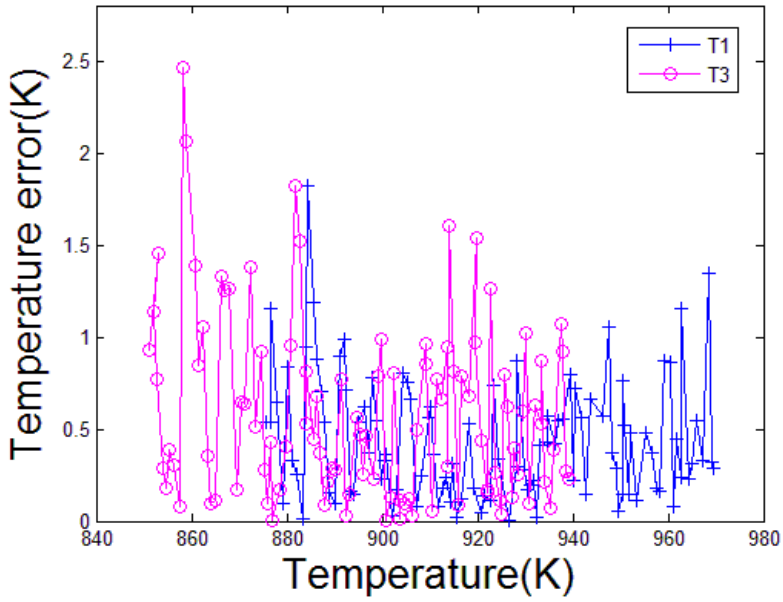

Fig. 3.12: Temperature error between the calculated temperatures and measured temperatures by thermocouple 1 (T1) and thermocouple 3 (T3).

3.3.2 Thermal field reconstruction under heating plate

Experimental Procedure

The material used is Ti-6Al-4V titanium alloy, which chemical composition (wt.-%) is Ti−6.05Al−4.32V−0.22Fe−0.04Si−0.024C−0.006N−0.16O-0.003H. A specimen with dimensions of 100 mm (length) × 10 mm (width) × 1 mm (thickness) was cut from the sheets. The specimen surface was also coated with black paint in order to make the emissivity uniform and maximal.

Fig. 3.13 shows the experimental set-up. This set-up consists of several main elements: (a) a Ti-6Al-4V alloy specimen with black paint coating on the surface; (b) an induction heating plate; (c) the CMOS camera; (d) two thermocouples; and (d) a computer with the software to record data and automatically adjust exposure time.

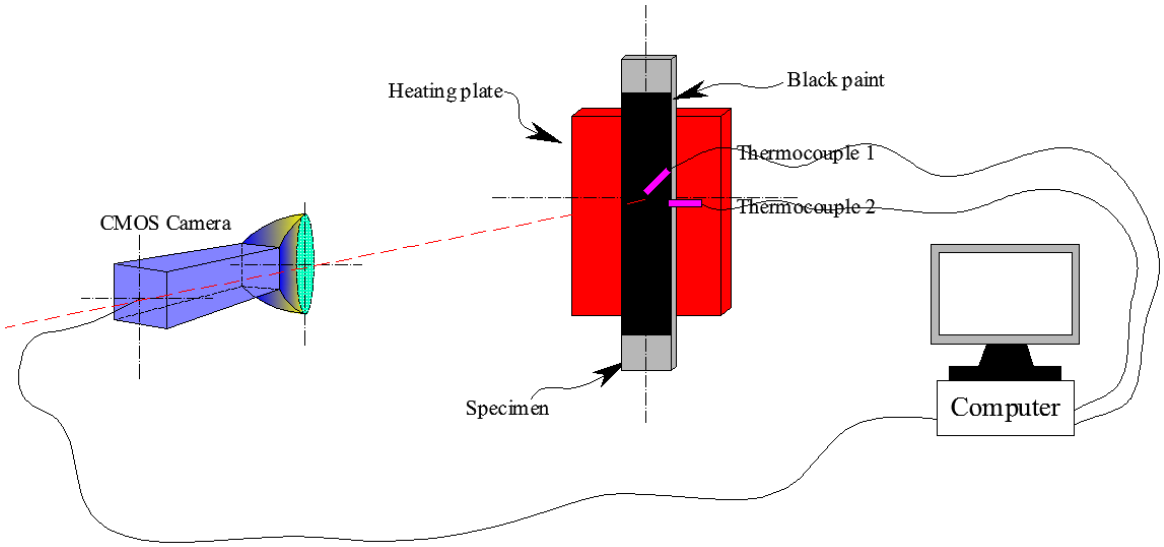

Fig. 3.13: Experimental set-up under heating plate.

The experiment was conducted in a small dark room to prevent interference from the eventual surrounding radiation. The distance between the front lens of the camera and the specimen surface was around 1 meter. A thermocouple (T2) was welded at the edge of the specimen surface, while another one was welded in the center of the specimen surface. The temperature of the specimen, induced by the magnetic field generated by the heating plate, is from 873 K to 1023 K and the heating rate is set to 5 K/s. The distance between heating plate and specimen is approximately 10 mm. The software based on the Planck's algorithm is used for automatic adjustment of exposure time. The images are acquired at the same time.

Fig. 3.14 shows an acquired image of specimen surface. The green rectangle 1 is a ROI with 200 × 200 pixels, chosen for the exposure time adjustment, where the mean gray level is intended to be

maintained stable or even constant. T1 and T2 are two thermocouples. A blue ROI 2 with 100 × 10 pixel is chosen for the radiometric model calibration, in which the mean gray level is assumed to be correspond to the temperature measured by thermocouple 2 (T2). The Appendix B gives a justification for the choice of this area. Red rectangle 3 with 2500 × 1000 pixels is the considered ROI for thermal field reconstruction. The mean temperatures of two yellow rectangles 4-1 and 4-2 with 100 × 10 pixels are calculated to be compared with the temperature measured by thermocouple T1, thereby validating the accuracy of the reconstructed thermal field.

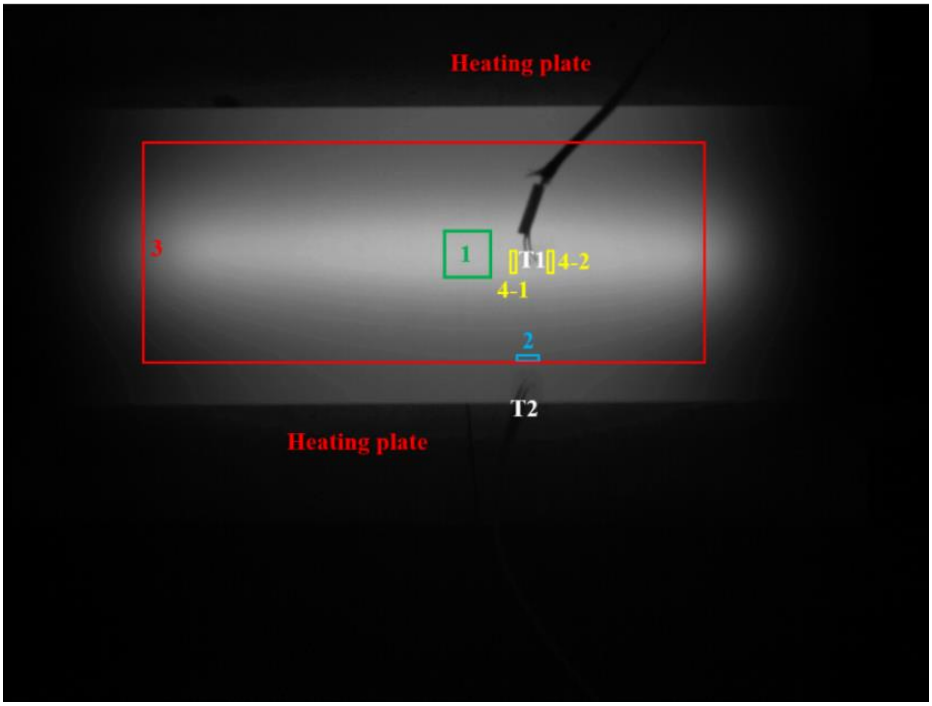

Fig. 3.14: Acquired image of a specimen surface when heated by induction thanks to the plate. Green square is the reference area for exposure time adjustment; blue rectangle 2 is the reference area for radiometric model identification by comparison to thermocouple T2; red rectangle 3 is the area of thermal field reconstruction; yellow areas 4-1 and 4-2 are chosen to validate the thermal field by comparison the thermocouple T1 measurement.

Control of the conservation of the image mean gray level

Fig. 3.15(a) shows the evolution of mean gray level of ROI 1 with/without exposure time adjustment. The red points indicate that without exposure time adjustment the mean gray level of ROI 1 increases fast from original gray level 180 GL to the maximum gray level 255 GL as the temperature of T2 increases from 837 K to 846 K. As the temperature further increases, saturated images are likely obtained without any exploitable information. Some examples of acquired images are shown in Fig. 3.16, in which the gray level of image increases with the increase of temperature at a constant exposure time. As

indicated by blue points in Fig. 3.15(a), with exposure time adjustment the mean gray level of ROI 1 is maintained almost constant as the temperature of T2 increases from 837 K to 962 K. The corresponding exposure time after automatic adjustment of exposure time during heating process is shown in Fig. 3.15(b). One can observe that the exposure time decreases from 75 ms to 5 ms to maintain the mean gray level stable when the temperature increases. Some examples of acquired images are shown in Fig. 3.17, in which the mean gray level of the image is maintained stable with the increase of temperature. These results further indicate that the algorithm and software are feasible and reliable.

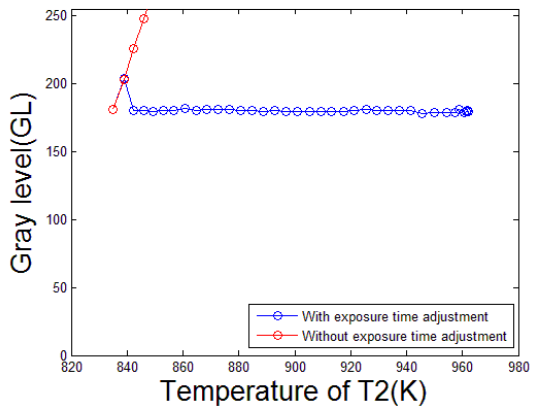

(a) Mean gray level evolution of ROI 1.

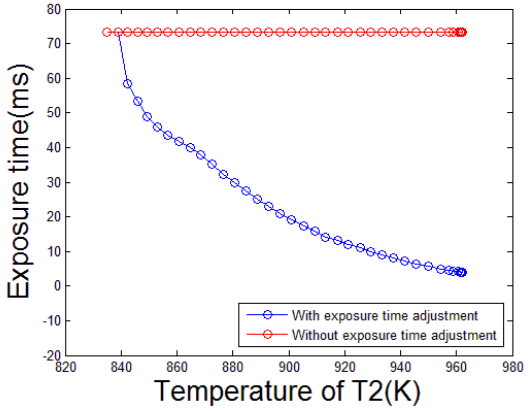

(b) Exposure time evolution after exposure time adjustment.

Fig. 3.15: Mean gray level of ROI 1 and exposure time evolves as the temperature of T2 increases with/without exposure time adjustment.

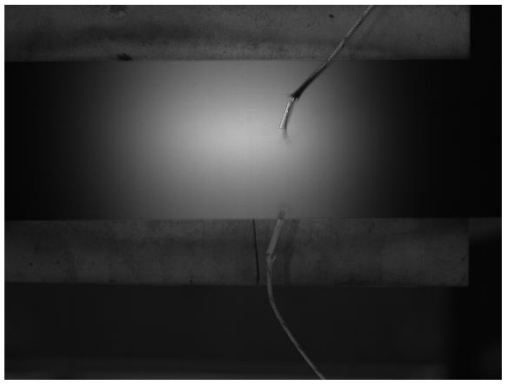

(a) 834.9 K

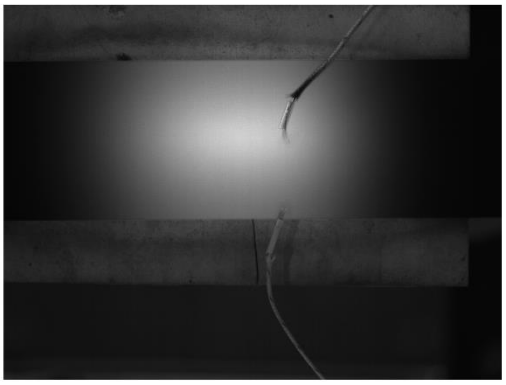

(b) 838.9 K

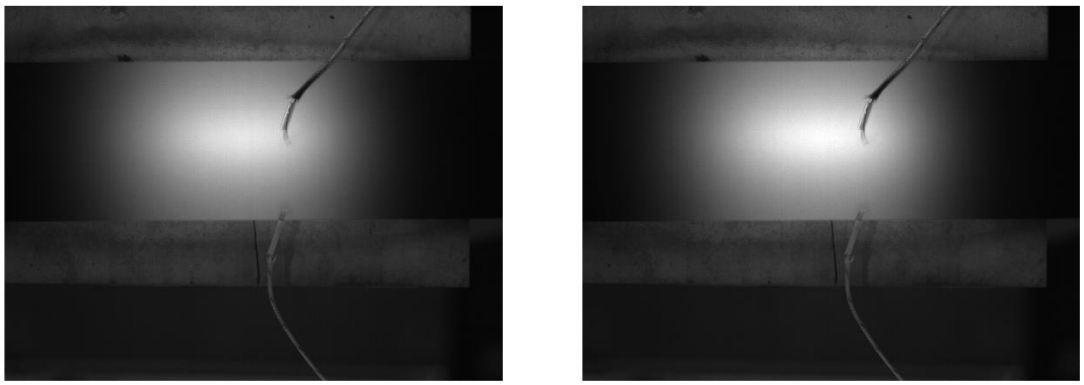

(c) 842.4 K (d) 845.9 K

Fig. 3.16: Some images acquired at various temperatures of T2 at constant exposure time.

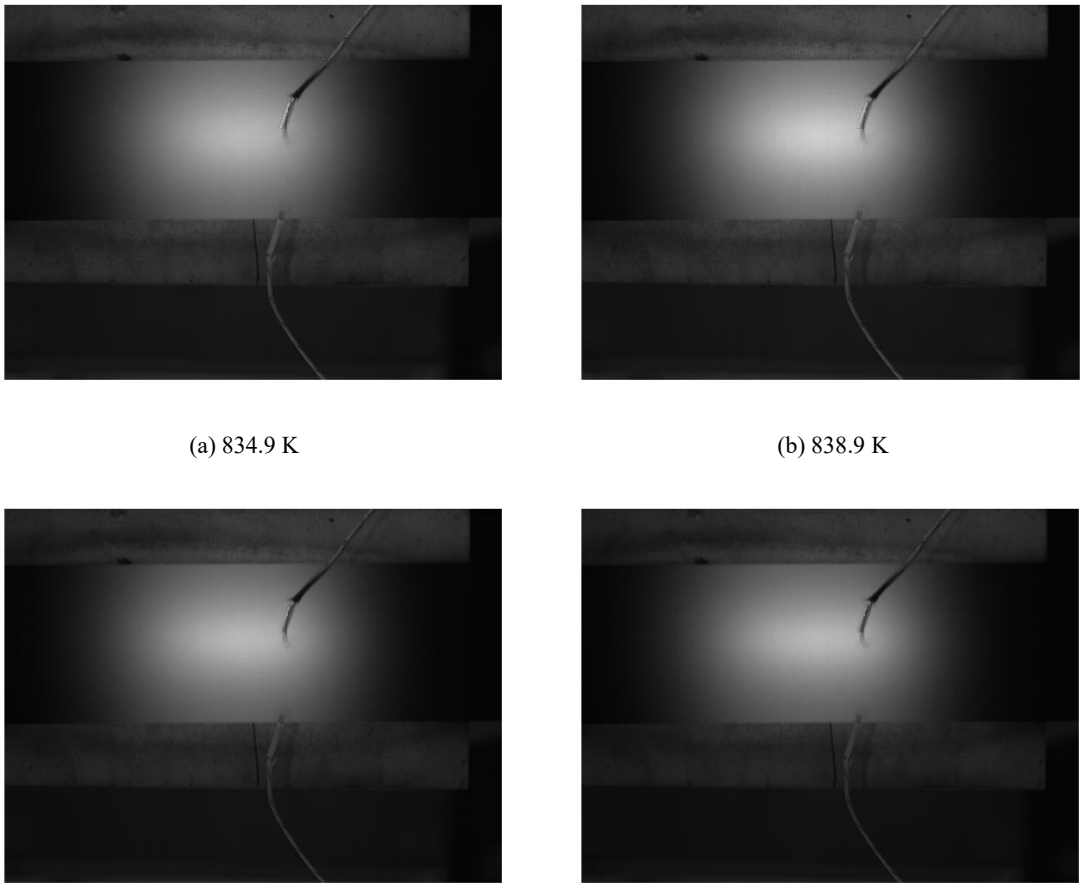

(a) 834.9 K (b) 838.9 K

(c) 842.4 K (d) 845.9 K

Fig. 3.17: Some images at various temperatures of T2 acquired with exposure time adjustment.

Calibration of radiometric model

The blue ROI 2 with 100 × 10 pixels is used to calibrate the radiometric model. Mean gray level of ROI 2 and the reference temperatures provided by thermocouple 2 (T2) is shown in Fig. 3.18. Based on the experimental data, the radiometric model (red curve) is calibrated by using the least square method. Through calibration procedure, three parameters k_w, a_0 and a_1 of radiometric model are identified, as indicated in Table 3.2. Thus, in this case the radiometric model of titanium alloy specimen surface can be given as follows:

$$I_n = \frac{I}{\tau} = 3.02\times10^{11} \times \exp\left(-\frac{1.849\times10^4}{T} + \frac{4.349\times10^5}{T^2}\right) \tag{3.6}$$

The temperature errors of the calibrated radiometric model are also shown in Fig. 3.19, in which the maximum error is 2.5 K.

Table 3.2: Three parameters of radiometric model of titanium alloy specimen surface.

k_w (GL/s)	a_0 (m^{-1})	a_1 ($K\cdot m^{-1}$)
3.02×10^{11}	1.284×10^6	-3.02×10^7

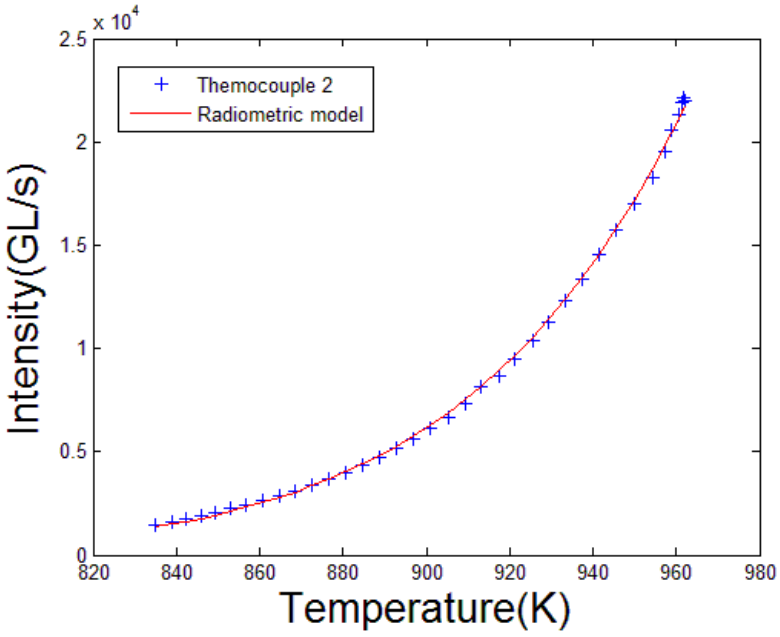

Fig. 3.18: Experimental data and radiometric model.

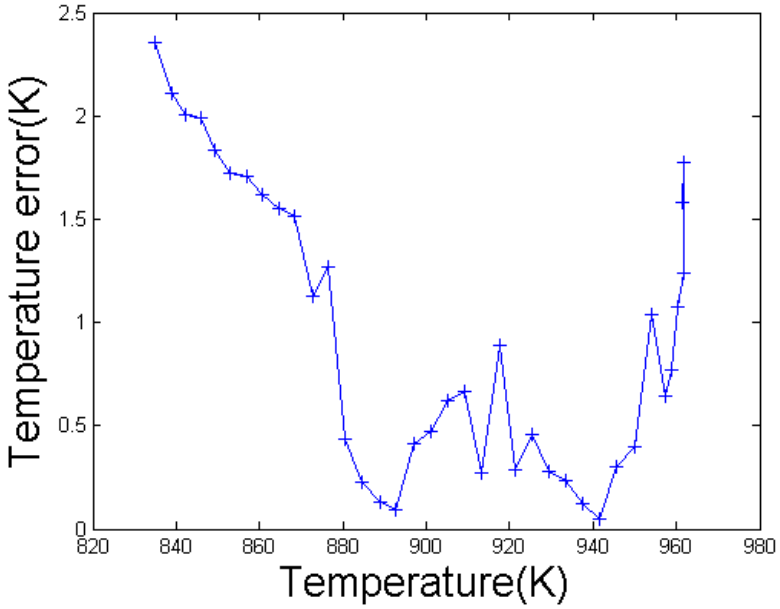

Fig. 3.19: Temperature errors of the radiometric model.

Thermal field reconstruction

Thermal field of the red ROI 3 is chosen to be reconstructed. Some reconstructed thermal fields at various measured temperatures by T1 are shown in Fig 3.20. It can be found that the thermal fields of specimen surface are also non-uniform in this case. The temperature distribution along the white dotted line (Fig. 3.20(a)) is analyzed, and the horizontal ordinate of the line is No. 1500 pixel. The temperature distribution along the line at different temperatures is shown in Fig. 3.21. It is seen that the temperature gradients on the specimen surface increase as the temperature increases. This indicates that the heating plate is inferior to the heat coils in maintaining the temperature gradient. In addition, the thermocouple (T1) is used to validate the accuracy of the reconstructed thermal fields. Since the thermocouple T1 is in the center of the specimen surface, the mean temperatures of two yellow rectangles (4-1 and 4-2) are chosen to be compared with the measured temperatures. Fig. 3.22 shows the temperature errors between the measured and calculated temperatures. The result indicates that most of errors are less than 3 K, which proves this technique is accurate and reliable.

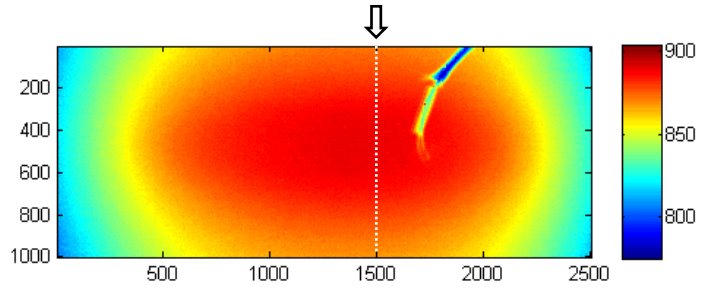

(a) 864.8

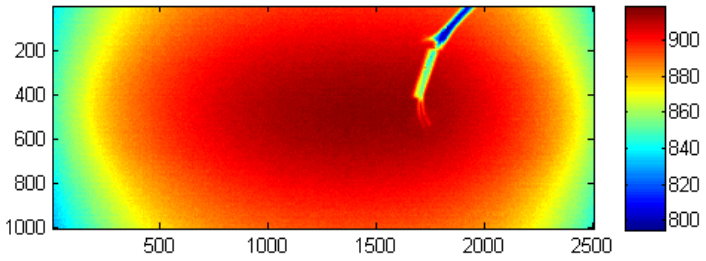

(b) 892.7

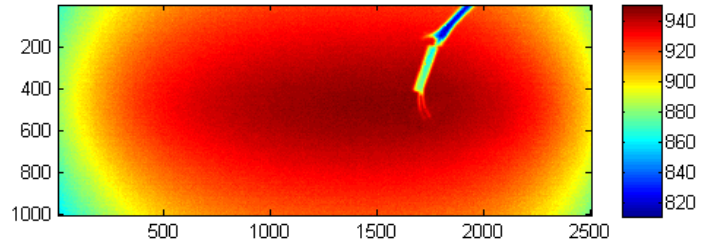

(c) 921.2

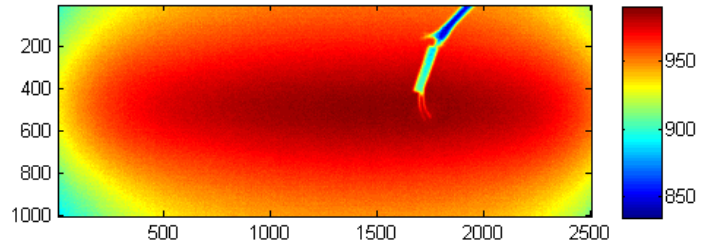

(d) 949.8

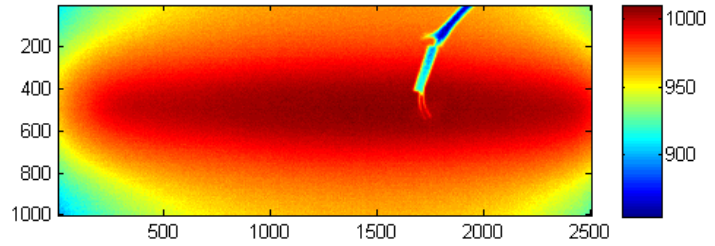

(e) 961.6

Fig. 3.20: Reconstructed thermal fields at various temperatures measured by T2.

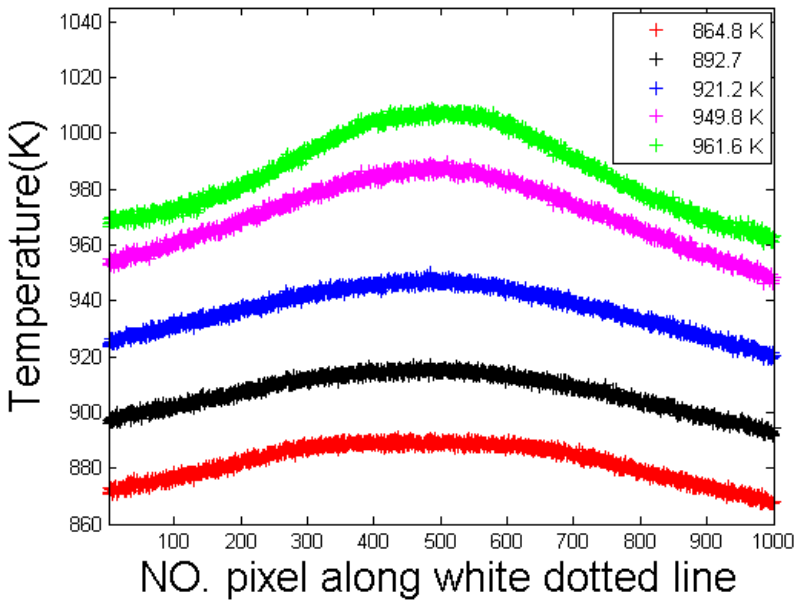

Fig. 3.21: Temperature distribution along the white dotted line.

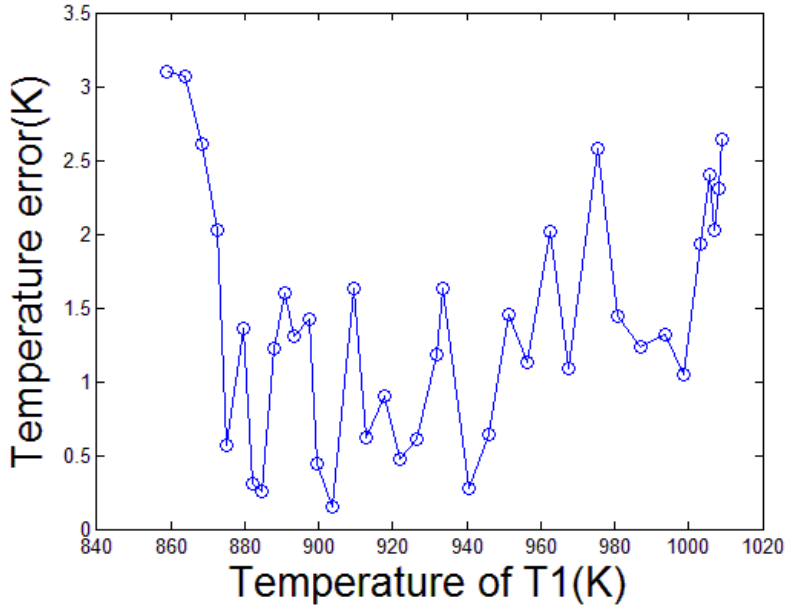

Fig. 3.22: Temperature error between the calculated temperatures and temperatures measured by thermocouple T1.

3.4 Conclusions

Thermal fields of both blackbody experiments and realistic experiments are reconstructed in this chapter. The temperature of each pixel can be calculated based on the radiometric model and recorded images. Thermal fields and error fields of blackbody images are reconstructed, and both fields are uniform. Mean temperature errors are about 1 K.

A steel specimen is heated under induction heating coils. During the heating process, the mean gray level of the acquired images can be maintained almost constant. A radiometric model of steel specimen surface can be obtained as follow:

$$I_n = \frac{I}{\tau} = 2.12\times10^{11} \times \exp\left(-\frac{1.728\times10^4}{T} + \frac{4.349\times10^5}{T^2}\right)$$

Based on this radiometric model, the thermal fields of specimen surface are reconstructed. Most of the temperature errors are less than 1.5 K. The temperature distribution is enhanced, and the result indicates that the temperature gradients provided by the heating coils have slight change with the increase of heating temperature.

A second experiment has been performed on a different material. A titanium alloy specimen is heated under induction heating plate. During the heating process, the gray level of the acquired images can be maintained almost constant. The radiometric model of titanium alloy specimen surface can be calibrated as follow:

$$I_n = \frac{I}{\tau} = 3.02\times10^{11} \times \exp\left(-\frac{1.849\times10^4}{T} + \frac{4.349\times10^5}{T^2}\right)$$

Based on this radiometric model, the thermal fields of specimen surface are reconstructed. Most of errors are less than 3 K. The temperature distribution is analyzed, and the result indicates that the temperature gradients provided by the heating plate dramatically change with the increase of heating temperature.

As a conclusion, this chapter demonstrates that the developed software is able to automatically adjust the exposure time of a common camera in order to maintain the mean grey level of an area stable. Knowing the exposure time and analyzing the grey level over an area are available, a simplified radiometric model can be identified.

This radiometric model can then be used to reconstruct pixel wise thermal field at different temperature over a larger area of interest. The whole developments have been applied in both uniformed fields (images of a blackbody) and realistic thermo-mechanical tests at high temperature for two different materials. The estimated temperature reconstruction errors are quite low compared to the real temperature of the scene during the tests. Thus this chapter has demonstrated that the developed acquisition algorithm and reconstruction methods are efficient and reliable for the thermo-mechanical characterization applications and could be used for simultaneous thermal and kinematic field measurements in Chapter 4.

Chapter 4
Coupling kinematic and thermal fields

This chapter focuses on coupling kinematic and thermal fields. Digital image correlation and near-infrared thermography simultaneously perform on the same images. Both fields are obtained at the same spatial and temporal coordinates.

Contents

4.1 Introduction

Many experimental procedures (for instance welding, materials forming, heat treatment, fatigue, damage, etc.) involve both high temperature and deformation, and sometimes, localized phenomena (phase transformation, cracking, friction, and so on). In these applications, measuring both deformation and temperature distribution can provide relevant information. Digital image correlation is an advanced technique, which can be used for non-contact full-field kinematic measurement of object surface. Infrared thermography is commonly used for non-contact full-field thermal measurement of object surface. If both kinematic and thermal fields can be obtained at the same spatial and temporal coordinates by digital image correlation and infrared thermography, it can offer invaluable experimental data for thermo-mechanical procedures.

Many researchers have contributed to integrating both kinematic and thermal fields. Using two different imaging systems to obtain simultaneously these two fields is the most common method: silicon-based cameras for acquiring kinematic field and infrared cameras for acquiring thermal field. Then, a *posteriori* data processing was conducted to integrate the space and time associations of these two fields. For instance, Chrysochoos et al. [CHR 10] studied the thermomechanical behavior of materials by using a CCD camera and an infrared camera. CCD camera provided the in-plane displacement field by digital image correlation, while infrared camera provided the thermal field by infrared thermography. Harzallah et al. [HAR 18] used a bi-spectral apparatus (a CMOS high speed camera and an infrared camera) to simultaneously measure kinematic and thermal fields in orthogonal cutting experiment. However, this method has several essential problems which are difficult to be solved:

- The two different imaging devices (silicon-based camera and infrared camera) have different spatial resolution and acquisition rates. The exact same spatial and temporal coordinates of these two fields cannot be achieved no matter how well the *posteriori* data processing is done.
- The two techniques have conflicting requirements for the specimen surface. Digital image correlation needs a heterogeneous and contrasting texture on the specimen surface to be tracked, while infrared thermography needs a homogeneous and constant emissivity on the surface to be measured.
- The combination of these two imaging systems is expensive. Special experimental set-up should be conducted to combine these two imaging systems by special filters and other installations due to the different spectral ranges acquired by these two systems.

To avoid the aforementioned problems, some researchers tried to obtain these two fields using a single camera. Maynadier et al. [MAY 12] used a single infrared camera to perform infrared image correlation to obtain both kinematic and thermal fields. However, the infrared camera delivered rather poor fields due to its low resolution. Silicon-based cameras, which are widely used to perform real-time observation of the kinematic fields thanks to digital image correlation, have high resolution, and are operating in both the visible spectrum (0.4-0.75 μm) and the near-infrared spectral range (0.75-1.1 μm).

Thus, silicon-based cameras can also be used to obtain thermal fields by near-infrared thermography. They are good candidates to measure both kinematic and thermal fields.

Orteu et al. [ORT 08] used a single CCD camera to measure both displacement and temperature fields. However, the problem that heterogeneous specimen surface possesses different emissivity cannot be addressed, thus the temperature they obtained is just the apparent temperature (i.e., radiation intensity) and the true temperature field cannot be obtained.

In this chapter, the previously introduced technique (see Chapters 2 and 3) is proposed to measure simultaneously kinematic and thermal full fields using a single CMOS camera. Tube ballooning test was conducted at varied temperatures, and images were acquired using a CMOS camera. The homemade software, based on the Planck algorithm, was used to automatically adjust the exposure time of the camera to obtain visible images with stable mean gray level whatever the temperature evolution was. The kinematic field was obtained by global digital image correlation technique. Based on a calibrated radiometric model, the true thermal field can be obtained. Finally, the two fields are obtained at the same coordinates in both reference and deformed images.

4.2 Tube ballooning experiments

4.2.1 Materials and experimental set-up

The material used in this study is Zircaloy alloy, of which the chemical composition (wt.-%) is Zr-1.29Sn-0.21Fe-0.11Cr-0.13O-0.016C. The specimen is 90 mm cladding tube with outer radius of 4.75 mm and wall thickness of 0.57 mm. The tube surface was firstly sprayed with black paint as undercoating, followed by randomly spraying white paint as a speckled pattern.

Schematic diagram of experimental set-up is shown in Fig. 4.1, which enables the tube ballooning tests at elevated temperature. This experimental set-up consists of some main elements: (a) a tube specimen with speckled surface; (b) an enclosure surrounding the specimen to maintain an argon environment in order to avoid severe oxidation; (c) an induction heating device; (d) a 10 kN servo-hydraulic machine to provide internal pressure with argon; (e) a 8bits CMOS camera (Viewworks VC-12MC) with 4096 × 3072 pixels, mounted with a lens (Nikon ED, 200 mm) to shoot images; (f) a pyrometer and a thermocouple to provide the classical temperature measurement (g) a computer to record experimental data (images, exposure time, loading and temperature) and an internal software to automatically adjust the exposure time to maintain the image gray level stable.

The test was conducted in a room without the interference of other heat sources, and the distance between the front lens of the camera and the specimen surface was 1 meter. The thermal loading process is shown in Fig. 4.2(a), in which the temperature was firstly set to 953 K with a heating rate of 10 K/s and followed by maintaining at 953 K for 1 min to ensure the temperature constant. Then the internal pressure of 1.5 MPa with argon was applied to the tube specimen and the temperature of specimen was

heated by coils from 953 K to 1203 K with a heating rate of 1 K/s at the same time. During this tube ballooning process, the CMOS camera acquired the images with an acquisition frequency of 1 Hz and the homemade Labview software was used to automatically adjust the exposure time of the camera to maintain the gray level of the regions of interest (ROI) constant. Finally, the loading was released and the specimen was cooled to room temperature. Before test, the pyrometer is calibrated to make sure that the temperature measured by the pyrometer is equal to the temperature measured by the thermocouple under the same condition.

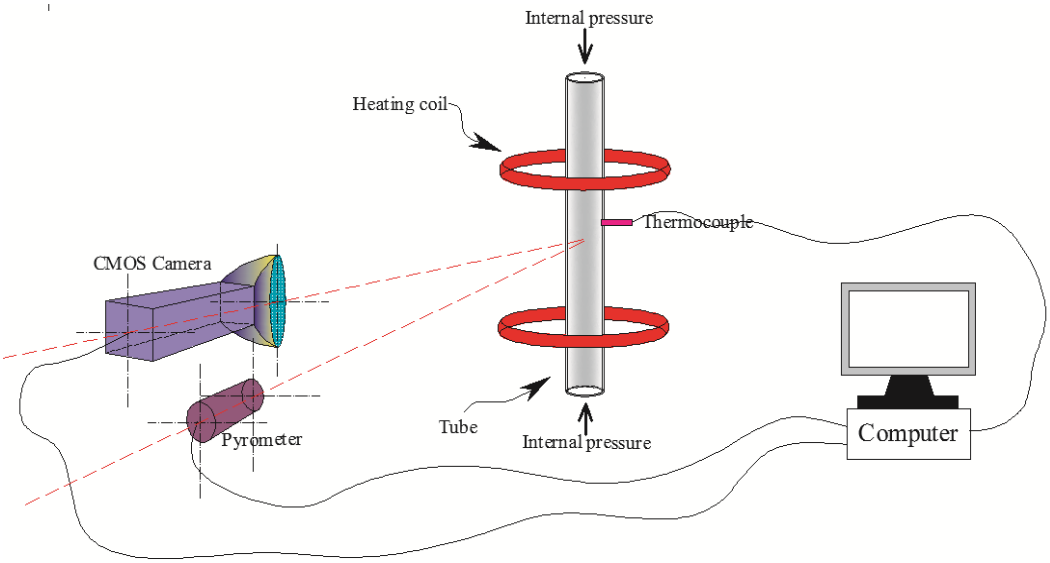

Fig. 4.1: Experimental set-up of tube ballooning tests.

Fig. 4.2(b) shows the first image (rotated 90 degrees counterclockwise) acquired by the CMOS camera, in which different regions of interest (ROI) have different functions. Green rectangle 1 is the chosen ROI with 300 × 200 pixels, where the mean gray level of this region is intended to be maintained stable by automatically adjusting the exposure time of camera. The white dot cycle is the measurement region of the pyrometer. Thus, a blue ROI 2 with 100 × 100 pixels within this measurement region of pyrometer is chosen for the radiometric model calibration based on the reference temperature measured by pyrometer. Red ROI 3 with 900 × 900 pixels is the chosen region to reconstruct the thermal field by near-infrared thermography. The mean temperatures of the yellow ROI 4 with 100 × 100 pixels is used to be compared to the temperatures measured by thermocouple, thereby validating the accuracy of the radiometric model. It is also worth noting that bright regions in the image shown in Fig. 4.2(b) are the regions sprayed with black paint, while the dark regions are the regions sprayed with white paint. These opposite phenomena between room temperature and high temperature are due to that the black paint has high emissivity and white paint has low emissivity, thus the black paint is brighter than white paint at high temperature.

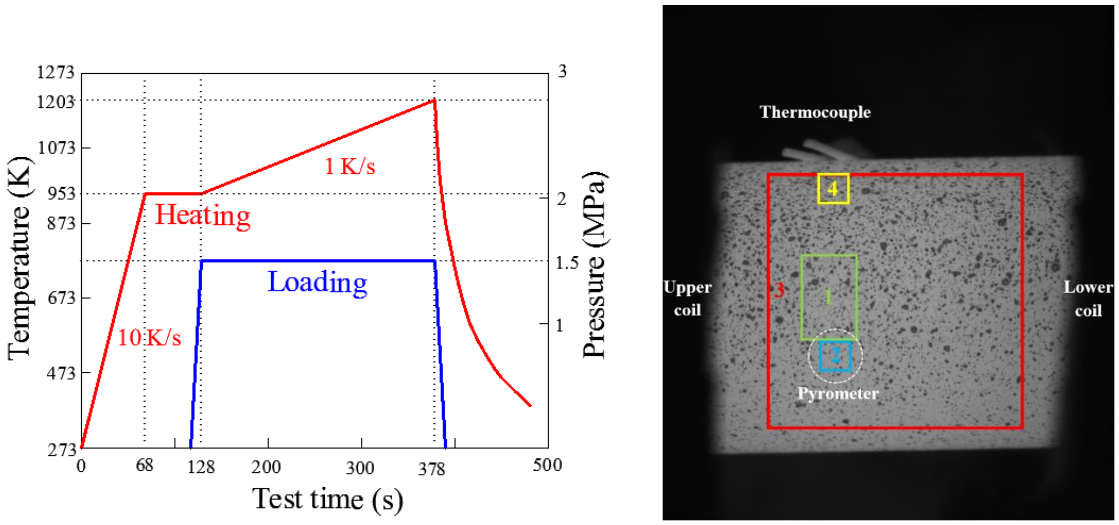

(a) Thermal loading procedure.

(b) An acquired image.

Fig. 4.2: Thermal loading procedure and an acquired image.

4.2.2 Control of image gray level

As depicted by the red points in Fig. 4.3(a), the mean gray level of green ROI 1 (Fig. 4.2(b)) increases fast from the original gray level of 143 GL to the maximum gray level of 255 GL with a temperature increment of only 30 K. As the temperature further increases, the acquired images would be unreadable due to the over saturation and couldn't provide any useful information. Some examples of acquired images are shown in Fig. 4.4, in which the gray level of image increases with the increase of temperature at the constant exposure time. In order to perform both digital image correlation and near-infrared thermography, the image gray level should be maintained stable as much as possible with temperature variation.

With exposure time adjustment using the software based on Planck's algorithm, the mean gray level of green ROI 1 (blue points in Fig. 4.3(a)) can be almost maintained constant as the temperature increases from 953 K to 1203 K. The corresponding exposure time after adjustment is shown in Fig. 4.3(b), where the exposure time decreases with the increase of temperature. Some examples of acquired images are also shown in Fig. 4.5, in which the gray level of image is maintained stable with the increase of temperature when the exposure time is automatically adjusted. This result further indicates that the algorithm and software are reliable and effective when the heterogeneous surface is investigated.

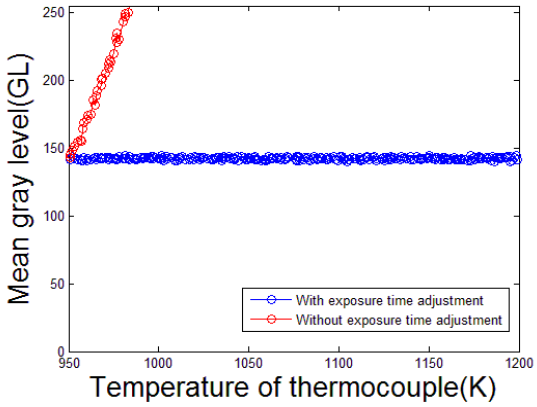

(a) Gray level evolution.

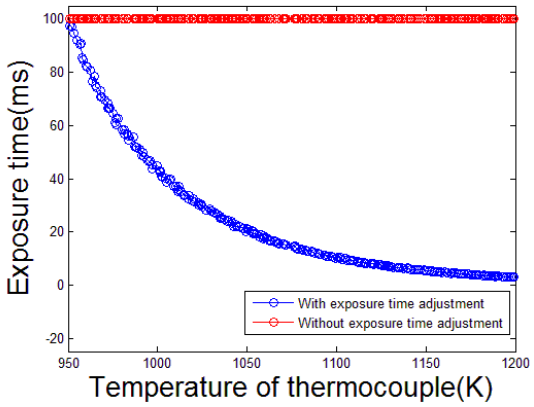

(b) Exposure time evolution after exposure time adjustment.

Fig. 4.3: Gray level and exposure time evolves with the increase of temperature with/without exposure time adjustment.

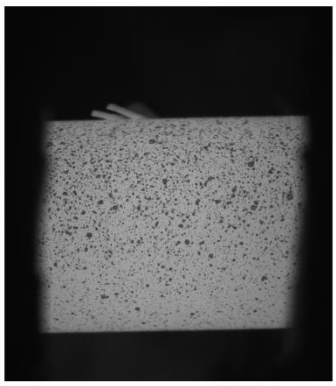

(a) 950.7 K

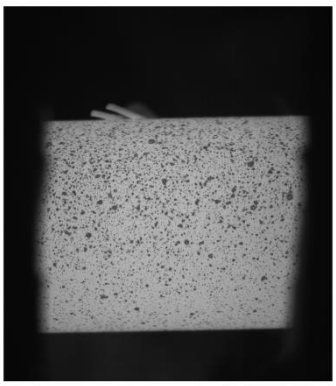

(b) 957.3 K

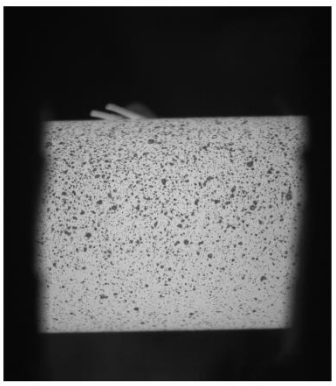

(c) 962.6 K

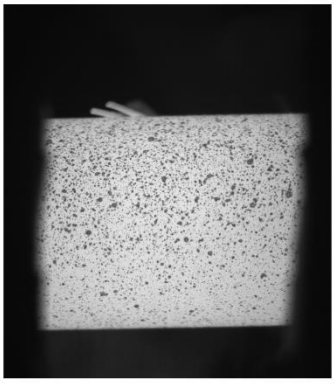

(d) 968.5 K

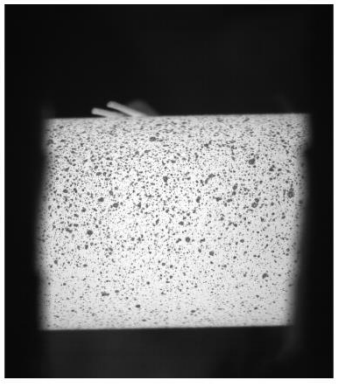

(e) 975.3 K

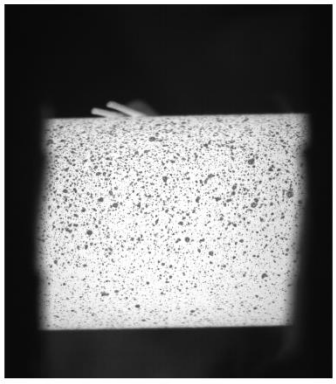

(f) 977.9 K

Fig. 4.4: Some images acquired at various temperatures of thermocouple at constant exposure time.

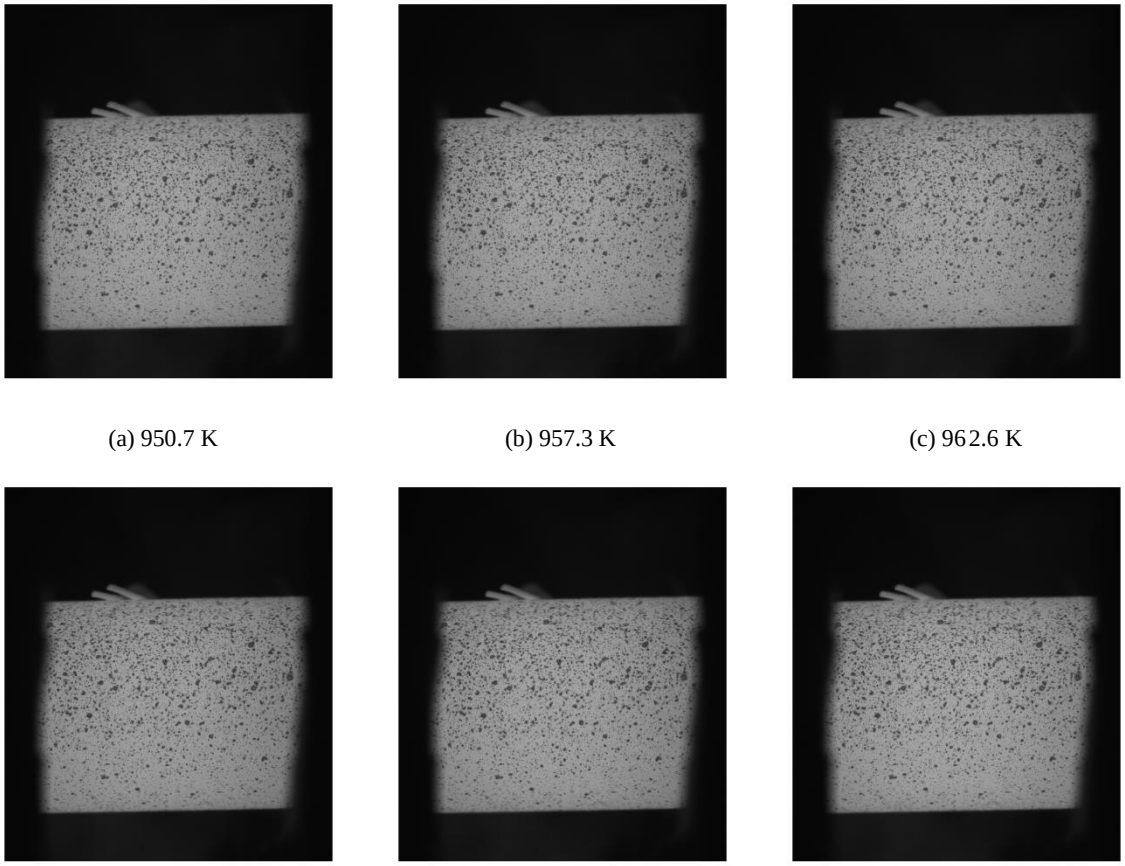

(a) 950.7 K (b) 957.3 K (c) 962.6 K

(d) 968.5 K (e) 975.3 K (f) 977.9 K

Fig. 4.5: Some images acquired at various temperatures of thermocouple with exposure time adjustment.

4.3 Kinematic field on specimen surface

4.3.1 Basic principle of global digital image correlation

In this study, 2D-DIC is performed using the homemade software UFreckles [RET 10a][RET 10b][RET 18]. The image correlation is based on the assumption of the optical flow conservation:

$$f(x) = g(x + u(x)) \tag{4.1}$$

where two functions $f(x)$ and $g(x)$ correspond to the gray levels of the reference image and the image deformed at the position x (where x represents the vector (x, y)). The correlation of two images aims to find the displacement field u solution of the equation of the optical flow conservation in the ROI. By spraying speckles on the specimen surface, it is possible to follow the displacement of the patterns during the test and thus to calculate the surface displacement field. This process is performed by minimizing the following function using a least square method:

$$Er^2 = \left[f(x) - g(x + u(x)) \right]^2 \tag{4.2}$$

In order to solve this correlation equation, several methods can be used. One is a local method, which consists of cutting the images into thumbnails and finding the transformation for each thumbnail, and all thumbnails are independent with each other. In order to obtain the continuous displacement and strain fields on the whole specimen surface, the global method is used in this case. Global methods has the advantage of obtaining a displacement field more representative of the reality, when a continuum medium is observed. The displacement field $u(x)$ is described as follow:

$$u(x)=\sum_{i\in N} u_i N_i(x) \tag{4.3}$$

where $N_i(x)$ are the shape functions, and u_i are the degrees of freedom. A development of Taylor at order 1 of the function g is given as follows:

$$g(x+u(x))=g(x)+u(x)\cdot\nabla g(x) \tag{4.4}$$

Substituting Eq. (4.4) into Eq. (4.2) yields:

$$Er^2=\left[f(x)-g(x)-u(x)\cdot\nabla g(x)\right]^2 \tag{4.5}$$

Substituting Eq. (4.3) into Eq. (4.5) yields:

$$Er^2=\left(f(x)-g(x)\right)^2-2\left(f(x)-g(x)\right)\left(\sum_{i\in N} u_i N_i(x)\cdot\nabla g(x)\right)+\left(\sum_{i\in N} u_i N_i(x)\cdot\nabla g(x)\right)^2 \tag{4.6}$$

Finally, by writing the terms in vector and matrix form, Eq. (4.6) can be given as follows:

$$Er^2=K-2U^TB+U^TMU \tag{4.7}$$

where

$$K=\left(f(x)-g(x)\right)^2$$

$$B=N\cdot\nabla g(x)\cdot\left(f(x)-g(x)\right)$$

$$M=\left(N\cdot\nabla g(x)\right)^T\cdot\left(N\cdot\nabla g(x)\right)$$

M is a square matrix, B and U are column vectors, and K is a scalar that does not depend on displacement. To find the displacement $u(x)$, it is necessary to minimize the Er^2. Thus, its derivative with respect to *u* can be given as follows:

$$\frac{\partial Er^2}{\partial u}=0 \tag{4.8}$$

Thus, it obtains

$$U=M^{-1}B \tag{4.9}$$

It is apparent from Eqs. (4.3) - (4.9) that the choice of the decomposition of the displacement field is crucial for calculating the correlation of images. To date, several shape functions can be chosen to find $u(x)$:

(1) Finite element DIC (FE-DIC): the finite element functions are the basis of the global image correlation [BES 06, SUN 05]. In addition to obtaining a more precise field of displacement than the methods of local correlation, this method is usually used for the identification of material parameters. With a mesh for the correlation of images and the numerical simulation, the material parameters can be calculated [AVR 08][RET 13][HIL 06][LEC 09].

(2) Integrated-DIC (I-DIC): The integrated I-DIC approach takes into account a *priori* the kinematic deformation of the structure. Research quantities are thus taken into account in the degree of freedom of the measure. Some base functions have been proposed: the kinematic of bending beam with a linear curvature [HIL 09] or decomposed on functions NURBS [RET 10b]. A decomposition of the displacement field on the Williams series was also performed to calculate stress intensity factors [ROU 06].

(3) Extended DIC (X-DIC): in the case of cracking, a crack is detected a *posteriori* and the continuity of the displacement field can be raised locally by enriching in the manner of the X-FEM method. X-DIC has been applied to cracking [RET 08] or shear band detection [RET 07b].

4.3.2 Results of digital image correlation

In our study, we will use a correlation of images based on the finite element method (FEM). Element type Q4 [BES 06] with each element of 30 pixels in the reference image is given, as shown in Fig. 4.6. By performing global digital image correlation, four examples of Uy displacement fields along the vertical direction (y axis) are shown in Fig. 4.7. As the tube ballooning proceeds, the displacement along y axis has an obvious increase.

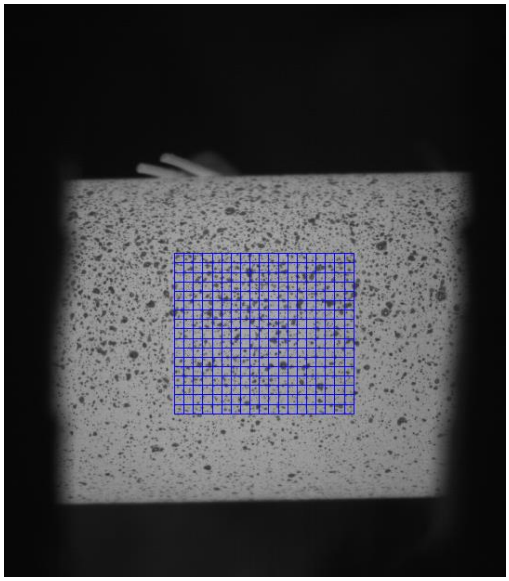

Fig. 4.6: Finite element in the reference image.

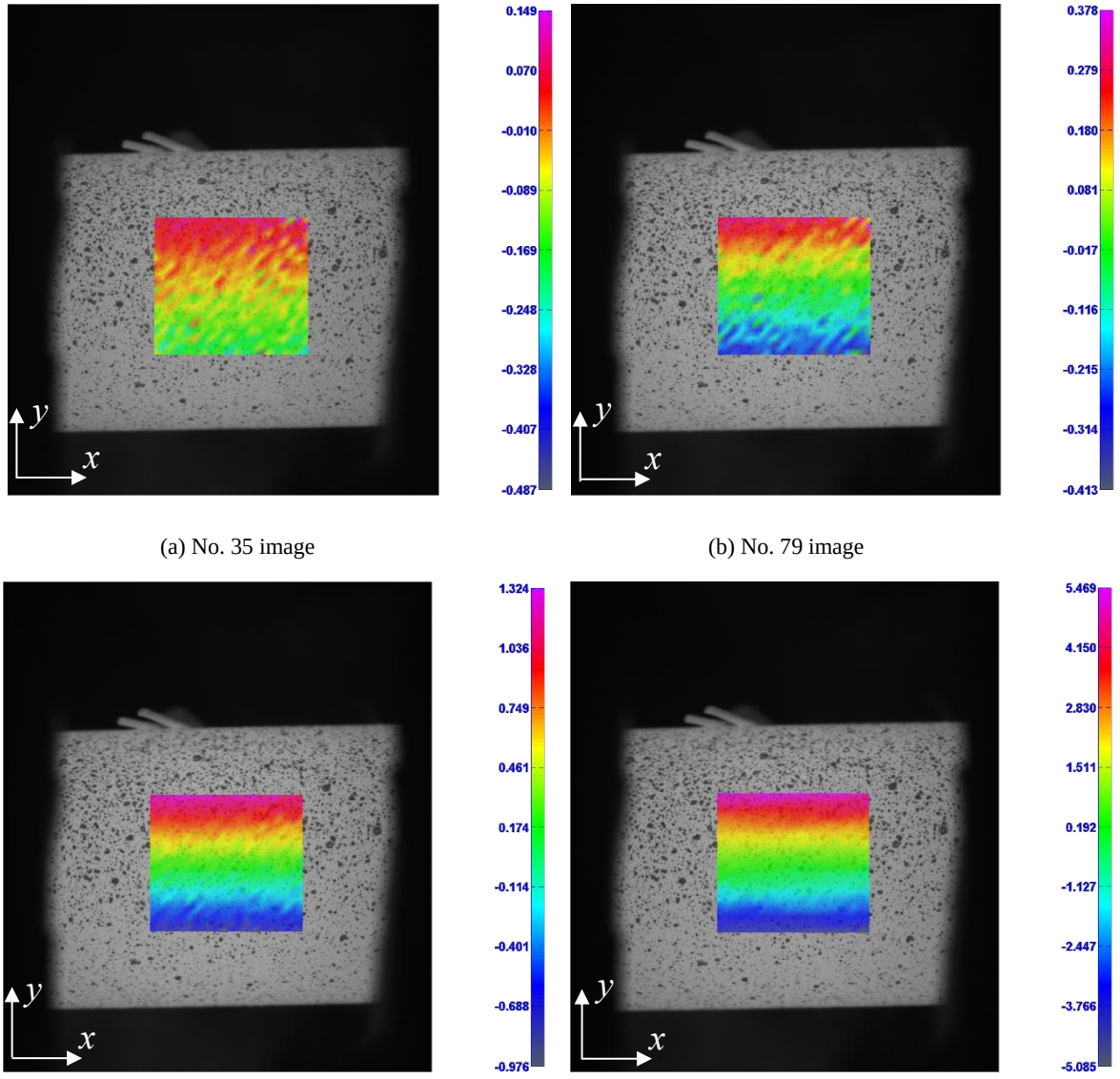

(a) No. 35 image (b) No. 79 image

(c) No. 156 image (b) No. 237 image

Fig. 4.7: Displacement fields (Unit: Pixel) along the direction of y axis.

The method is based on the hypothesis of conservation of gray level. This hypothesis is reasonable, but during the implementation of a test, it is necessary to make sure of the good behavior of certain elements: out-of-plane movements of the specimen, surface or paint flaking, defocusing the optical assembly. To judge the result of the correlation of images, it is necessary to rely on the error of correlation. The error of image correlation is obtained by subtracting the grayscale of the images or the deformed image contains the displacement computes *u*, which can be given as follows:

$$|Er| = |f(x) - g(x + u(x))| \tag{4.10}$$

The error is therefore a field of the same size as the ROI in pixels. If the correlation of images is perfect, then the error should be uniformly zero [RET 10a]. In reality, the correlation error is unavoidable due to some defective pixels or noises, but are still good indicators. The fields of correlation errors of the aforementioned four images are also calculated and shown in Fig. 4.8. The error field is quite uniform and most of pixel errors are less than 4% of the gray level range. These are typically low errors, indicating trustable correlation results.

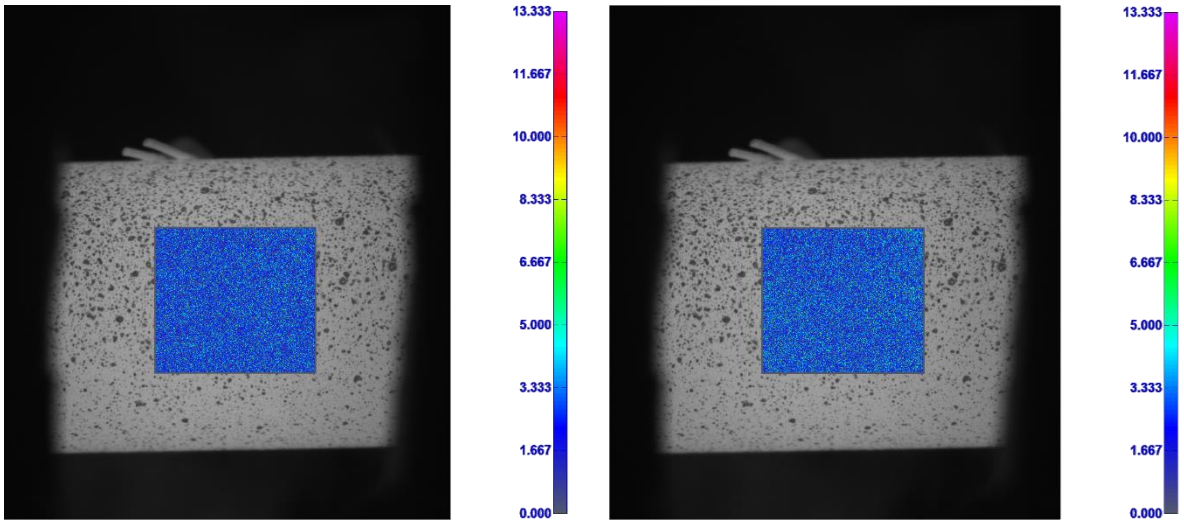

(a) No. 35 image

(b) No. 79 image

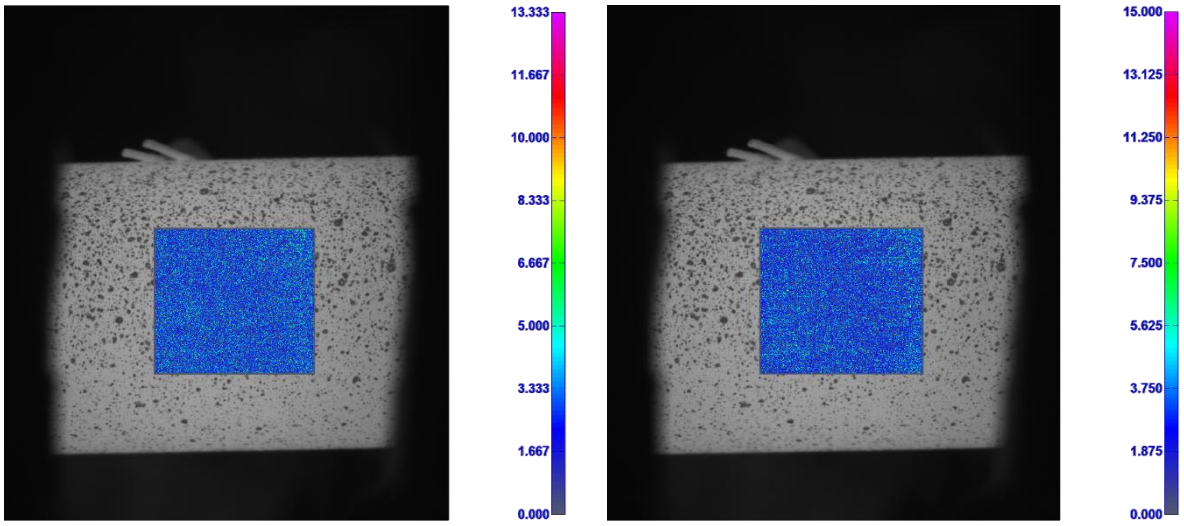

(c) No. 156 image

(b) No. 237 image

Fig. 4.8: Fields of correlation errors (Unit: %).

4.4 Thermal field of specimen surface

4.4.1 Radiometric model

To reconstruct the thermal field on the specimen surface, three unknown parameters (k_w, a_0 and a_1) of the radiometric model should be calibrated. To perform the radiometric model calibration, all 251 images acquired by the camera are used. In these images, the blue ROI 2 with 100 × 100 pixels (as indicated in Fig. 4.2(b)) was chosen for the radiometric model calibration by comparison to the reference temperature provided by the pyrometer. Digital image correlation needs a heterogeneous surface. This is the main difficulty to obtain the kinematic fields by digital image correlation when the thermal field is intended to be simultaneously obtained on the same heterogeneous surface with speckle by near-infrared thermography. Since the specimen surface was sprayed with different emissivity paints (black and white paints), the surface possesses non-uniform surface emissivity. When all pixels of the blue ROI 2 are used to perform the radiometric model calibration, the three parameters of radiometric model based on 100% of pixels are calculated and indicated in Table 4.1, and the corresponding radiometric model curve (pink curve) is shown in Fig. 4.9. Based on these radiometric models, the corresponding thermal fields of ROI 3 can be reconstructed. The mean temperatures of the yellow ROI 4 with 100 × 100 pixels, which can be calculated from the reconstructed thermals field of ROI 3, are compared with the temperatures measured by thermocouple, thereby identifying the accuracy of the thermal field. The temperature error ΔT_{err} is defined as follows:

$$\Delta T_{err} = \left| T_{mea} - \overline{T_{cal}} \right| \tag{4.11}$$

where the T_{mea} is the temperature measured by thermocouple, and $\overline{T_{cal}}$ is mean calculated temperature of ROI 4. During this tube ballooning test, there are 251 images acquired by camera, thus there are also 251 temperature errors ΔT_{err}.

Table 4.1: Three parameters of different radiometric models based on different percents of pixels.

Percent of the brightest pixels (%)	k_w (GL/s)	a_0 (m^{-1})	a_1 ($K \cdot m^{-1}$)
100	1.4565×10^{12}	1.6960×10^{6}	-3.1077×10^{8}
10	1.3696×10^{12}	1.6646×10^{6}	-2.9266×10^{8}
20	1.3567×10^{12}	1.6654×10^{6}	-2.9370×10^{8}
30	1.3242×10^{12}	1.6616×10^{6}	-2.9087×10^{8}

By using radiometric model based on 100% of pixels, the temperature errors of these 251 images are calculated and indicated by pink dots in Fig. 4.10, and the corresponding distribution of these temperature errors (pink rectangles) is shown in Fig. 4.11. One can observe that most of temperature errors are between 4 K and 8 K, which are a little large. These large temperature errors are due to that the radiometric model is calibrated based on the heterogeneous surface, which has two kinds of paints with different emissivity (black and white paints). Using this radiometric model, the accurate temperatures of both black and white paints cannot be calculated.

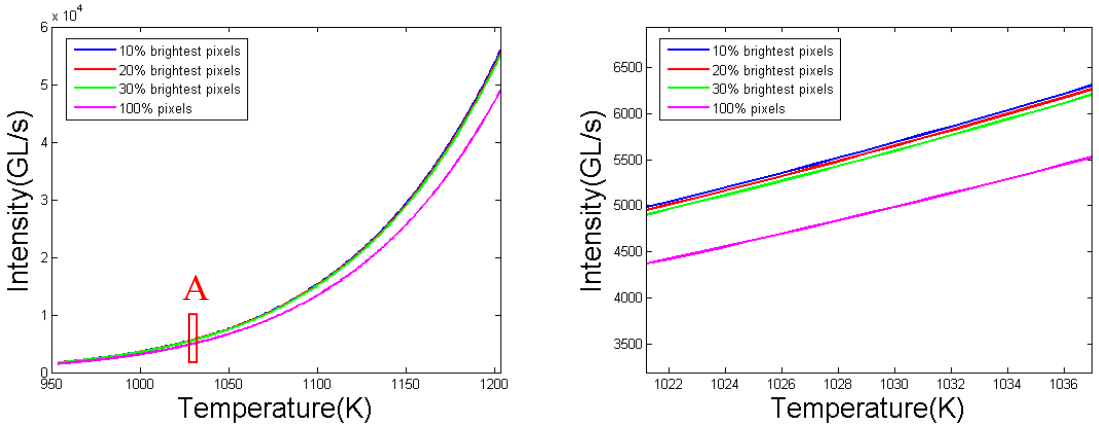

(a) Radiometric models. (b) Magnified A region.

Fig. 4.9: (a) Radiometric models based on different percents of pixels, and (b) magnified A region.

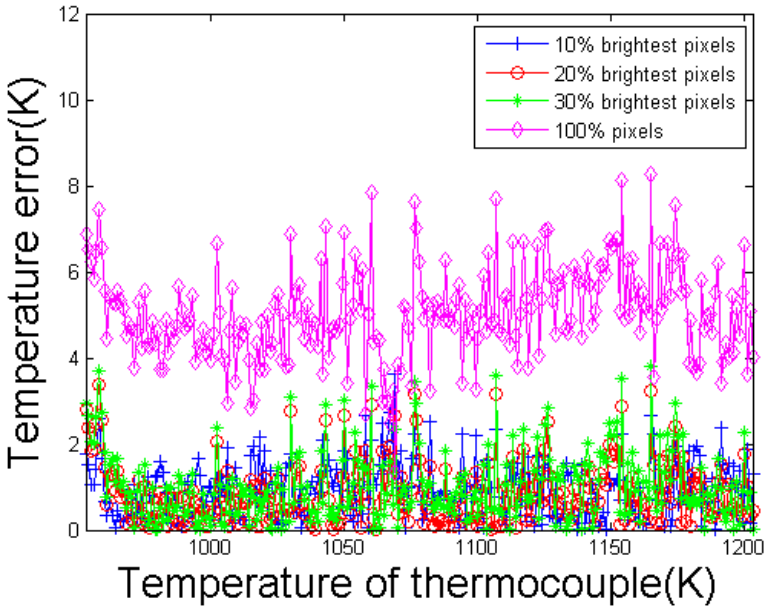

Fig. 4.10: Effect of different percent of pixels on the temperature errors.

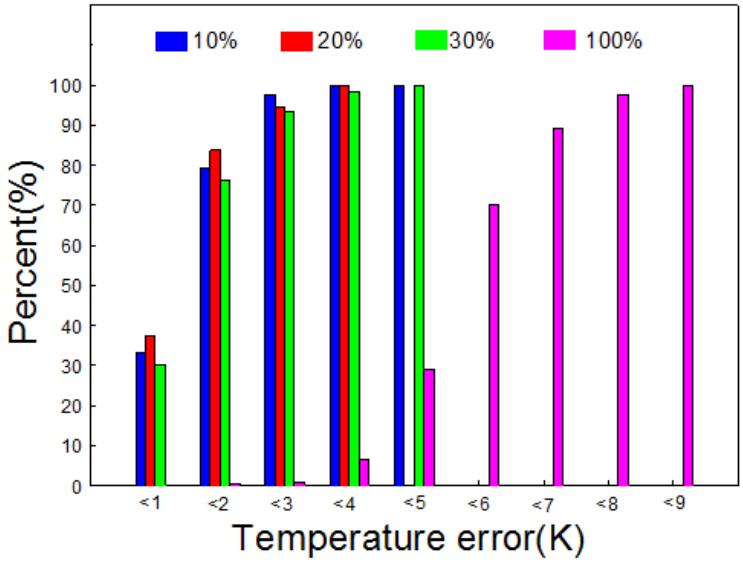

Fig. 4.11: The distribution of temperature errors for different percents of pixels.

To address this problem, a method is proposed in this study, in which parts of the brightest or darkest pixels are chosen to perform radiometric model calibration. The brightest or darkest pixels are unique black paint or white paint on the specimen surface, thus the radiometric model can be calibrated by the homogeneous and constant paint.

In order to know which kind of paint (dark paint or white paint) is better to be considered for radiometric model calibration, a tube with speckle is heated from 953 K to 1203 K for twice, as shown in Fig. 4.12. For each time, both 5% of the brightest pixels (the black paint at room temperature) and the darkest pixels (the white paint at room temperature) are used to calibrate the independently radiometric models. A relative error of intensity between twice heating processes (ς) is defined as follows:

$$\varsigma = \frac{I_{n1}(5\%) - I_{n2}(5\%)}{I_{n1}(5\%)} \times 100\% \tag{4.12}$$

where $I_{n1}(5\%)$ is the intensity of 5% of the brightest or 5% of the darkest pixels during the first heating process, $I_{n2}(5\%)$ is the intensity of 5% of the brightest or the darkest pixels during the second heating process. The relative errors of intensity between twice for 5% of the brightest or 5% of the darkest pixels are shown in Fig. 4.13. It can be found that the relative errors based on 5% of the brightest pixels are smaller and more reliable, while the relative errors based on 5% of the darkest pixels are large at the beginning and then decrease to a low value. The occurrence of this large relative error based on 5% of the darkest pixels is due to that the white paint (the darkness pixels), which has low emissivity, are evidently affected by oxidation, smoking and other noises, while the black paint (the brightest pixels),

which has high emissivity, are not easy to be affected by these noises. Thus, in this study parts of the dark paint (brightest pixels) is a better choice for performing radiometric model calibration.

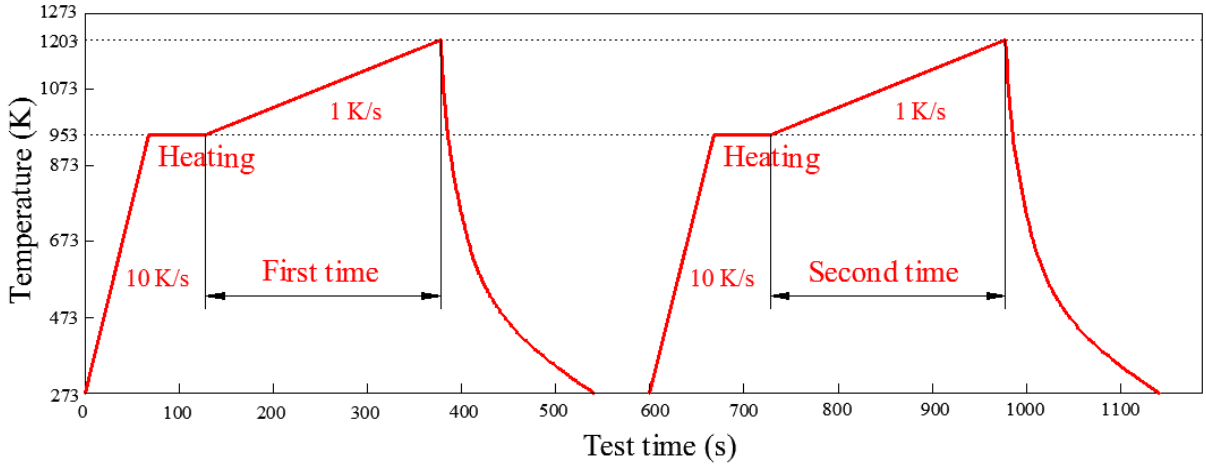

Fig. 4.12: A tube with speckle is heated for twice.

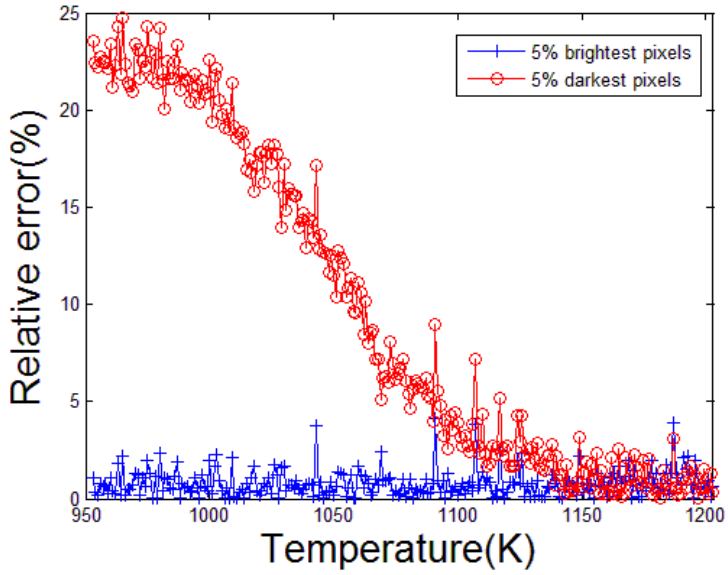

Fig. 4.13: Relative errors of intensity based on 5% brightest and 5% darkest pixels between twice heating processes.

To perform the radiometric model calibration based on parts of the brightest pixels, in this case 10%, 20% and 30% of the brightest pixels are chosen to calibrate the radiometric models. Three parameters of radiometric models based on 10%, 20% and 30% of the brightest pixels are also indicated in Table 4.1, and the corresponding radiometric model curves are shown in Fig. 4.9. The magnified local

region **A** shown in Fig. 4.9(b) indicates that these three radiometric model curves are very approximate. By using these radiometric models, discrete temperature values of the same percents 10%, 20% and 30% of the brightest pixels within the ROI 3 can be calculated, respectively. The whole fields can be reconstructed based on these discrete known temperature values using mathematical methods. In this study, the whole thermal fields of ROI 3 is reconstructed by the fifth order polynomials fitting of these discrete temperature values. An example of the thermal field reconstructed based on 20% of discrete known pixel temperatures is shown in Fig. 4.14, where all black points are the discrete known pixel temperatures and the curved surface is the reconstructed thermal field. After that, the temperature errors between the temperatures measured by thermocouple and the mean calculated temperatures of ROI 4 (ΔT_{err}) of 251 images are calculated and indicated in Fig. 4.10, and the corresponding distribution of these temperature errors is shown in Fig. 4.11. Compared with the results of the radiometric model based on 100% pixels, it can be found that low temperature errors can be obtained for all these three cases. All temperature errors are almost less than 4 K and most of them are less than 2 K. This result demonstrates that the radiometric model calibrated based on the homogeneous and constant paint is a good way to obtain accurate thermal fields, just like the performance in Chapter 3. All these three radiometric models can be considered to perform the reconstruction of thermal fields. However, among these three cases we found that, when the percent of the brightest pixels is 20%, the percent of temperature errors less than both 1 K and 2 K are a little more than those obtained by other two situations, and the number of temperature errors less than 2 K is up to 84%. Thus, we will show the reconstruction of thermal fields based on 20% of the brightest pixels in the following subsection.

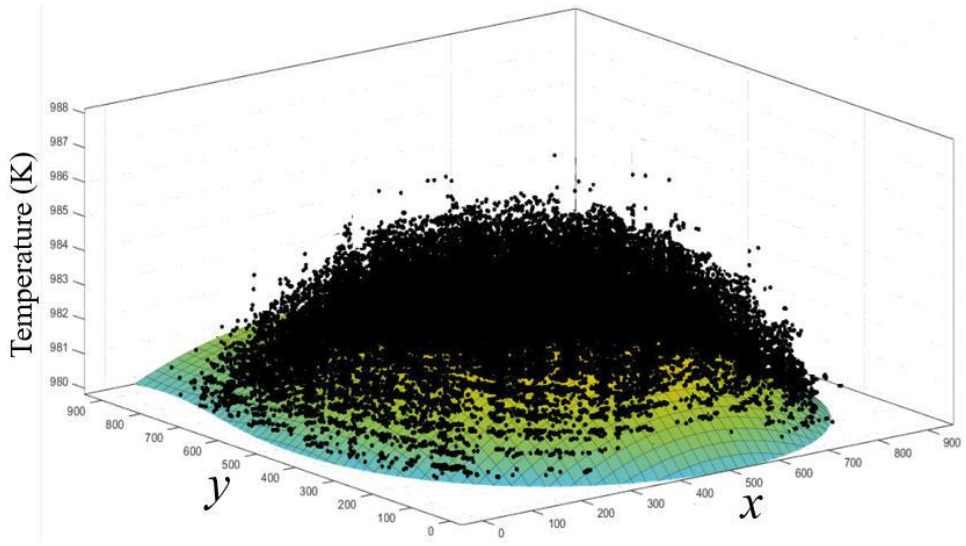

Fig. 4.14: An example of the thermal field reconstructed based on 20% of discrete known pixel temperatures using fifth order polynomial fitting method.

4.4.2 Thermal fields

Based on radiometric model using 20% of the brightest pixels, discrete temperature values of 20% of the brightest pixels within the ROI 3 can be calculated. The whole thermal fields of ROI 3 is reconstructed by the fifth order polynomials fitting of these discrete pixel temperatures. By performing this procedure, four examples of reconstructed thermal fields of ROI 3 on the same images as Fig. 4.7 are shown in Fig. 4.15. To evaluate the fitting results, the discrete temperature errors ΔT_{dis} between discrete known pixel temperatures $T_{discrete}(x, y)$ and the corresponding temperatures in the thermal fields $f(x, y)$ are calculated, which is defined as:

$$\Delta T_{dis} = \left| T_{discrete}(x, y) - f(x, y) \right| \tag{4.13}$$

For each thermal field, there are 162000 discrete temperature errors. Fig. 4.16 is the distribution of all discrete temperature errors for four thermal fields in Fig. 4.15. It is clear that for four thermal fields, above 80% errors are less than 1 K, and above 95% are less than 2K. Meanwhile, the mean discrete temperature errors $\overline{\Delta T_{dis}}$ of four thermal fields are calculated and shown in Fig. 4.17. The mean discrete temperature errors of four thermal fields are between 0.5 K and 0.6 K. These errors are low, which indicates the fitting results are good.

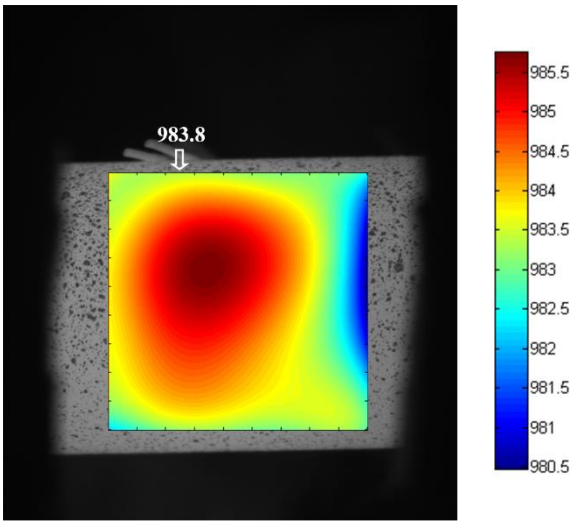

(a) No. 35 image

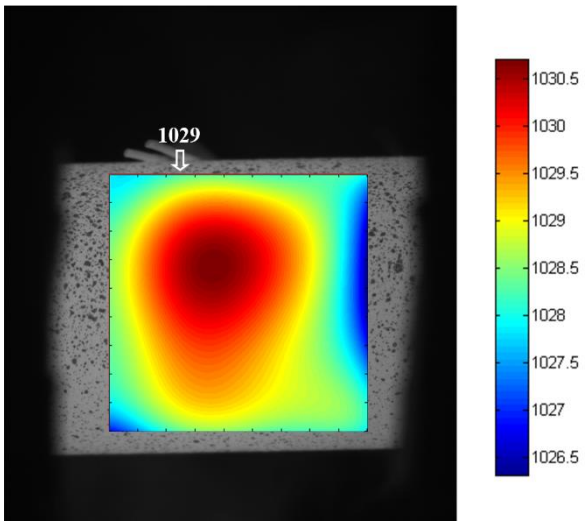

(b) No. 79 image

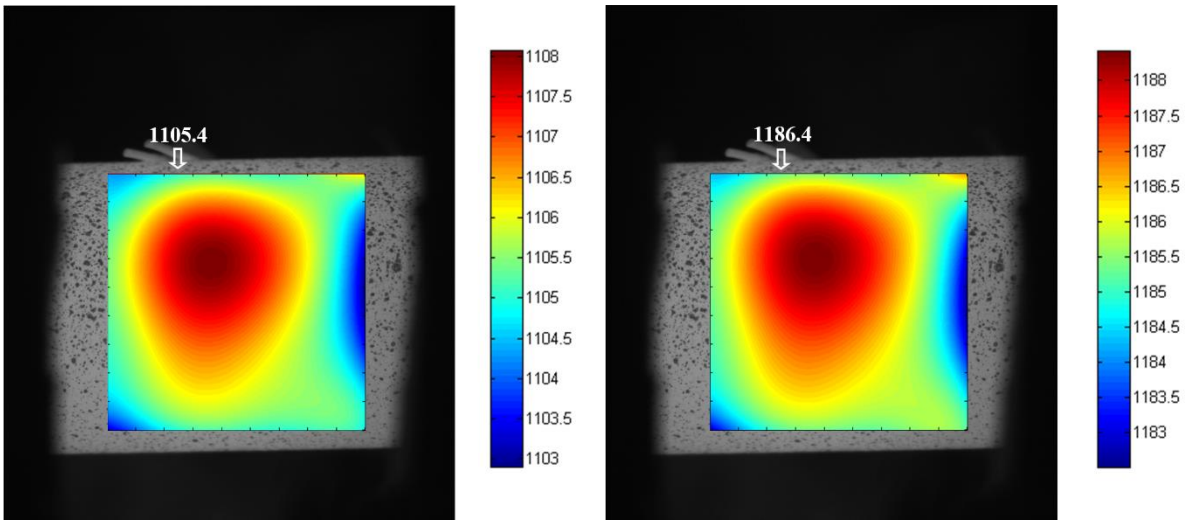

(c) No. 156 image (b) No. 237 image

Fig. 4.15: Reconstructed thermal fields (Unit: K) of ROI 3.

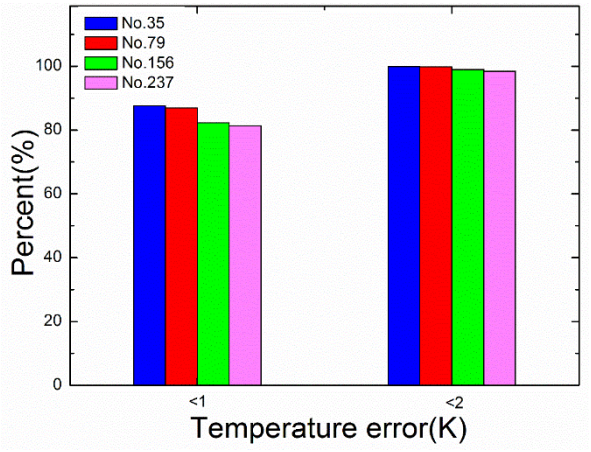

Fig. 4.16: Distribution of 162000 discrete temperature errors of four thermal fields in **Fig. 4.15**.

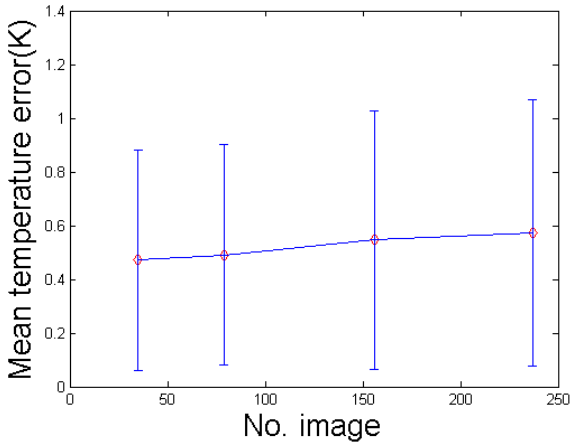

Fig. 4.17: Mean discrete temperature errors of four thermal fields in **Fig. 4.15**.

Nevertheless, the thermal fields of ROI 3 shown in Fig. 4.15 are bigger than the kinematic fields shown in Fig. 4.7. Thus, thermal fields and kinematic fields at the same coordinates in reference and deformed images should be obtained. In DIC analysis, the moved coordinates of kinematic fields are known. Combined with these known coordinates of kinematic fields, the thermal fields at the same coordinates as the kinematic fields in Fig. 4.7 can be cut from Fig. 4.15 and the corresponding thermal fields are shown in Fig. 4.18. Finally, the kinematic fields in Fig. 4.7 and the thermal fields in Fig. 4.18 are obtained on the same images and coordinates, indicating that the exact space and time associations of these two fields can be achieved using a single silicon-based camera.

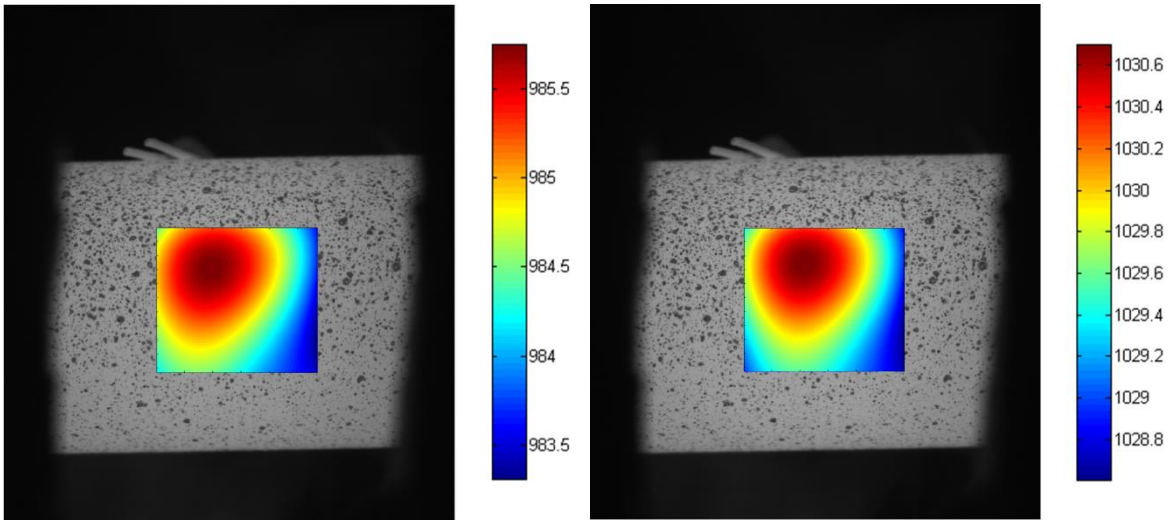

(a) No. 35 image (b) No. 79 image

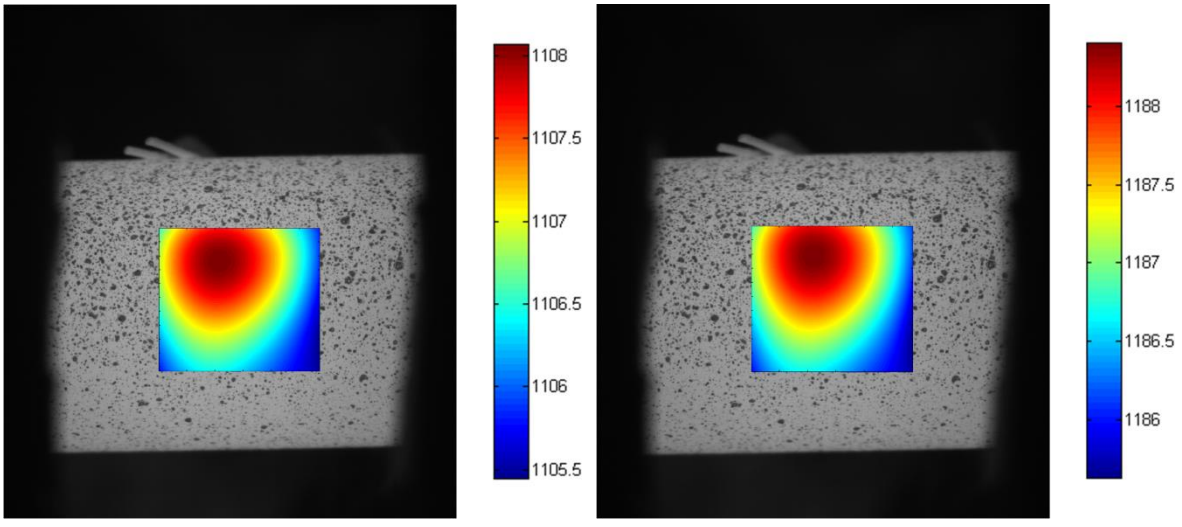

(c) No. 156 image (b) No. 237 image

Fig. 4.18: Thermal field (Unit: K) at the same coordinates as displacement fields shown in Fig. 4.7.

4.5 Conclusions

In this chapter, an innovative technique for measuring simultaneously kinematic and thermal fields is proposed, which has great potentialities to be widely applied in materials science and experimental mechanics. Some main conclusions can be drawn as follows:

A low-cost, high-resolution, easy-to-use silicon-based camera is used to simultaneously obtain kinematic and thermal fields.

The homemade software is successfully used to maintain the gray level of image stable during the heating process of tube specimen with speckle.

Global digital image correlation is performed to obtain the kinematic fields of the specimen surface. The corresponding fields of correlation errors are also obtained and most of the correlation errors are less than 4%. It demonstrates that the exposure time adjustment has successfully delivered images for DIC measurement, despite the high temperature.

To perform near-infrared thermography on the specimen surface with speckle, a radiometric model is calibrated by the analysis of the gray level variation of a small portion of pixels among the brightest. Different percents 10%, 20%, and 30% of the brightest pixels have been tested to calibrate the radiometric models. The temperature errors between the calculated temperatures and the measured temperatures is calculated for each case. The result shows that low temperature errors can be obtained for all these three cases. All temperature errors are almost less than 4 K and most of them are less than 2 K. It demonstrates that the radiometric model calibrated based on the homogeneous and constant paint is a good way to obtain accurate thermal fields.

Based on the radiometric model using 20% of brightest pixels, thermal fields are reconstructed. Combined with the known coordinates of kinematic fields by DIC, the thermal fields at the same coordinates as kinematic fields can be obtained.

General conclusions and perspectives

General conclusions

In this thesis, we have investigated an innovative experimental measurement method for measuring simultaneously kinematic and thermal fields at the same spatial and temporal coordinates using a single type of camera. A low-cost high resolution silicon-based camera, *i.e.* CMOS camera, is used in this study because it not only operates in both visible spectral range (0.4-0.75 μm) and near-infrared spectral range (0.75-1.1 μm). The joint kinematic and thermal full field measurement can provide rich information about the thermo-mechanical loading procedures. This technique can offer a low-cost simplified instrumentation. The major conclusions are drawn below, followed by some perspectives for future investigations.

(I) In Chapter 2, a simple radiometric model equation with three unknown parameters k_w, a_0 and a_1 is firstly derived and used to describe the relationship between gray level of image, exposure time of camera and temperature of the observed object. Three unknown parameters can be calibrated by a few images acquired at different temperatures. Generally, more than three images acquired at different temperatures are enough to calibrate the radiometric model so as to obtain three parameters. This radiometric model is used to blackbody experiments, and the radiometric model of the blackbody is calibrated successfully with low temperature errors. Gray level of image acquired by the CMOS camera is sensitive to the temperature variation. A small temperature variation will cause large modification in image gray level, thereby readily leading to poor quality recorded images due to oversaturation and/or poor dynamic range of gray level. This problem will make the performance of near-infrared thermography and digital image correlation on the acquired images impossible. An innovative approach is proposed to get a series of images with stable gray level whatever temperature evolution is. The basic principle of this approach is that, when the gray level changes with the temperature variation, the gray level is changed to equal to the original value by adjusting the exposure time of the camera. To realize this approach, two algorithms, including linear algorithm and Planck's algorithm, are

proposed to predict the exposure time of next image, in which the Planck's algorithm is derived from the radiometric model. A home-made Labview software based on both linear algorithm and Planck's algorithm is made and used in the heating experiments of a blackbody. The experimental result indicated that a series of images with stable gray level can be obtained by using Planck's algorithm based on the radiometric model; while larger errors will occur by using the linear algorithm. This phenomenon indicates the homemade software based on Planck's algorithm can be used to maintain the image gray level stable when the temperature changes.

(II) In Chapter 3, the basic principle of the reconstruction of thermal fields is firstly introduced, in which the temperatures can be calculated pixelwise when the three unknown parameters of the radiometric model are known and the images are acquired. Then, this method to reconstruct thermal fields is used in the blackbody experiment, which is conducted in Chapter 2. The thermal fields of blackbody images can be reconstructed successfully, and most of temperature errors between the calculated temperatures and measured temperatures are less than 1 K. To further validate the reliability and accuracy of the homemade software to obtain the stable gray level images and the method to reconstruct the thermal fields. Two heating tests of realistic specimens are conducted: heating of steel specimen under two heating coils and heating of a titanium alloy under a heating plate. The experimental results show that the homemade software is efficiently and reliably adjust the exposure time of the camera to obtain stable gray level images during two heating processes. Two radiometric models of two specimen surfaces can be calibrated successfully, and the thermal fields on the specimen surfaces can also be reconstructed based on the calibrated radiometric models. For the heating test of the steel specimen, most of the temperature errors are less than 1.5 K, while most of temperature errors are less than 3 K for the heating test of titanium alloy specimen.

(III) In Chapter 4, the technique of coupling kinematic and thermal fields are investigated. Tube ballooning test is conducted under thermomechanical condition, and the CMOS camera is used to obtain both kinematic and thermal fields on the tube surface. The homemade software is used to maintain the image gray level stable during the test. After the adjustment of the software, stable gray level images are obtained and used for digital image correlation and near infrared thermography. Global digital image correlation is performed to obtain kinematic fields on the tube surface using UFreckles software made by our team. Fields of correlation errors show that most of errors in the fields are less than 4%, indicating that the exposure time adjustment has successfully delivered images for DIC measurement. To perform near-infrared thermography on the heterogeneous specimen surface with speckle, radiometric model is calibrated based on only 20% of brightest pixels. Based on the radiometric model using 20% of brightest pixels, discrete temperature values of 20% of the brightest pixels within the region of interest can be

calculated. The whole thermal field can be reconstructed by the polynomials fitting of these discrete known temperatures. The temperature errors between calculated temperatures thanks to the radiometric model and measured temperatures by thermocouple are also calculated, and most of them are less than 2 K. Finally, combined with the known coordinates of kinematic field by DIC in deformed images, the thermal fields at the same coordinates as kinematic fields can be obtained at the same spatial and temporal coordinates.

Perspectives

The future work could be considered in these aspects:

(I) Development of this technique

In this work, the technique is preliminaryly proposed. Just like the digital image correlation, this technique could be improved better. The accuracy and reliability of the Planck's algorithm can be improved. The thermal field reconstruction on the specimen surface with speckles can be further investigated.

(II) Realistic applications of this technique

This technique can be applied to the study of thermomechanical coupled phenomena: (1) Determination of complex constitutive model (shear bands, phase transformation, and so on); (2) Description and modeling of rupture (cracking, self-heating in fatigue, and so on); (3) Study of the manufacturing processes (modeling/development of the welding/forging, study of the cutting during milling, and so on). This technique can offer accurate information of temperature and deformation, which not only makes us better understand the thermomechanical procedures, such as welding, cracking, etc, but also provides more accurate boundary conditions for numerical simulation of these procedures.

Appendix A

In Fig. 3.4, the blue rectangle 2-2 with 100 × 100 pixels is corresponding to the measured temperature provided by thermocouple 2 (T2). The yellow rectangle 4-1 with 100 × 100 pixels is a chosen region corresponding to the measured temperature by thermocouple 1 (T1), while the yellow rectangle 4-2 with 100 × 100 pixels is a chosen region corresponding to the measured temperature by thermocouple 3 (T3).

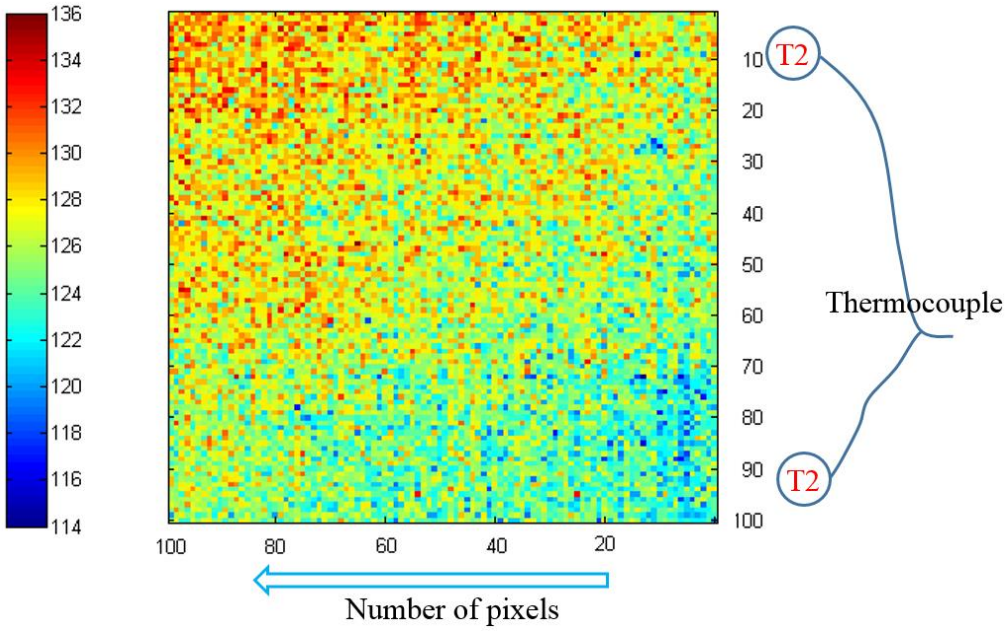

Fig. A1: Gray level of the blue rectangle 2-2 with 100 × 100 pixels.

Fig. A1 shows the gray level of the blue rectangle 2-2 with 100 × 100 pixels, in which the thermocouple 2 (T2) is on the right side of the rectangle 2-2. The thermocouple has two lines, and the distance between these two lines is about 100 pixels. Thus, the width of the rectangle is chosen as 100 pixels. As the number of pixels increases along the direction of the blue hollow arrow, the mean gray level of rectangle is calculated correspondingly, as shown in Fig. A2. It is observed that the mean gray level almost maintains constant as the number of pixels increases. This indicates that the number of pixels along the direction of the blue hollow arrow has a slight effect on the mean gray level. The same

phenomenon can be found for thermocouple 1 (T1) and thermocouple 3 (T3) in Fig. A2. Thus, Rectangles 2-2, 4-1 and 4-2 with 100 × 100 pixels are reasonable.

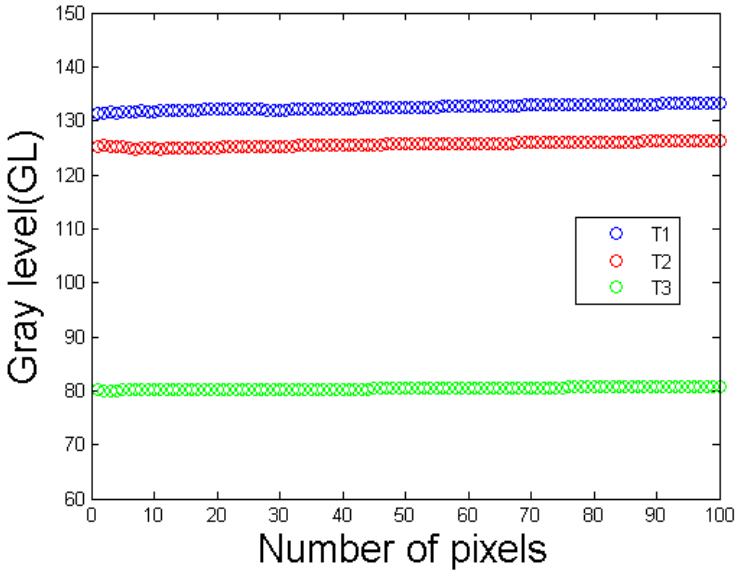

Fig. A2: Effect of number of pixels along the direction of the blue hollow arrow on mean gray level.

Appendix B

In Fig. 3.14, the blue rectangle 2 with 100 × 10 pixels is chosen to be representative of to the measured temperature provided by thermocouple 2 T2. The following presents why this typical area has been chosen.

Fig. B1 shows the gray level of a rectangle with 100 × 100 pixels, located just above the thermocouple T2. The thermocouple has two lines, and the distance between these two wires, welded on the surface as drawn on the Fig. B1. The distance between these two wires is about 100 pixels. Thus, the length of the representative rectangle is chosen as 100 pixels.

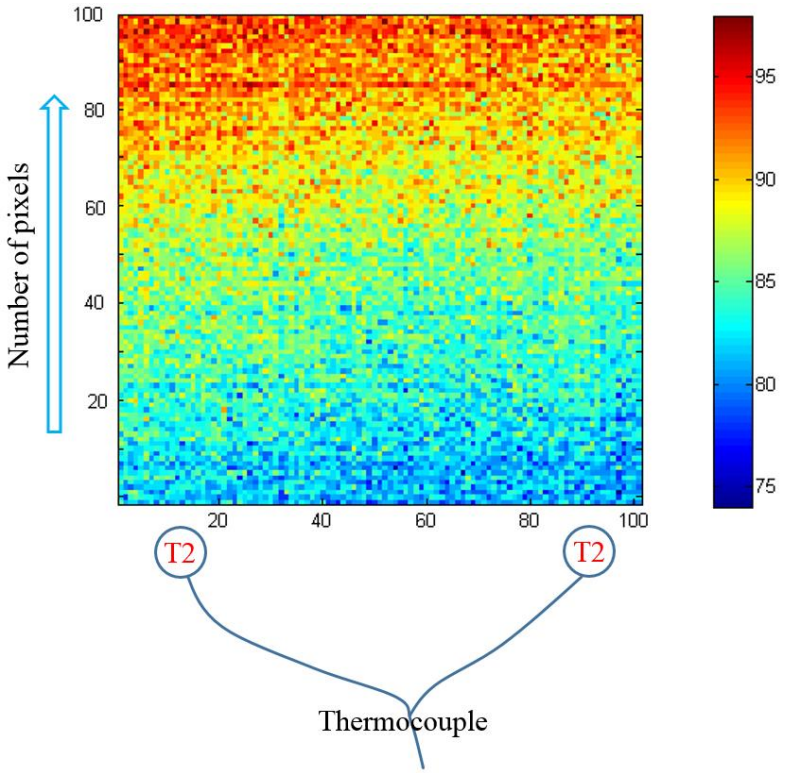

Fig. B1: Gray level of the blue rectangle 2-2 with 100 × 100 pixels.

As the number of pixels increases along the direction of the blue hollow arrow, and the mean gray level of each line of the observed areas is calculated correspondingly, as shown in Fig. B2. The graph B2 shows that the mean gray level increases rapidly with the distance to the thermocouple. Thus, a wide area cannot be chosen to be representative of the material temperature below the thermocouple. Nevertheless, one can observe that the gray level is quite constant within a strip of 10 pixel width. To ensure accuracy, the width of rectangle 2 is set to 10 pixels.

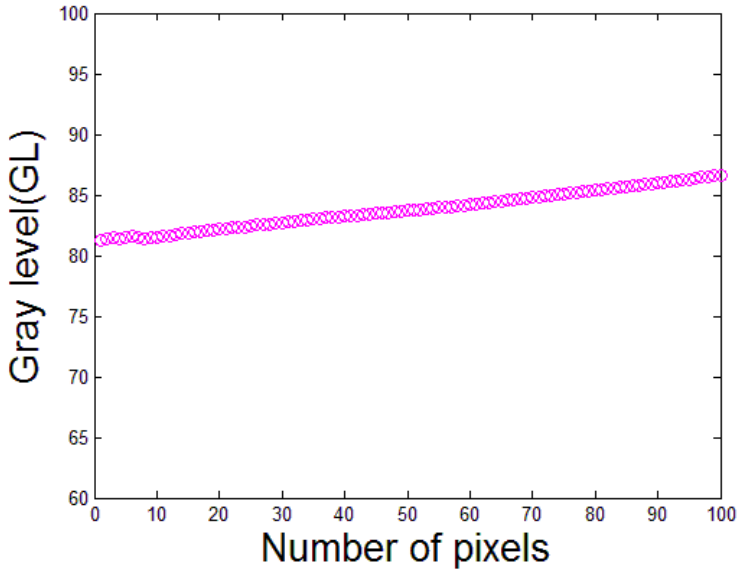

Fig. B2: Gray level variation along the direction of the blue hollow arrow (see Fig. B1) as a function of the number of pixel.

Bibliography

[ASD 02] ASDRUBALI F., BALDINELLI G., BIANCHI F.
A quantitative methodology to evaluate thermal bridges in buildings. Applied Energy, vol. 97, 2012, p. 365-373.

[AST 06] ASTARITA T., CARDONE G., CARLOMAGNO G.M.
Infrared thermography: An optical method in heat transfer and fluid flow visualization. Optics and Lasers in Engineering, vol. 44, n° 3-4, 2006, p. 261-281.

[AVR 08] AVRIL S., BONNET M., BRETELLE A.S., GREDIAC M., HILD F., IENNY P., LATOURTE F., LEMOSSE D., PAGANO S., PAGNACCO E., PIERRON F.
Overview of Identification Methods of Mechanical Parameters Based on Full-field Measurements. Experimental Mechanics, vol. 48, 2008, p. 381-402.

[BAD] BADULESCU C., GREDIAC M., HADDADI H., MATHIAS J.D., BALANDRAUD X., TRAN H.S.
Applying the grid method and infrared thermography to investigate plastic deformation in aluminium multicrystal. Mechanics of Materials, vol. 43, n° 1, 2011, p. 36-53.

[BAR 12] BARREIRA E., DE FREITAS V.P., DELGADO J.M.P.Q., RAMOS N.M.M.
Thermography applications in the study of buildings hygrothermal behavior. In: Prakash RV, editor. Infrared thermography. Croatia, China: InTech; 2012. p. 171-192.

[BAS 00] BASTAWROS A.F., BART-SMITH H., EVANS A.G.
Experimental analysis of deformation mechanisms in a closed-cell aluminium alloy foam. Journal of the Mechanics and Physics of Solids, vol. 48, n° 2, 2000, p. 301-322.

[BES 06] BESNARD G., HILD F., ROUX S.
Finite-Element Displacement Fields Analysis from Digital Images: Application to Portevin Le Chatelier Bands. Experimental Mechanics, vol. 46, n° 6, 2006, p. 789-803.

[BER 06] BERFIELD T.A., PATEL J.K., SHIMMIN R.G., BRAUN P.V., LAMBROS J., SOTTOS N.R.
Fluorescent image correlation for nanoscale deformation measurements. Small, vol. 2, 2006, p. 631-635

[BLA 89] BLACK J.J.E.

Thermal baseline factors in nuclear power plants, in: G.B. McIntosh (Ed.), SPIE, Thermosense XI: International Conference on Thermal Infrared Sensing for Diagnostics and Control, Orlando, FL, 1989, pp. 62.

[BLA 15] BLASDEL N.J. WUJCIK E.K., CARLETTA J.E., LEE K.S., MONTY C.N.

Fabric nanocomposite resistance temperature detector. IEEE Sensors Journal, vol. 15, n° 1, 2015, p. 300-306.

[BLO 80] BLOOMQUIST D.D., SHEFFIELD S.A.

Thermocouple temperature measurements in shock compressed solids. Journal of Applied Physics, vol. 51, 1980, p. 5260-5266.

[BOD 09] BODELOT L., SABATIER L., CHARKALUK E., DUFRENOY P.

Experimental setup for fully coupled kinematic and thermal measurements at the microstructure scale of an AISI 316L steel. Materials Science and Engineering A, vol. 501, n° 1-2, 2009, p. 52-60.

[BOM 78] BOMBERG M., SHIRTLIFFE C.

Influence of moisture and moisture gradients on heat transfer through porous building materials. ASTM STP, vol. 660, 1978, p. 211-233.

[BOR 01] BORGEFORS G., RAMELLA G., BAJA G.A.D.

Shape and topology preserving multi-valued image pyramids for multi-resolution skeletonization. Pattern Recognition Letters, vol. 22, n° 6-7, 2001, p. 741-751.

[CAB 96] CABANNES F.

Température de surface: mesure radiative. In Techniques de l'ingénieur, vol, Traité Mesures et Contrôle R2735, 1996, p. 1-19.

[CAL 14] CALVIE E., RETHORE J., JOLY-POTTUZ L., MEILLE S., CHEVALIER J., GARNIER V., JORAND Y., ESNOUF C., EPICIER T., QUIRK J.B., MASENELLI-VARLOT K.

Mechanical behavior law of ceramic nanoparticles from transmission electron microscopy in situ nano-compression tests. Materials Letters, vol. 119, 2014, p. 107-110.

[CEN 97] CENGEL Y.A.

Introduction to thermodynamics and heat transfer. McGraw Hill series in mechanical engineering/international edition. McGraw Hill; 1997. ISBN: 0-07-01 1498-6.

[CHA 05] CHANG S., WANG C.S., XIONG C.Y., FANG J.

Nanoscale in-plane displacement evaluation by AFM scanning and digital image correlation processing. Nanotechnology, vol. 16, 2005, p. 344-349.

[CHE 01] CHEVALIER L., CALLOCH S., HILD F., MARCO Y.

Digital image correlation used to analyze the multiaxial behavior of rubber-like materials. European Journal of Mechanics A/Solids, vol. 20, 2001, p. 169-187.

[CHO 97] CHOI S., SHAH S.P.

Measurement of deformations on concrete subjected to compression using image correlation, Experimental Mechanics, vol. 37, n° 3, 1997, p. 307-313.

[CHO 05] CHO S.W., CARDENAS-GARCIA J.F., CHASIOTIS I.

Measurement of nano displacement and elastic properties of MEMS via the microscopic hole method. Sensors and Actuators A: Physical, vol. 120, n° 1, 2005, p. 163-171.

[CHO 09] CHOU Y.C., YAO L.

Automatic diagnostic system of electrical equipment using infrared thermography. In Proceedings of the SOCPAR'09 International Conference of IEEE soft computing and pattern recognition, Malaysia, 4-7 December 2009, p. 155-160.

[CHR 10] CHRYSOCHOOS A., HUON V., JOURDAN F., MURACCIOLE J.M., PEYROUX R., WATTRISSE B.

Use of full-field digital image correlation and infrared thermography measurements for the thermomechanical analysis of material behavior. Strain, vol. 46, n° 1, 2010, p. 117-130.

[DAT 13] DATTOMA V., GIANCANE S.

Evaluation of energy of fatigue damage into GFRC through digital image correlation and thermography. Composites: Part B, vol. 47, 2013, p. 283-289.

[DI 2003] DI CARLO A.

Telethermography with the thermostimulus technique, 7th Int. Workshop on advanced infrared technology and applications. Pisa; 09; 2003.

[FAV 95] FAVRO L.D., AHMED T., HAN X., WANG L., SHEPARD S.M.

Thermal wave imaging of aircraft structures. Review of Progress in Quantitative Non-Destructive Evaluation, vol. 14, 1995, p. 461-466.

[FAV 07] FAVIER D., LOUCHE H., SCHLOSSER P., ORGEAS L., VACHER P., DEBOVE L.

Homogeneous and heterogeneous deformation mechanisms in an austenitic polycrystalline Ti-50.8 at% Ni thin tube under tension. Investigation via temperature and strain fields measurements. Acta Materialia, vol. 55, n° 16, 2007, p. 5310-5322.

[FRA 07] FRANCK C., HONG S., MASKARINEC S.A., TIRRELL D.A., RAVICHANDRAN G.

Three-dimensional full-field measurements of large deformations in soft materials using confocal microscopy and digital volume correlation. Experimental Mechanics, vol. 47, 2007, p. 427-438.

[GEN 09] GENIX M., VAIRAC P., CRETIN B.

Local temperature surface measurement with intrinsic thermocouple. International Journal of Thermal Sciences, vol. 48, n° 9, 2009, p. 1679-1682.

[GOI 13] GOIDESCU C., WELEMANE H., GARNIER C., FAZZINI M., BRAULT R., PERONNET E., MISTOU S.

Damage investigation in CFRP composites using full-field measurement techniques: Combination of digital image stereo-correlation, infrared thermography and X-ray tomography. Composites: Part B, vol. 48, 2013, p. 95-105.

[GRI 02] GRINZATO E., BISON P.G., MARINETTI S.

Monitoring of ancient buildings by the thermal method. Journal of Cultural Heritage, vol. 3, n° 1, 2002, p. 21-29.

[HAN 04] HANA FIKACKOVA M.D., EKBERG E.

Can infrared thermography be a diagnostic tool for arthralgia of the temporomandibular joint ?. Oral Surgery, Oral Medicine, Oral Pathology, Oral Radiology, and Endodontology, vol. 98, n° 6, 2004, p. 643-650.

[HAR 18] HARZALLAH M., POTTIER T., GIBLAS R., LANDON Y., MOUSSEIGNE M., SENATORE J.

A coupled in-situ measurement of temperature and kinematic fields in Ti-6Al-4V serrated chip formation at micro-scale. International Journal of Machine Tools and Manufacture, vol. 130-131, 2018, p. 20-35.

[HE 84] HE Z.H., SUTTON M.A., RASNSON W.F., PETERS W.H.

Two-dimensional fluid velocity measurement by use of digital-speckle correlation technique. Experimental Mechanics, vol. 24, n° 2, 1984, p. 117-121.

[HIL 06] HILD F., ROUX S.

Digital Image Correlation: from Displacement Measurement to Identification of Elastic Properties: a Review. Strain, vol. 42, n° 2, 2006, p. 69-80.

[HIL 09] HILD F., ROUX S., GRAS R., GUERRERO N., MARANTE M.E., FLOREZ-LOPEZ J.

Displacement measurement technique for beam kinematics. Optics and Lasers in Engineering, vol. 47, 2009, p. 495-503.

[HIL 12] HILD F., ROUX S.

Comparison of local and global approaches to digital image correlation. Experimental Mechanics, vol. 52, 2012, p. 1503-1519.

[ITA 04] ITAMI K., SUGIE T., VAYAKIS G., WALKER C.

Multiplexing thermography for international thermonuclear experimental reactor divertor targets. Review of Scientific Instruments, vol. 75, 2004, p. 4124-4128.

[KAN 05] KANG J., JAIN M., WILKINSON D.S.

Microscopic strain mapping using scanning electron microscopy topography image correlation at large strain. The Journal of Strain Analysis for Engineering Design, vol. 40, 2005, p. 559-570.

[KAF 11] KAFIEH R., LOTFI T., AMORFATTAHI R.

Automatic detection of defects on polyethylene pipe welding using thermal infrared imaging. Infrared Physics & Technology, vol. 54, n° 4, 2011, p. 317-325.

[KIM 11] KIM J., KIM J.D.

Voltage divider resistance for high-resolution of the thermistor temperature measurement. Measurement, vol. 44, n° 10, 2011, p. 2054-2059.

[KNA 03] KNAUSS W.G., CHASIOTIS I., HUANG Y.

Mechanical measurements at the micron and nanometer scales. Mechanics of Materials, vol. 35, n° 3-6, 2003, p. 217-231.

[KRS 15] KRSTULOVIC-OPARA L., SURJAK M., VESENJAK M., TONKOVIC Z., KODVANJ J., DOMAZET Z.

Comparison of infrared and 3D digital image correlation techniques applied for mechanical testing of materials. Infrared Physics & Technology, vol. 73, 2015, p. 166-174.

[LAH 11] LAHIRI B.B., BAGAVATHIAPPAM S., SARAVANAN T., RAJKUMAR K.V., KUMAR A., PHILIP J., JAYAKUMAR T.

Defect detection in weld joints by infrared thermography, in: International Conference on NDE in Steel and allied Industries, NDESAI, 2011, Jamshedpur, India, 2011, p. 191-197.

[LEC 09] LECLERC H., PERIE J.-N., ROUX S., HILD F.

Integrated Digital Image Correlation for the Identification of Mechanical Properties. Gagalowicz A., Philips W., Eds., Computer Vision/Computer Graphics Collaboration Techniques, vol. 5496 de Lecture Notes in Computer Science, p. 161-171, Springer Berlin Heidelberg, 2009.

[LEP 07] LEPRINCE S., BARBOT S., AYOUB F., AVOUAC J.P.

Automatic and precise orthorectification, coregistration, and subpixel correlation of satellite images, application to ground deformation measurements. IEEE Transactions on Geoscience and Remote Sensing, vol. 45, n° 6, 2007, p. 1529-1558.

[LIS 11] LISOWSKA-LIS A., MITKOWSKI S.A., AUGUSTYN J.

Infrared technique and its application in science and engineering in the study plans of students in electrical engineering and electronics. In: 2nd World conference on technology and engineering education Ljubljana, Slovenia; 5th–8th September; 2011.

[LJU 94] LJUNGBERG S.A.

Infrared techniques in buildings and structures: Operation and maintenance. Infrared Methodology and Technology, 1994, 7, p. 211-252.

[LOU 12] LOUCHE H., SCHLOSSER P., FAVIER D., ORGEAS L.

Heat source processing for localized deformation with non–constant thermal conductivity. Application to superelastic tensile tests of NiTi shape memory alloys. Experimental Mechanics, vol. 52, n° 9, 2009, p. 1313-1328.

[LUO 98] LUONG M.P.

Fatigue limit evaluation of metals using an infrared thermographic technique. Mechanics of Materials, vol. 28, n° 1-4, 1998, p. 155-163.

[MAH 05] MAHMOUD M.

Engineering thermofluids. Heidelberg, New York, Dordrecht, London: Springer; 2005.

[MAI 09] MAIERHOFER C., ROELLIG M.

Active thermography for the characterization of surfaces and interfaces of historic masonry structures. In Proceedings of the 7th International Symposium on Non-destructive Testing in Civil Engineering (NDTCE), Nantes, France, 30 June–3 July 2009.

[MAY 12] MAYNADIER A., PONCELET M., LAVERNHE-TAILLARD K., ROUX S.

One-shot measurement of thermal and kinematic fields: Infrared image correlation (IRIC). Experimental Mechanics, vol. 52, 2012, p. 241-255.

[MCC 10] MCCORMICK N., LORD J.

Digital image correlation. Materials Today, vol. 13, n° 12, 2010, p. 52-54.

[MEN 06] MENAKA M., BAGAVATHIAPPAM S., BEMLAYRAMAN B., JAYAKUMAR T., RAJ B.

Characterization of adhesively bonded laminates using radiography and infrared thermal imaging techniques. Insight, vol. 48, 2006, p. 606-612.

[MEO 04] MEOLA C., CARLOMAGNO G.M., SQUILLACE A., GIORLEO G.

The use of infrared thermography for nondestructive evaluation of joints. Infrared Physics & Technology, vol. 46, n° 1-2, 2004, p. 93-99.

[NGU 10] NGUTEN A.V., COHEN N.J., LIPMAN H., BROWN C.M., MOLINARI N.A., JACKSON W.L., KIRKING H., SZYMANOWSKI P., WILSON T.W., SALHI B.A., ROBERTS R.R., STRYKER D.W., FISHBEIN D.B.

Comparison of 3 infrared thermal detection systems and self-report for mass fever screening. Emerging Infectious Diseases, vol. 16, n° 11, 2010, p. 1710-1717.

[NOW 18] NOWAK M., MAJ M.

Determination of coupled mechanical and thermal fields using 2D digital image correlation and infrared thermography: Numerical procedures and results. Archives of Civil and Mechanical Engineering, vol. 18, n° 2, 2018, p. 630-644.

[ORT] ORTEU J.J., ROTROU Y., SENTENAC T., ROBERT L.

An innovative method for 3-D shape, strain and temperature full-field measurement using a single type of camera: principle and preliminary results, Experimental Mechanics, vol. 48, n° 2, 2008, p. 163-179.

[PAN 07] PAN B.

Digital image correlation method and its application in experimental mechanics. Doctoral Thesis, Tsinghua University, Beijing, 2007.

[PAN 09] PAN B., QIAN K., XIE H., ASUNDI A.

Two-dimensional digital image correlation for in-plane displacement and strain measurement: a review. Measurement Science and Technology, vol. 20, 2009, p. 062001.

[PAN 10] PAN B., WANG Z., LU Z.

Genuine full-field deformation measurement of an object with complex shape using reliability-guided digital image correlation, Optics Express, vol. 18, n° 2, 2010, p. 1011-1023.

[PAS 08] PASTOR M.L., BALANDRAUD X., GREDIAC M., ROBERT J.L.

Applying infrared thermography to study the heating of 2024-T3 aluminium specimens under fatigue loading. Infrared Physics & Technology, vol. 51, n° 6, 2008, p. 505-515.

[PER 17] PEREIRA C.G., RAMASWAMY H.S., DE OLIVEIRA GIAROLA T.M., RESENDE J.V.

Infrared thermography as a complementary tool for the evaluation of heat transfer in the freezing of fruit juice model solution. International Journal of Thermal Sciences, vol. 120, 2017, p. 386-399.

[PET 82] PETERS W.H., RANSON W.F.

Digital imaging technique in experimental mechanics. Optical Engineering, vol. 21, n° 3, 1982, p. 427-431.

[PET 83] PETERS W.H., RANSON W.F., SUTTON M.A., CHU T.C., ANDERSON J.

Application of digital correlation methods to rigid body mechanics. Optical Engineering, vol. 22, n° 6, 1983, p. 738-742.

[PIT 02] PITTER M.C., SEE C.W., GOH J.Y.L., SOMEKH M.G.

Focus errors and their correction in microscopic deformation analysis using correlation. Optics Express, vol. 23, 2002, p. 1361-1367.

[RET 05] RETHORE J., GRAVOUIL A., MORESTIN F., COMBESCURE A.

Estimation of mixed-mode stress intensity factors using digital image correlation and an interaction integral. International Journal of Fracture, vol. 132, n° 1, 2005, p. 65-79.

[RET 07a] RETHORE J., ROUX S., HILD F.

From pictures to extended finite elements: Extended digital image correlation (X-DIC). Comptes Rendus Mécanique, vol. 335, n° 3, 2007, p. 131-137.

[RET 07b] RETHORE J., ROUX S., HILD F.

Shear-band capturing using a multiscale extended digital image correlation technique. Computer Methods in Applied Mechanics and Engineering, vol. 196, n° 49-52, 2007, p. 5016-5030.

[RET 08] RETHORE J., HILD F., ROUX S.

Extended digital image correlation with crack shape optimization. International Journal for Numerical Methods in Engineering, vol. 73, n° 2, 2008, p. 248-272.

[RET 10a] RETHORE J.

A fully integrated noise robust strategy for the identification of constitutive laws frin digital images. International Journal for Numerical Methods in Engineering, vol. 84, 2010, p. 631-660.

[RET 10b] RETHORE J., ELGUEDJ T., SIMON P., CORET M.

On the Use of NURBS Functions for Displacement Derivatives Measurement by Digital Image Correlation. Experimental Mechanics, vol. 50, 2010, p. 1099-1116.

[RET 13] RETHORE J., MUHIBULLA, ELGUEDJ T., CORET M., CHAUDET P., COMBESCURE A.

Robust identification of elasto-plastic constitutive law parameters from digital images using 3D kinematics. International Journal of Solids and Structures, vol. 50, n° 1, 2013, p. 73 - 85.

[RET 18] RETHORE J.

UFreckles (version v 2.0). Zenodo, http://doi.org/10.5281/zenodo.1433776, October 1, 2018.

[RIN 10] RING F.

Thermal imaging today and its relevance to diabetes. Journal of Diabetes Science and Technology, vol. 4, 2010, p. 857-862.

[ROB 09] ROBITAILLE P.M.

Kirchhoff's law of thermal emission: 150 years. Progress in Physics, 2009.

[ROT 06a] ROTROU Y.

Thermographie courtes longueurs d'onde avec des caméras silicium: contribution à la modélisation radiométrique, Thèse, L'école des mines d'Albi-Carmaux, 2006.

[ROT 06b] ROTROU Y., SENTENAC T., LE MAOULT Y., MAGNAN P., FARRE J.

Near-infrared thermography with silicon FPA-Comparison to MWIR and LWIR thermography. Quantitative Infrared Thermography Journal, vol. 3, n° 1, 2006, p. 93-115.

[ROU 06] ROUX S., HILD F.

Stress intensity factor measurements from digital image correlation: post processing and integrated approaches. International Journal of Fracture, vol. 140, n° 1-4, 2006, p. 141-157.

[RUD 03] RUDDOCK W.

Advanced infrared resources, www.infraredthermography.com; 2003.

[SAB 06] SABATE N., VOGEL D., GOLLHARDT A., KELLER J., MICHEL B.

Measurement of residual stresses in micro-machined structures in a micro-region. Applied Physics Letters, vol. 88, n° 7, 2006, p. 071910.

[SAU 97] SAUNDERS P.

General interpolation equations for the calibration of radiation thermometers. Metrologia, vol. 34, 1997, p. 201-210.

[SCA 92] SCAMBOS T.A., DUTKIEWICZ M.J., WILSON J.C.

Application of image cross-correction to the measurement of glacier velocity using satellite image data. Remote Sensing of Environment, vol. 42, n° 3, 1992, p. 177-186.

[SRI 12] SRINIVASAN N., RAGHU N., VENKATRAMAN B.

Study on Lüders deformation in welded mild steel using infrared thermography and digital image correlation. Advanced Materials Research, vol. 585, 2012, p. 82-86.

[SUN 97] SUN Z.L., LYONS J.S., MCNEILL S.R.

Measuring microscopic deformations with digital image correlation. Optics and Lasers in Engineering, vol. 27, 1997, p. 409-428.

[SUN 05] SUN Y., PANG J.H.L., WONG C.K., SU F.

Finite element formulation for a digital image correlation method. Applied Optics, vol. 44, n° 34, 2005, p. 7357-7363.

[SUN 06] SUN Y.F., PANG J.H.L.

AFM image reconstruction for deformation measurements by digital image correlation. Nanotechnology, vol. 17, 2006, p. 933-939.

[SUT 83] SUTTON M.A., WOLTERS W.J., PETERS W.H., RANSON W.F., MCNEILL S.R.
Determination of displacements using an improved digital correlation method. Image and Vision Computing, vol. 1, n° 3, 1983, p. 133-139.

[TEY 07] TEYSSIEUX D., THIERY L., CRETIN B., BRIAND D., DE ROOIJ N.F.
Precise thermography of microsystems in the visible region using a standard CCD camera. In Proc. IEEE Sensors, October, 2007, p. 926-929.

[TEY 08] TEYSSIEUX D., BRIAND D., CHARNAY J., DE ROOIJ N.F., CRETIN B.
Dynamic and static thermal study of micromachined heaters: the advantages of visible and near-infrared thermography compared to classical methods. Journal of Micromechanics and Microengineering, vol. 18, 2008, p. 065005.

[TEY 09] TEYSSIEUX D., EUPHRASIE S., CRETIN B.
Thermal detectivity enhancement of visible and near infrared thermography by using super-resolution algorithm: Possibility to generalize the method to other domains. Journal of Applied Physics, vol. 105, 2009, p. 064911.

[USA 14] USAMENTIAGA R., VENEGAS P., GUEREDIAGA J., VEGA L., MOLLEDA J., BULNES F.G.
Infrared thermography for temperature measurement and non-destructive testing. Sensors, vol. 14, n° 7, 2014, p. 12305-12348.

[VEN 98a] VENDROUX G., KNAUSS W.G.
Submicron deformation field measurements: Part 1. Developing a digital scanning tunneling microscope. Experimental Mechanics, vol. 38, 1998, p. 18-23.

[VEN 98b] VENDROUX G., KNAUSS W.G.
Submicron deformation field measurements: Part 2. Improved digital image correlation. Experimental Mechanics, vol. 38, 1998, p. 86-92.

[VEN 98c] VENDROUX G., KNAUSS W.G.
Submicron deformation field measurements: Part 3. Demonstration of deformation determinations. Experimental Mechanics, vol. 38, 1998, p. 154-160.

[WAN 00] WANG H., JIANG L., LIAW P.K., BROOKS C.R., KIARSTROM D.L.
Infrared temperature mapping of ULTIMET alloy during high-cycle fatigue. Metallurgical and Materials Transaction A, vol. 31, n° 4, 2000, p. 1307-1310.

[WAN 06] WANG H., XIE H., JU Y., DUAN Q.

Error analysis of digital speckle correlation method under scanning electron microscope. Experimental Techniques, vol. 30, 2006, p. 42-45.

[WAN 11] WANG T., HU X., TANG D., GUO C.

Infrared thermal image of vapor-liquid interface in capillary microgroove heat sink. International Journal of Thermal Sciences, vol. 50, n° 3, 2011, p. 274-279.

[WAN 16] WANG X.G., WITZ J.F., BARTALI A.E., JIANG C.

Infrared thermography coupled with digital image correlation in studying plastic deformation on the mesoscale level. Optics and Lasers in Engineering, vol. 86, 2016, p. 264-274.

[WAN 17] WANG X.G., WANG L., HUANG M.X.

Kinematic and thermal characteristics of Lüders and Protevin-Le Châtelier bands in a medium Mn transformation-induced plasticity steel. Acta Materialia, vol. 124, 2017, p. 17-29.

[YAM 81a] YAMAGUCHI I.

Speckle displacement and deformation in the diffraction and image fields for small object deformation. Acta Optica Sinica, vol. 28, n° 10, 1981, p. 1359-1376.

[YAM 81b] YAMAGUCHI I.

A laser-speckle strain gage. Journal of Physics E: Scientific Instruments, vol. 14, 1981, p. 1270-1273.

[YON 03] YONEYAMA S., MORIMOTO Y.

Accurate displacement measurement by correlation of colored random patterns. JSME International Journal Series A Solid Mechanics and Material Engineering, vol. 46, n° 2, 2003, p. 178-184.

[YON 06] YONEYAMA S., KIKUTA H., KITAGAWA A., KITAMURA K.

Lens distortion correlation for digital image correlation by measuring rigid body displacement. Optical Engineering, vol. 45, n° 2, 2006, p. 023602.

[ZIN 95] ZINK A.G., DAVIDSON R.W., HANNA R.B.

Strain measurement in wood using a digital image correlation. Wood and Fiber Science, vol. 27, n° 4, 1995, p. 346-359.

[ZHA 02] ZHANG D.S., EGGLETON C.D., AROLA D.D.

Evaluation the mechanical behavior of arterial tissueusing digital image correlation. Experimental Mechanics, vol. 42, n° 4, 2002, p. 409-416.

Publications

Journal Articles:

[1] C. Zhang, J. Marty, A. Maynadier, P. Chaudet, J. Réthoré, M.C. Baietto. An innovative technique for real-time adjusting exposure time of silicon-based camera to get stable gray level images with temperature evolution. **Mechanical Systems and Signal Processing**, vol. 122, 2019, p. 419-432.

[2] C. Zhang, J. Marty, A. Maynadier, P. Chaudet, J. Réthoré, M.C. Baietto. Application of silicon-based camera for measurement of non-homogeneous thermal field on realistic specimen surface. **Applied Thermal Engineering**, vol. 149, 2019, p. 1186-1191.

Academic Conferences:

28/08/2017-01/09/2017	Conference of French Mechanics	Lille
20/03/2018-22/03/2018	International Conference of Photo Mechanics	Toulouse
04/06/2018-07/06/2018	Annual Conference-Society for Experimental Mechanics	Greenville
08/10/2018-10/10/2018	International Conference of Manufacturing Engineering	Paris

FOLIO ADMINISTRATIF

THESE DE L'UNIVERSITE DE LYON OPEREE AU SEIN DE L'INSA LYON

NOM: ZHANG DATE de SOUTENANCE: 05/03/2019

Prénoms: Chao

TITRE: Quantitative kinematic and thermal full fields measurements

NATURE: Doctorat Numéro d'ordre: 2019LYSEI013

Ecole doctorale: MECANIQUE, ENERGETIQUE, GENIE CIVIL, ACOUSTIQUE

Spécialité: Mécanique – Génie Mécanique – Génie Civil

RESUME: Simultaneous measurement of kinematic and thermal full fields are very important for thermomechanical procedures. Silicon-based cameras are widely used to perform real-time observation of the kinematic fields, mainly thanks to digital image correlation. Moreover, they are known to be as well sensitive in the near-infrared spectral range, thus the acquirement of thermal fields using a silicon-based camera is possible. However, there are two main problems for the silicon-based camera to obtain simultaneously kinematic and thermal fields. One is that in the near-infrared spectral range, a small temperature variation will lead to a large modification in the image gray level, which easily leads to poor quality images. Another is that digital image correlation needs a heterogeneous and contrasting surface, while the near-infrared thermography needs a homogeneous and constant surface. In this thesis, an innovative technique was proposed to automatically adjust the exposure time of the camera to obtain kinematically and thermally exploitable images whatever the temperature evolution occurs on the surface of the observed object. This technique was validated by different experiments, including blackbody heating experiments and realistic specimen heating experiments. Radiometric models of blackbody and specimen surface ware calibrated respectively. Based on the radiometric models, thermal fields have been reconstructed on the kinematically and thermally exploitable images. High temperature tube ballooning experiment is conducted to perform kinematic and thermal fields. Global digital image correlation was performed to obtain kinematic fields. To perform near-infrared thermography on the specimen surface, radiometric model is calibrated based on portions of brightest pixels. In this case 20% of the brightest pixels is used to perform radiometric model calibration. Based on the radiometric model using 20% of brightest pixels, thermal fields are reconstructed. Combined with the known coordinates of kinematic field by digital image correlation, the thermal field at the same coordinates as kinematic field can be obtained.

MOTS-CLÉS: Silicon-based camera, Kinematic field, Thermal field, Radiometric model, Exposure time adjustment, Thermomechanical

Laboratoire (s) de recherche : Laboratoire de Mécanique des Contacts et des Structures
UMR CNRS 5259 – INSA de Lyon
20, avenue Albert Einstein
69621 Villeurbanne Cedex FRANCE

Directeur de thèse: Marie-Christine BAIETTO

Président de jury: Eric CHARKALUK

Composition du jury: Bertrand WATTRISSE, Fabien AMIOT, Eric CHARKALUK, Anne MAYNADIER, Julien RÉTHORÉ, Marie-Christine BAIETTO